A THESIS FOR THE DEGREE OF DOCTOR OF PHILOSOPHY

Printed electronics based environmental and bio sensors fabrication and performance tuning through optimized structures and materials

Memoon Sajid

Department of Mechatronics Engineering

GRADUATE SCHOOL

JEJU NATIONAL UNIVERSITY

2018. 02

Printed electronics based environmental and bio sensors fabrication and performance tuning through optimized structures and materials

Memoon Sajid

(Supervised by Professor Kyung Hyun Choi)

A thesis submitted in partial fulfillment of the requirement for the degree of Doctor of Philosophy

2018. 02

The thesis has been examined and approved.

Jong Hwan Lim

Thesis Director: Jong-Hwan Lim, Professor, Department of Mechatronics Engineering

Supervisor: Kyung Hyun Choi, Professor, Department of Mechatronics Engineering

Yang Hoi Doh

Yang-Hoi Doh, Professor, Department of Electronic Engineering

C. N. Kang

Chang-Nam Kang, Professor, Department of Mechanical Engineering

Jeongdai Jo

Dr. Jeong-Dai Jo, Principal Researcher, Korea Institute of Machinery & Materials

Date

Department of Mechatronics Engineering

GRADUATE SCHOOL

JEJU NATIONAL UNIVERSITY

REPUBLIC OF KOREA

Dedicated to my beloved parents without whom I would not be where I am today and to my dear Pakistan.

Acknowledgements

All praise to Almighty Allah for blessing me with strength, courage, and knowledge; and helping me out constantly to achieve this honor. He has never left me helpless and has always guided me in the right direction throughout this long journey. Without His help and blessings, I would not have been able to complete a single step. I pray to Him to make the path of my future easy and help me in doing something good for humanity.

My sincerest gratitude is towards my parents who have always supported me at all steps of my life. They have provided me with everything in their power and beyond. Without their love and constant support, this journey would have ended far earlier for me. It was their encouragement and motivation that kept me going and I am indebted to them forever. I am also grateful to Dr. Masood Akbar for guiding me throughout my life and my educational career and helping me achieve my goals with his constant support in all forms possible. He has always inspired me to become a better human being and put others before myself. I would also like to thank my sisters and brother; Tuba, Azka, and Mohsin; and my wife Farah whose support was always there when I needed it the most.

I am extremely thankful to Prof. Kyung Hyun Choi who is the best PhD supervisor I could have asked for. I will always be indebted to him for his kindness, endless support, and guidance throughout my program. I would remember the amount of trust he has put into me and the confidence that I got as a result. I wish him all the happiness in his life. I would also like to thank all the other teachers in my life who have been the real builders of my personality and the torchbearers of knowledge for me at each and every stage of my life.

I am thankful to all my seniors and mentors, specially Dr. Muhammad Zubair who taught me a lot to help me start my research, and others including Dr. Kamran Ali, Dr. Khalid Rahman, Dr. Ghayas Uddin Siddiqui, Dr. Zahid Manzoor, Dr. Farrukh Israr, Dr. Murtuza Mehdi, Dr. Afaq, Dr. Naveneethan, Dr. Junaid Ali, Dr. Safdar Ali, Dr. Rashid Ahmed, Dr. Sohail Khan, Dr. Anil Kumar, Dr. Karhik Krish, Dr. Saravan Kumar, Dr. Sirminder Singh Sodhi, Dr. Young Jin Yang, Dr. Hyun Woo Dang, and specially Dr. Shahid Aziz. I am thankful to my AMM lab colleagues including Jahan Zeb Gul, Hyun Bum Kim, Soo Wan Kim, Young Su Kim, Srikanth, Asad Ullah, Imran, Muhsin, Shital, Mutee, Jae Wook, Kyung Hwan, Dae You, and Go Bum. I am particularly thankful to my friends including Gul Hassan, Zubair Amjad, Irshad Ali, Waseem Abbas, Arshad Hassan, Sehrish Malik, Umair, Tahir, Fayaz, Alluri, Parthiban, Waqar, Israr, Khurram, Asif, Asim, Mudassar, Shahbaz, and others who have been here with me through my journey and made my life easier away from

home. We have had many good memories together that I will cherish throughout my life.

I would take this opportunity to thank the wonderful people of Korea and particularly Jeju who have always been kind to me and other foreigners. Everyone here is very helpful, humble, friendly, honest, and awesome. Living on a small island for four years, thousands of miles away from home, in a different culture with people speaking an unrecognizable language seemed a walk in the park just because of the amazing natives of this great country.

May Allah guide us and help us all in our lives here and hereafter.

Memoon Sajid, December 2017

Contents

List of Figures

List of Tables

Abstract

This research work focuses on the development of high performance sensing devices through all printed fabrication methods. The targeted sensors include environmental and bio-monitoring devices. Humidity and temperature sensors have been developed under the category of environmental sensors while multi-reagent immunosensors and human posture detection sensors lie under the category of bio-sensors. The aim of this research was to improve the performance parameters like sensitivity, selectivity, range of detection (RoD), limit of detection (LoD), response time, recovery time, robustness, stability, and accuracy. The output response curve shape linearity was also targeted and easy to interface readout signals were preferred for the devices. All these targets were achieved through interdisciplinary research in three major fields including appropriate electronic material selection and synthesis, device structure optimization through device physics and sensing mechanism, and compatible printing based fabrication system and process optimization to realize the devices. After fabrication, the sensors were characterized to evaluate their performance parameters through in-house developed highly accurate and reliable characterization setups. The devices were then interfaced with specifically designed electronic circuits to employ them in real-life applications for environmental monitoring and point of care (POC) diagnosis for various diseases and conditions. The humidity sensors developed in this research work outperform the reported sensors in literature and have at least comparable or better properties than the commercially available sensors in the market. The temperature sensor is capable of recording the data in both terrestrial and aquatic environments with RoD well suitable for general environmental monitoring. The immunosensors and the POC setup developed in this research is capable to detect multiple bio-reagents crucial for early diagnosis of various diseases with high sensitivity and with LoD and RoD well within the required clinical range of detection. In short, this research work successfully presents unique combination of multiple fields of study to optimize and improve the performance of sensing devices.

1 Introduction

Environmental and bio-monitoring are crucial for investigating climate change, weather forecasting, health care, industry, and other applications [1]. Parameters like temperature, humidity, radiation, wind speed, gases, light intensity, contamination, etc. are detected both quantitatively and qualitatively to establish a complete set of information [2]. The major parameters used for basic weather monitoring include relative humidity and temperature [3–5], while for bio-monitoring, different biological species like bacteria and antigens are detected and their concentration is measured [6–11]. All these factors are crucial in monitoring and control of application-specific environments and health care industry [12]. A huge magnitude of research has focused and is currently focusing on the development of high performance sensors for this purpose. The basic goal in all sensors based research is to improve the performance, reduce the cost, and make the fabrication process easier and mass production compatible [13,14]. An ideal sensor would be cheap, highly sensitive, specific, will have wide operation range, accurate, stable, and robust, with fast transient response, easy to fabricate and interface with user-friendly output [15,16]. It is not possible to have a single sensor possessing all these qualities combined [17]. Rather, there is always a trade-off among one or more of the parameters [18,19]. The good thing, however, is that application specific sensors do not need to possess the complete set of the mentioned qualities but only need few of them together [20]. Researchers try to achieve these goals by using different approaches like changing the sensor materials [21–27], device structure [23,27–43], working mechanism [44–49], fabrication process, etc. A majority of research on sensors development for target specific applications focuses on a single parameter to achieve the target. The research group specializing in materials chemistry try to solve the issues by developing novel high performance materials, physicists try to tweak the device structure and working principle, and so on. Advancement in 3D printing and additive manufacturing has enabled the fabrication of electronic sensing devices that were not possible through conventional methods [50,51]. They allow liberty in design and specifications and make it possible to fabricate embedded devices like sensors, OLEDs, FETs, and actuators inside a printed 3D structure. Various printing methods and materials have been employed by researchers to fabricate sensing devices like accelerometers, ECG electrodes, optical sensors, pressure sensors, tactile sensors, displacement sensors, temperature sensors, biosensors, chemo sensors, gas detection sensors, flow sensors, humidity sensors, antennas, and so on [52]. Novel active materials with desired properties to carry out the targeted task are being developed that are compatible with additive manufacturing technologies [53–56]. Device physics is being thoroughly studied to optimize the device structure and physical parameters for best performance. The fact, however, remains that all the targeted

goals cannot be achieved using one of the mentioned techniques. The major drawbacks of using one approach to tackle the issues include compromise on performance parameters, complicated device structures and user interface, expensive and difficult fabrication, incompatibility with majority of the mainstream technology like smartphones, and other. To develop ideal sensors for target specific applications, researchers have to combine the knowledge from different fields.

To solve these issues, the current work focuses on the development of high performance environmental and bio-sensors by considering all three major related research areas together. The sensor structures have been developed after optimization, printed electronics and additive manufacturing approaches are used for the fabrication of the device that are cheap and easy to fabricate and conformable with wearable technology, novel materials have been developed for high performance application specific requirements that are compatible with the fabrication systems and methods, and easy user interface and compatibility has been developed to allow the devices to seamlessly integrate with daily use gadgets and devices like smartphones. This allows even the layman users, hobbyists, and professionals who do not have device based sound technical knowledge to employ these devices in their targeted applications like IoT, smart homes, big-data for environmental monitoring, and point of care systems.

2 Electronic Materials Synthesis

For any sort of device fabrication, materials are one of the most vital elements. It is of great importance to select and synthesize appropriate materials based on the required applications. The materials must possess the properties that can perform the desired operation and must also be compatible with the available fabrication technologies that are printing systems in case of this research work. The materials selection and synthesis process starts with enlisting the properties required for the target application. A number of candidates are short listed based on their intrinsic properties and then one or more of them are selected based on the design and fabrication requirements. In current research work targeting environmental and bio-sensing devices, three major categories of materials were studied in detail. They include conductive materials for electrode fabrication, active layer materials for sensing area fabrication, and bio-materials to study the interaction of different bio-reagents and the effects of those interactions. All these materials involved in electronic sensing device fabrication can be referred to as electronic materials due to the change in their electrical properties that can be studied as the device output.

2.1 Electrode Materials

All the sensors fabricated in this research work were based on changes in electronic properties and were listed in the electronic sensors category. For the fabrication of electronic sensors, a transducer is one of the core device elements that converts any kind of signals in to electrical signals that can be detected by the read-out circuits. For the fabrication of the transducers, different conductive inks based on metallic nano-particles were used. The electrodes were designed in an interdigitated transducer (IDT) patterns in most of the devices in this work. IDT design was selected based on its superiority in performance relative to other transducer designs owing to its large area and multi chemristors element design. For the initial sensing devices, gold was used as the electrode material deposited in IDT pattern using lithography technique. The electrode material and fabrication method were later replaced with silver nano particle based conductive inks and printing techniques to make it compatible with printed electronic approaches. Two types of commercially available silver nano-particle inks were used for electrode fabrication including Ag nanoparticles ink purchased from PARU with particles diameter range of 20~200 nm, Ag contents of 80~88 wt% and typical resistance of 2.0 mΩ/□/mil and Silverjet DGH ink for reverse offset (viscosity: 1.5 cps, surface tension: 24.4 mN/m, dispersion matrix: octane based). These inks were compatible with multiple pattern printing systems including reverse offset printing, screen printing, EHD printing, and inkjet printing. In a third type,

Electroninks Circuit Scribe Conductive ink pen with ~2 Ω/cm conductivity was used for the hand drawn electrode patterns onto the substrates.

2.2 Active Layer Materials

Active layer materials possess the highest importance in any electronic sensing device and they are selected after carefully considering their electronic readout capabilities, sensitivity towards the target analytes, saturation values, limits of detection, re-usability, long-term stability, low cost, environmental effects, and so on. Three major categories of active layer materials were used in this research work including polymers, 2D materials, and composites.

2.2.1 Electronic polymers

1) The first polymer used for the fabrication of humidity sensors active layer was Poly (3, 4-ethylenedioxythiophene) Polystyrene Sulfonate (PEDOT:PSS). The materials was purchased in the form of a thick paste from Orgacon EL-P5010 solvent based paste with 3 wt% solid content. PEDOT:PSS is a conductive polymer with excellent response towards change in humidity in the surrounding environment. The conductivity of the thin film of polymer changes with the change in amount of absorbed water vapors and molecules from the surroundings [3]. A solution of PEDOT:PSS that can be deposited in the form of thin film using electro-spray deposition was synthesized by diluting PEDOT:PSS paste into isopropyl alcohol (IPA) and was ultra-sonicated for 30 min. Ink was then placed on a magnetic stirrer at room temperature for 3 hours until a homogenous solution was formed. 2% of di-methyl sulfoxide (DMSO) was added to the solution as a surfactant to improve dispersion and facilitate the spray process. The limitation of PEDO:PSS is its low hydrophilic response that results in lower sensitivity and poor low relative humidity detection. The Fourier transform infrared spectroscopy (FTIR) data of the PEDOT:PSS material is presented in ***Figure 2-1*** [3]. The presented spectra have several characteristic peaks like those at 1097 cm^{-1} and 1162 cm^{-1} correspond to the stretching C-O-C bonds in ethylene dioxy group. The peak at 887 cm^{-1} correspond to S-C bonds in the polymerized PEDOT chain. The peaks at 1384 cm^{-1} and 1520 cm^{-1} can be attributed to the stretching of thiophene ring while those at 2852 cm^{-1} and 2921 cm^{-1} are because of C-H stretching vibrations. The peaks at 1632 cm^{-1} and 3428 cm^{-1} correspond to the O-H bending and stretching vibrations respectively [3].

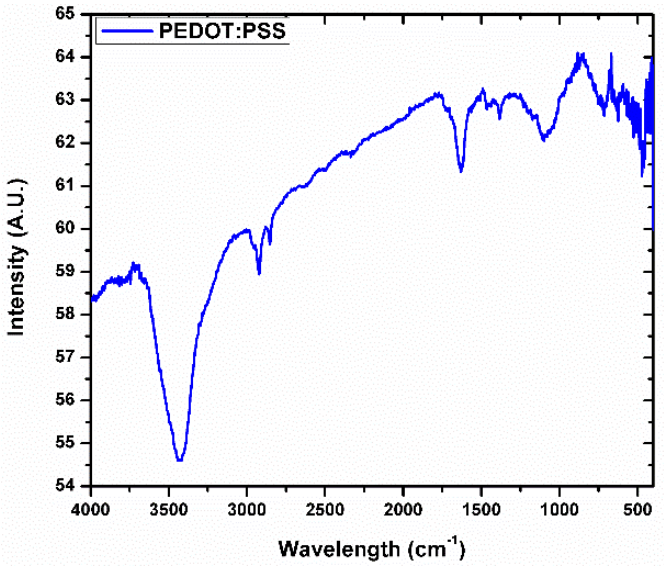

Figure 2-1: FTIR spectrum of pure PEDOT:PSS showing the chemical composition and purity of the polymer.

2) Another hydrophilic polymer used for the active layer fabrication of humidity sensors was polyvinyl alcohol (PVA). PVA with MW 9000-10000, 80% Hydrolyzed, was obtained from Sigma Aldrich. The ink was prepared by first dissolving 10 wt% PVA in de-ionized water. The mixture was then put on bath sonicator at room temperature for 30 minutes and was then kept on magnetic stirrer at 70ºC for 10 hours [1]. PVA has a natural affinity towards water and has a capacity to absorb fairly large amounts of water molecules in its dry state. These properties make it a good candidate for humidity sensor applications but the limitations with PVA are its highly insulating electronic properties. PVA based humidity sensors mostly work on the principle of change in the dielectric constant of the thin active film upon the change in absorption of the water contents. This in-return changes the device capacitance that can be electronically measured to quantitatively detect relative humidity. The problem with this approach, however, is that the low range humidity detection is poor that makes the sensors only viable for high humidity environments like food industry. The limitations can be reduced by making composite inks.

3) Based on the limitations of the polymers used in the initial research works, a better candidate for humidity sensing was selected that was another hydrophilic polymer polyethylene oxide (PEO). PEO average Mv 200,000 powder was purchased from Sigma. The ink was prepared by dissolving the powder in deionized water by 5 wt%/vol. The mixture was put on a magnetic stirrer at 40ºC overnight until a clear homogenous solution was formed. PEO is a semi-crystalline conductive polymer with a much better response towards humidity detection as compared to the above counterparts. Though, the humidity sensing properties of semi-crystalline PEO are not comparable to its amorphous form. To improve the sensing performance and low humidity detection, PEO was converted to its amorphous form

by heating it at 100ºC that is over its melting point. A comparison of the chemical changes in the structure of PEO before and after heating are presented in ***Figure 2-2*** [57].

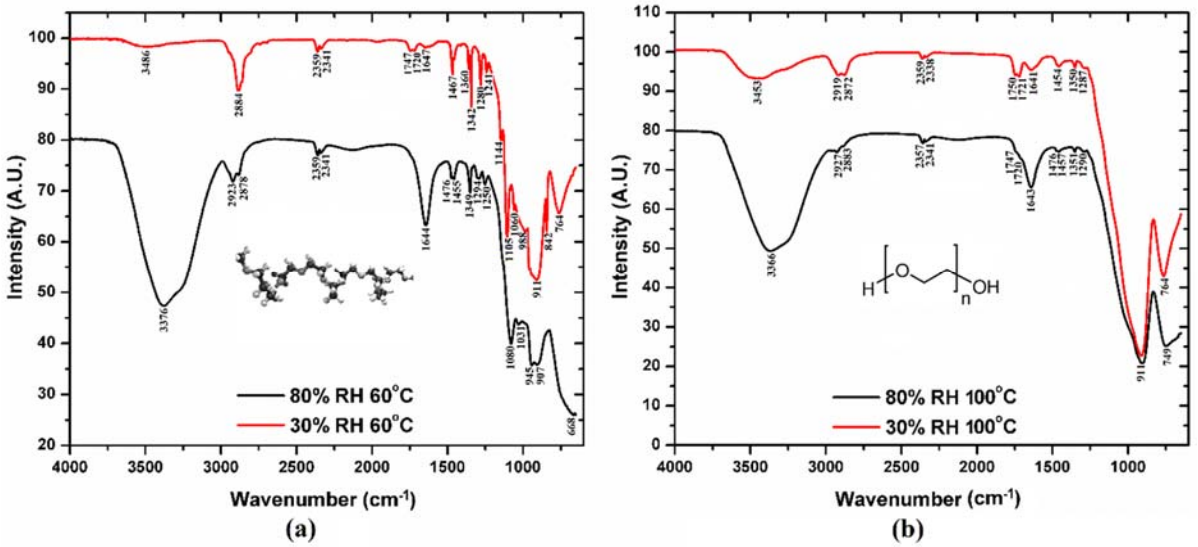

Figure 2-2: (a) FTIR spectra at 30% RH and 80% RH of the semi crystalline PEO thin film cured at 60ºC and (b) FTIR spectra of amorphous PEO thin film cured at 100ºC recorded at 30% RH and 80% RH.

FTIR spectrum of the low temperature PEO shows the characteristic peaks normally present in PEO. The triplet absorption bands of C-O-C stretching vibrations at 1060, 1105, and 1144 cm^{-1} confirm the semi crystalline phase of PEO showing that after the PEO film is cured at 60°C, it retains its crystallinity. The absorption bands in the region with wavenumber less than 1000 cm^{-1} are associated with CH_2 rocking bands. The bands at 1342 and 1360 cm^{-1} are attributed to the CH_2 wagging vibrations whereas the band at 1280 cm^{-1} corresponds to CH_2 twisting mode. The absorption bands at 1241 and 1467 cm^{-1} are ascribed to CH_2 symmetric twisting and CH_2 asymmetric bending respectively. The sharp peak at 2884 cm^{-1} corresponds to C-H stretching mode while two very low absorption bands at 2341 and 2359 cm^{-1} can be attributed to the second overtones of peaks at 1105 and 1144 cm^{-1}. The presence of OH group can be observed at 3486 and 1647 cm^{-1} showing physical adsorption and hydrogen bonded hydroxyl ions respectively. The intensity of these two bands is very low at 30% RH for the semi crystalline thin film which shows almost no affinity of the film to low concentration of OH^{-1} ions at low relative humidity. If we observe the FTIR spectrum of the semi crystalline thin film at 80% RH, the two OH bands appear to have largely grown in intensity and are slightly shifted to 1644 and 3376 cm^{-1} showing good affinity of the crystalline film towards high RH levels. Similar slight shifting was observed in low wavenumber peaks of PEO at high humidity level due to the invasion of water molecules but the film retained its semi crystalline nature. The FTIR spectra of the PEO after heating at 100°C for 30%

and 80% RH show that when PEO is heated beyond its melting temperature, it did not retain its semi crystalline phase and was converted into an amorphous polymer. The triplet peaks at 1060, 1105, and 1144 cm^{-1} showing crystallinity of PEO were totally diminished which means that PEO is no more in its semi crystalline phase. The other absorption bands at 1287, 1350, 1454, 2338, 2359, and 2872 cm^{-1} mostly resemble with the FTIR spectra of PEO film cured at 60°C showing that there are no other impure phases in PEO except losing its crystallinity. Most of the PEO signature absorption bands show broadening and weakening and some have been susceptible to disappear while others tend to overlap to form broader bands showing the typical characteristic of an amorphous polymer when heated through its melting point. The comparison of intensities of OH bands near 3400 cm^{-1} and 1640 cm^{-1} shown in the red curves of both films recorded at a low humidity level of 30% RH indicate that in case of amorphous film, the band intensity is considerably higher showing higher affinity of the amorphous polymer towards even low concentration of water molecules at low relative humidity levels. The changes in physical morphology of the fabricated thin films of crystalline and amorphous PEO are presented in ***Figure 2-3*** [57]. The microscopic image of the crystalline thin film of PEO cured at 60ºC shows large cracks representing the crystal boundaries. The crystals size is in the range of millimeters. The zoomed-in version of surface SEM image shows smooth solid surface of the crystals with cracks appearing at micro level if further magnified. The micro level observation of the thin film cured at 100ºC shows very rare occurrence of cracks in the film which means that the film is not in crystalline solid phase but possess an amorphous waxy solid like form. The cross-sectional SEM images of the three films deposited using different number of passes show thicknesses of ~200 nm, 300 nm, and 400 nm respectively.

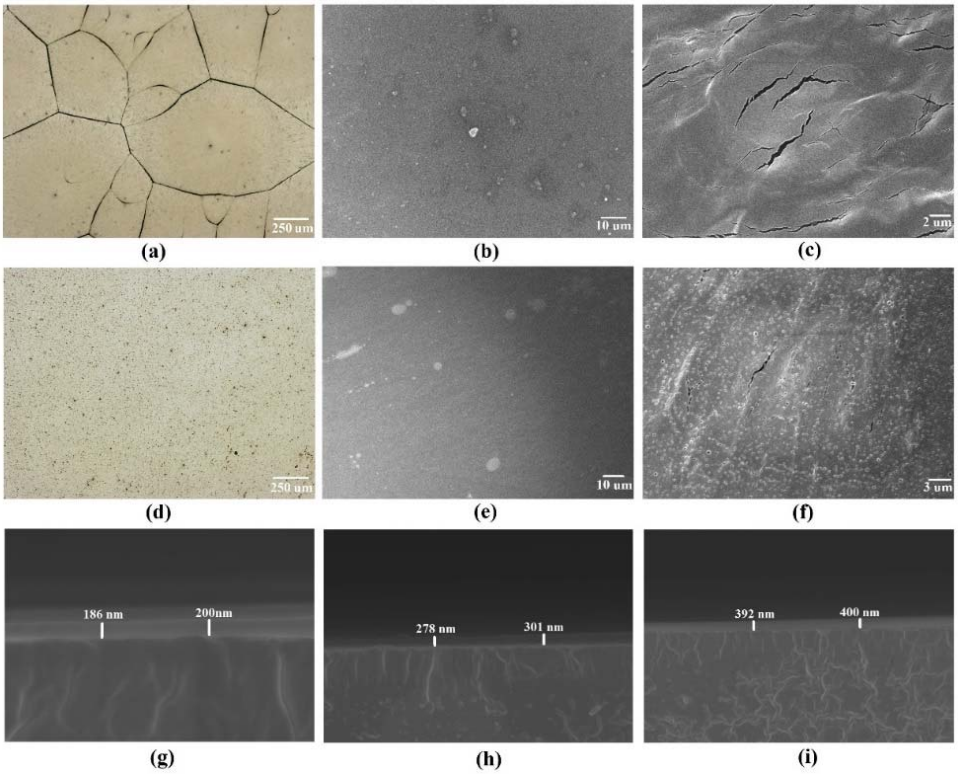

Figure 2-3: Surface morphology of the thin films showing (a) 60ºC cured film microscopic image, (b) low magnification SEM, (c) high magnification SEM showing cracks, (d) 100ºC cured film microscopic image, (e) low magnification SEM, and (f) high magnification SEM showing waxy solid amorphous film (g-i) cross-sectional SEM of three deposited films of different thicknesses.

Four types of hydrophilic conductive and insulating polymer materials of both organic and inorganic origin were used to fabricate the active layers of the sensing devices. Further research was done to introduce other material categories like 2D materials and composites to improve the sensing performance.

2.2.2 2D Materials

2D materials are in limelight these days for electronic devices. 2D materials possess unique chemical, electrical, and physical properties that can be helpful in many different applications including sensing devices. 2D flakes of transition metal di-chalcogenides (TMDs) have been used for various sensing applications including gas sensing, bio-sensing, photo-sensing, etc. [58–62]. Transition metal carbides (TMCs) have been used in their MXene phase mostly in catalysis, energy storage devices, and biosensors [63–72], etc. Large scale 2D TMCs are synthesized usually by selective etching [73], nano-casting [74], and CVD [75]. Synthesis and exfoliation of 2D hBN requires acid etching, chemical vapor deposition, complex chemical reactions, and other complex methods [76–78] that result in forcing the scientists to change their first choice for material selection. Some of the materials like MoS_2, Cr_3C_2, and Mo_2C have been exfoliated using a simpler

wet mechanical grinding process to achieve their 2D flakes [79–81]. 2D flakes of the materials used in this research work were synthesized by liquid assisted mechanical exfoliation method. Thin films of 2D flakes of transition metal carbides, dichalcogenides, and nitrides were tested for humidity sensing based on their large surface area to volume ratio and excellent abruption capacity. Water absorption generates both ionic and electronic current inside the thin film that results in change in resistance of the materials [82]. The details of the exfoliation technique are presented in ***Figure 2-4***.

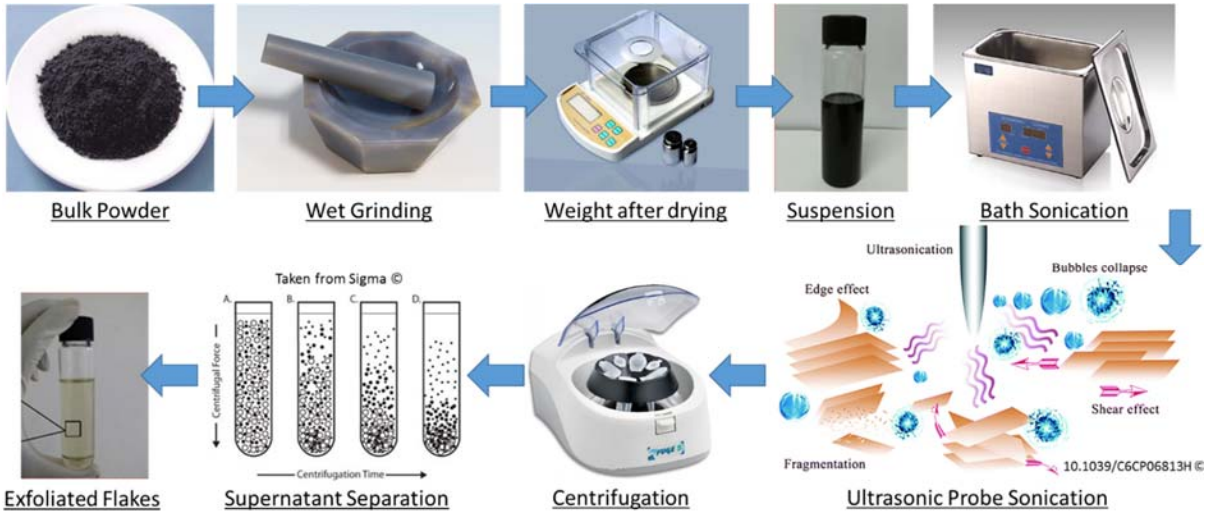

Figure 2-4: Step by step exfoliation process to synthesize 2D flakes from bulk powder of the desired materials.

The process involves wet grinding of the bulk powders of the target materials in a mortar with small amounts of solvent for 4 hours and then drying at room temperature. The dried powders obtained after wet grinding were dispersed in equal volume ratio of ethanol and water followed by probe sonication and centrifugation at 4000 rpm for 30 min. After centrifugation, the supernatants were taken out so that mono or few layered nano-sheets may be obtained. As obtained aqueous solutions were stirred for 12 hours to achieve a homogeneous solution [82].

2D flakes of Molybdenum Carbide (Mo_2C), Chromium Carbide (Cr_3C_2), hexagonal Boron Nitride (hBN), and Molybdenum Disulfide (MoS_2) were prepared using the exfoliation method as described above. The morphological and chemical properties of the exfoliated flakes were investigated to understand their behavior and predict their possible applications in sensors. The two transition metal carbides were exfoliated and the changes in their physical morphology were visualized through FE-SEM as presented in ***Figure 2-5*** [13,82].

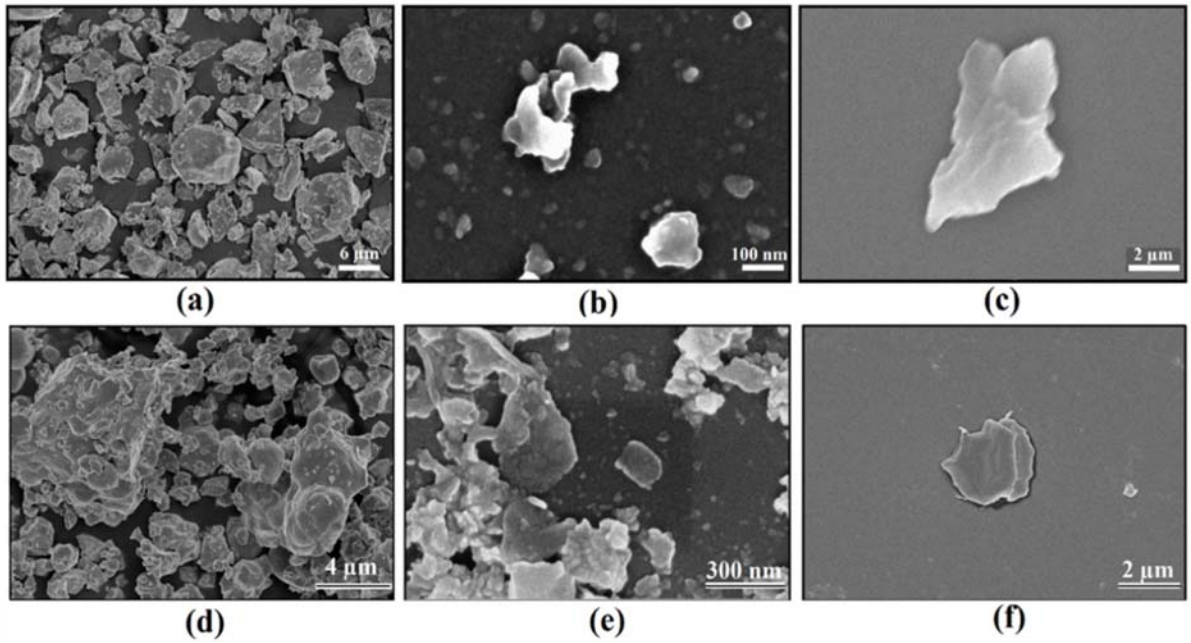

Figure 2-5: FE-SEM images showing thin film surfaces of (a) non-exfoliated bulk Cr_3C_2 powder, (b) exfoliated Cr_3C_2 crystal particles, (c) single 2D flake of exfoliated Cr_3C_2, (d) bulk Mo_2C, (e) exfoliated Mo_2C, and (f) a single, large exfoliated flake.

The image of the bulk Cr_3C_2 powder shows big bulky chunks of the material spread on the surface. The thickness and size of the chunks is in range of several micrometers. The SEM image of the thin film of exfoliated Cr_3C_2 shows large number of smaller particles and flakes distributed throughout the surface. There are also some large area flakes on the surface but their physical structure is like 2D. Same trend can be observed for Mo_2C after exfoliation.

Further details on the structure and morphology of the exfoliated 2D TMC flakes were studied through XRD spectroscopy and AFM imaging. The results for both Mo_2C and Cr_3C_2 are presented in ***Figure 2-6***.

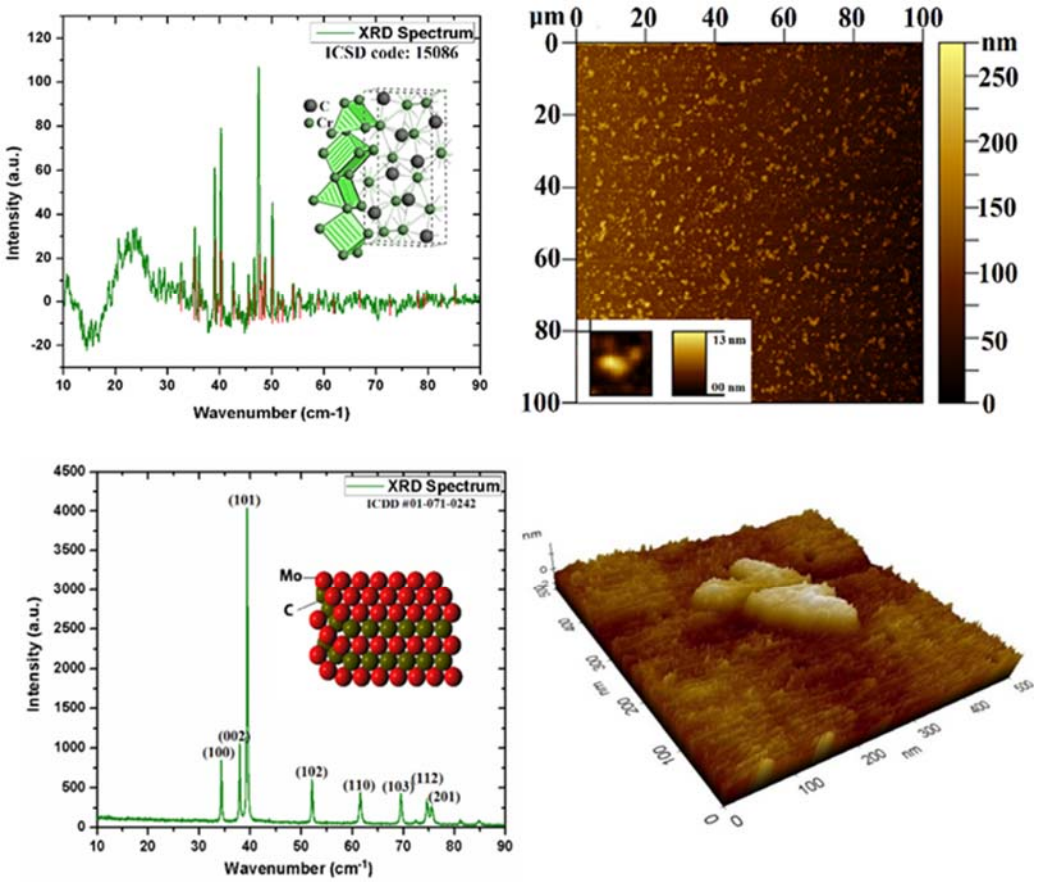

Figure 2-6: XRD crystallographic spectra of (a) Cr_3C_2, (b) surface AFM of the exfoliated Cr_3C_2 thin film with inset showing single flake (c) XRD of α-Mo_2C with layered hexagonal crystal structure, and (d) 3D AFM image of single Mo_2C flake.

AFM images show that the thickness of the Cr_3C_2 flakes range between ~9 nm to ~90 nm while the thickness is near ~6nm for Mo_2C. The single flakes have lower thickness in range of few nanometers while the higher thickness is mostly due to stacking and agglomeration of the particles on top of each other. Some flakes are thicker than others having comparatively higher number of stacked sheets in a single flake. The XRD results of the Mo_2C powder show that the material used in this work is in α-phase [83,84]. There are 3 phases of Mo_2C, α, β, and δ, having hexagonal, orthorhombic, and cubic structures respectively [84–86]. The obtained XRD peaks confirm that the phase used in this research work is the α-phase having a layered hexagonal crystal structure [67,68]. The crystal structure of Cr_3C_2 investigated using XRD ascertain the orthorhombic crystal structure of the material [87–89].

Hexagonal Boron Nitride was then exfoliated through the same process as described above and the physical morphology of the 2D exfoliated flakes was observed through FE-SEM and AFM. The flakes were suspended in IPA solvent and in a PEO polymer ink.

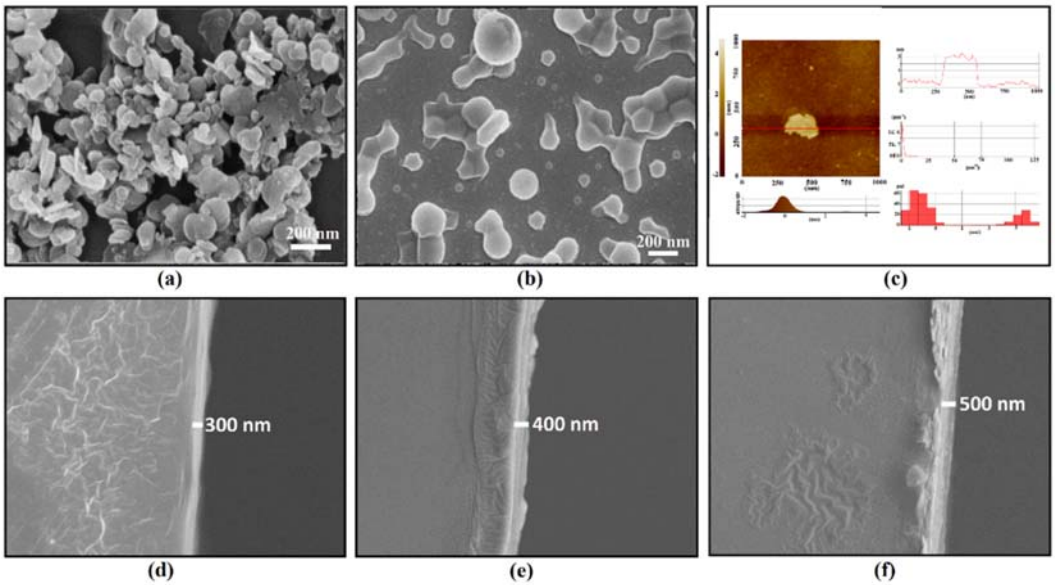

Figure 2-7: Physical morphology of the thin films showing (a) surface SEM of thin film of 2D hBN sheets, (b) surface SEM of composite active layer, (c) AFM image of single 2D hBN flake, (d-f) cross-sectional SEM of three deposited films with different thicknesses.

The results of physical morphology are presented in ***Figure 2-7***. The images show petal like microstructure and lateral size of the as exfoliated flakes. The surface SEM of the composite of hBN and PEO is also presented which shows that the flakes are thoroughly mixed in to the polymer matrix and are well dispersed that is a result of a homogenous suspension and uniform coating. The AFM image of a single flake and its height profile are show that the nominal flake thickness is in range of 3-4 nm while the size of flakes is around 200 nm as shown by the SEM images. This thickness ascertains that the hBN has been exfoliated into few layered 2D flakes with high surface area to volume ratio.

Lastly, MoS_2 was exfoliated into 2D flakes and the SEM and AFM results to study the physical morphology are presented in ***Figure 2-8*** [15].

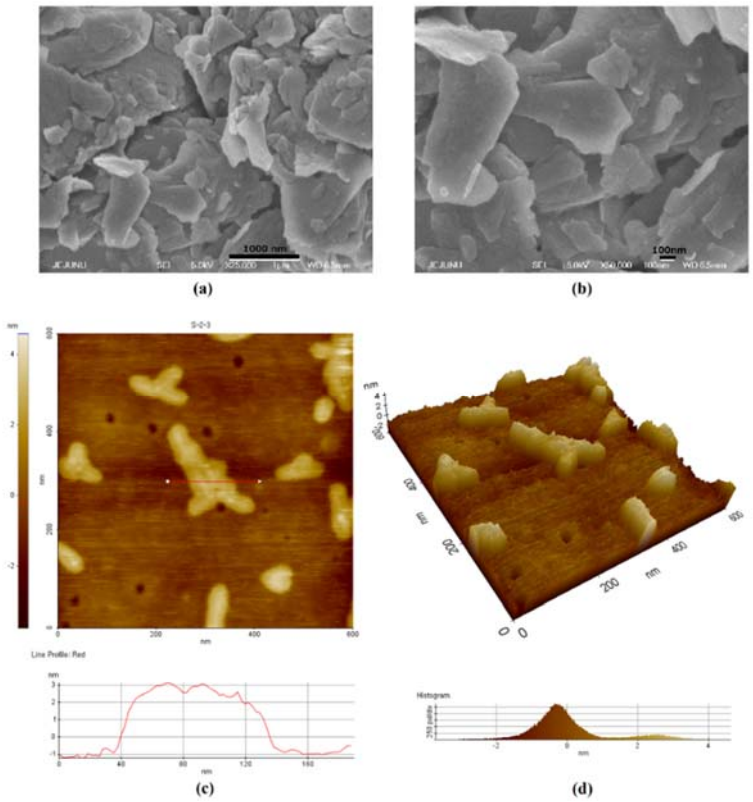

Figure 2-8: SEM and AFM of the active layer showing (a) MoS_2 active layer with highly porous surface, (b) 2D MoS_2 flakes, (c) 2D surface profile and AFM line profile, and (d) 3D surface profile by AFM.

The SEM images of MoS_2 thin film at different magnifications show clear 2D sheets of the material and a highly porous active layer ideal for physisorption and bonding of antibodies on to the film. This facilitates direct electron transfer from the antibody-antigen complex to the electrodes for higher sensitivity [90]. The higher surface roughness also reduces the non-specific absorption of proteins [91]. The SEM images also indicate that the cumulative surface area of the thin film has been increased, and the 2D flakes are also capable to possess semiconducting properties that would be absent in case of bulk material. The AFM images of MoS_2 flakes indicate 3-4 nm nanometer thick flakes ascertaining the exfoliation of the bulk into few layered sheets.

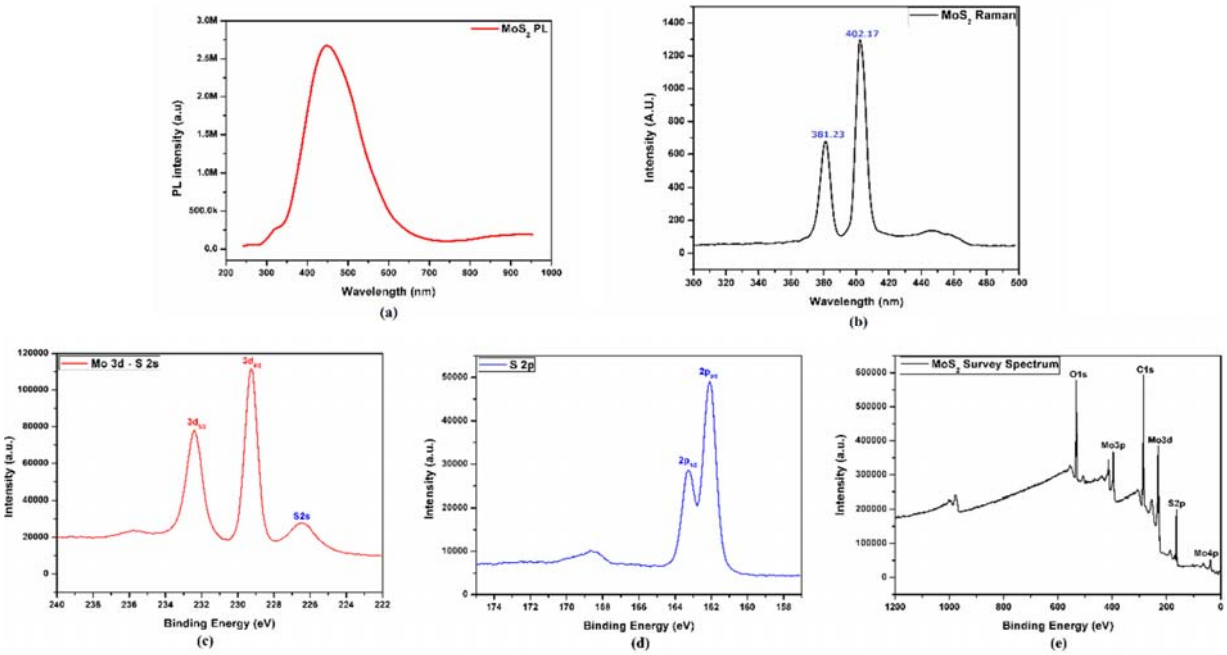

Figure 2-9: Chemical characterizations including (a) PL emission spectrum, (b) Raman spectrum, (c-e) XPS spectra of MoS_2 active layer.

Figure 2-9(a) shows the PL emission spectrum of MoS_2 flakes with a broad peak at 440 nm. Usually this broad peak appears at 652 nm in case of large monolayer sheets exfoliated by scotch tape method but in this case, the shift in peak is due to direct and indirect bandgap in monolayer and few layer flakes respectively. This also might be due to mechanical grinding resulting in smaller flakes and possibly few quantum dots giving rise to quantum confinement effects [92]. The Raman spectrum results presented in ***Figure 2-9***(b) shows that the phonon modes of exfoliated MoS_2 flakes lie at 381.23 nm and 402.17 nm ascertaining the attributes of Raman analysis for exfoliated MoS_2 flakes [93]. The XPS results presented in ***Figure 2-9***(c-e) confirm the presence of only MoS_2 as the active layer material with no contamination as such except the Carbon and Oxygen from the atmosphere [94]. The atomic ratio of the thin film was 1: 2 for Mo:S that ascertains the presence of MoS_2 flakes. The exfoliated flakes of all the four materials shows expected physical and chemical properties that can be ideally used to fabricate the active layer of environmental and biosensors.

2.2.3 Hybrid organic/inorganic composites

1) A conducting/insulating polymer/polymer nanocomposite of PEDOT:PSS and hydrophilic PVA was prepared to fabricate the active layer of wide range humidity sensor with both capacitive and impedance based output. Polyvinyl alcohol (PVA MW 9000-10000, 80% Hydrolyzed) was obtained from Aldrich and Poly (3, 4-ethylenedioxythiophene)

Polystyrene Sulfonate (PEDOT:PSS) used was Orgacon EL-P5010 solvent based paste with 3 wt% solid content. The PEDOT:PSS/PVA composite ink was prepared by first dissolving 10 wt% PVA in de-ionized water. The mixture was put on bath sonicator at room temperature for 30 minutes and was then kept on magnetic stirrer at 70ºC for 10 hours. After the formation of uniform solution of PVA, the solution was divided in to three equal parts. Then PEDOT:PSS paste was added by 10 wt%, 20 wt% and 30 wt% (with solid content 0.3 wt%, 0.6 wt% and 0.9 wt%) in three separate solutions of the same quantity as that of the three PVA solutions prepared. These solutions were magnetically stirred three times for 30 minute interval each. The three PVA solutions prepared before were then mixed separately with three PEDOT:PSS solutions to get three composites with 5 wt% PVA in each of them and 5 wt%, 10 wt% and 15 wt% (0.15 wt%, 0.3 wt% and 0.45 wt% solid content) PEDOT:PSS. All the final mixtures were kept on magnetic stirrer at 25ºC for 5 hours. The chemical structures of the two materials used in the composite along with the FTIR spectroscopy data of the composite are presented in ***Figure 2-10*** [1]. The physical morphology of the composite has been investigated through microscopy and SEM that shows homogenous mixing of the two components as shown in ***Figure 2-10***.

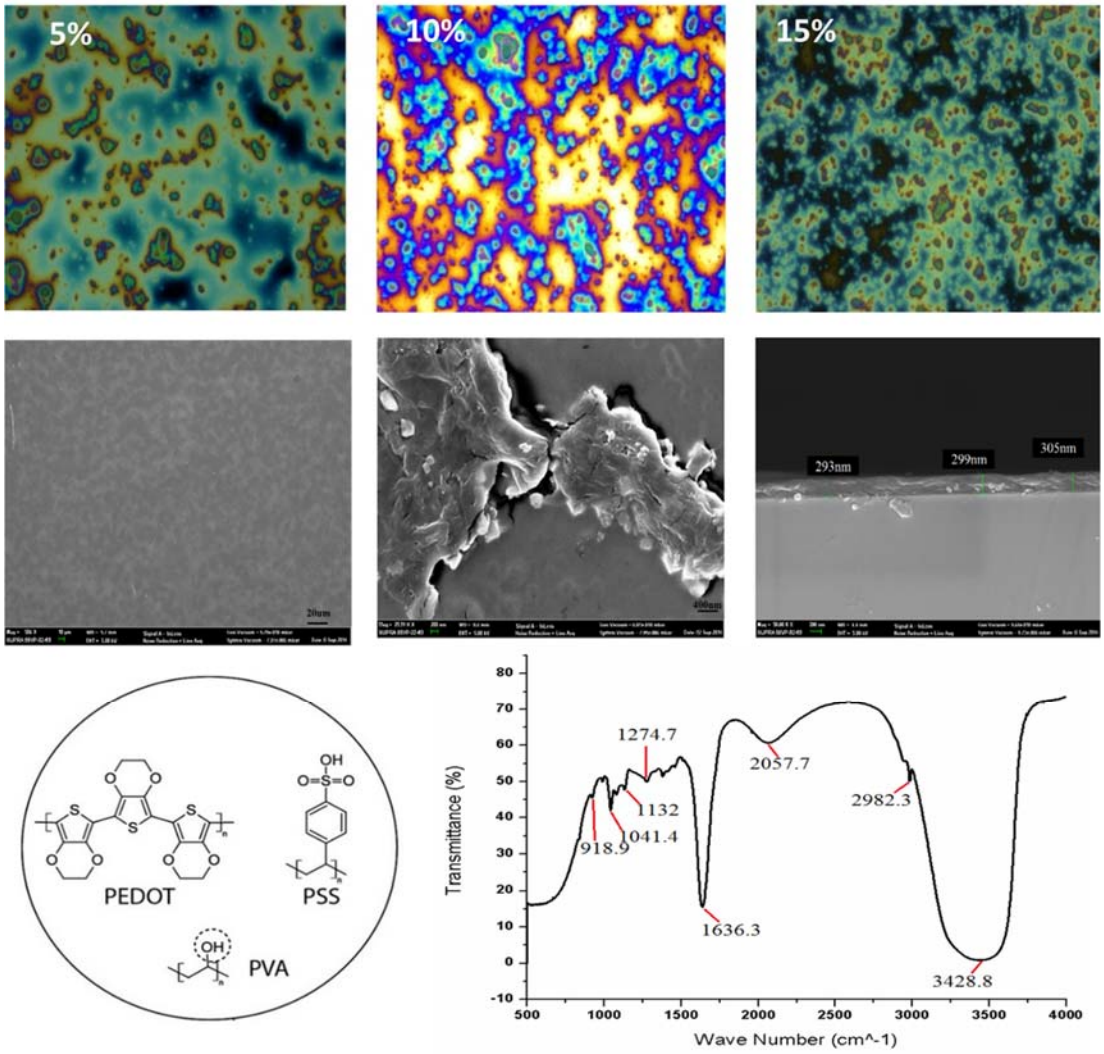

Figure 2-10: Chemical structures of PVA & PEDOT:PSS composite, FTIR spectrum of the composite, and Microscopic & SEM images with different composite ratios.

PEDOT and PSS make bonds between SO_3^- group of PSS and S^+ group of PEDOT while OH (Hydroxyl group) of the PVA is free. There is no proper bonding between PEDOT:PSS and PVA but there is quite an interaction between them [95]. Adding more PEDOT: PSS to a fixed amount of PVA will decrease the number of free hydroxyl ions in the solution [96] that are responsible of trapping water molecules for humidity sensing. This suggests that too much PEDOT: PSS can affect the performance of the sensor in terms of response towards low humidity but an optimized concentration will help increasing the overall conductivity of the composite film and decreasing the hysteresis and recovery time in return by preventing the phenomenon of trapping [96].

2) Another polymer/polymer composite of BEHP-co-MEH:PPV and super-hydrophilic PAAPSS was prepared for humidity sensing active layer fabrication. Poly{[2-[2',5'-bis(2''-ethylhexyloxy)phenyl]-1,4-phenylenevinylene]-co-[2-

methoxy-5-(2′-ethylhexyloxy)-1,4-phenylenevinylene]} (BEHP-co-MEH:PPV) powder with average molecular weight around 18,900, Poly(acrylic acid) partial sodium salt <1000 µm particle size (99%) (PAAPSS), and Chloroform were purchased from Sigma Aldrich. The ink for active layer was prepared by dissolving 1% wt/vol. BEHP-co-MEH:PPV in chloroform solvent. The mixture was put on bath sonicator at 30ºC for 60 minutes and was then kept on magnetic stirrer for 2 hours. The powder of PAAPSS was ground to reduce the particle size that will allow uniform dispersion in the composite ink. After the homogenous solution of BEHP-co-MEH:PPV was ready, PAAPSS powder was added to the solution in three different weight by volume ratios of 1%, 3%, and 5%. The resulting composite inks were continuously put on mechanical shaker at 200 rpm to avoid agglomeration and keep the PAAPSS particles suspended. PAAPSS is not soluble in chloroform and it does not absorb any of the solvent contents, so, the particles of PAAPSS remain the same size and do not swell like in case of water and other affine solvents. The structures of the composite materials and the FTIR spectra are presented in ***Figure 2-11*** [12]. Four samples were prepared and were differentiated based on the weight percentage of poly(acrylic acid) partial sodium salt. Sample1 corresponds to 0% PAAPSS (only BEHP-co-MEH:PPV), sample 2 contains 1% wt/vol PAAPSS in BEHP-co-MEH:PPV solution, sample 3 has 3%, while sample 4 has 5% PAAPSS. The samples were pre-processed with drying and humidifying treatments by exposing them to a 90% RH environment for 10 s for humidification and a 0% RH environment for 10 s for drying. The samples were then quickly sealed in glass slabs and were fixed in a sealed mini chamber in FTIR analyzer to let them retain the levels of humidity in the films after pre-processing.

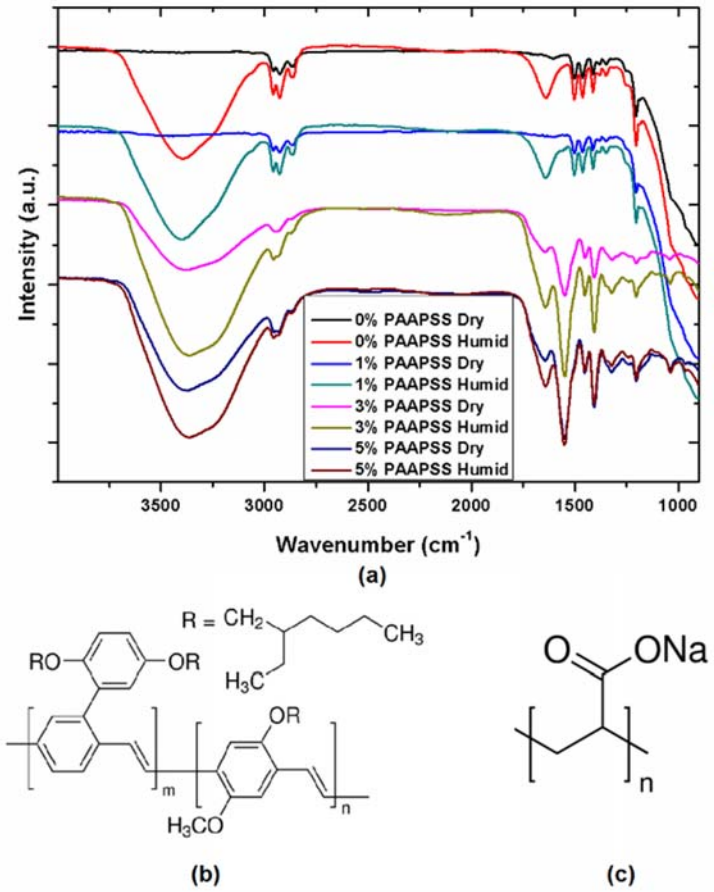

Figure 2-11: Chemical properties of the active layer (a) FTIR spectra of the four samples at dry and humid states, (b) chemical structure of BEHP-co-MEH:PPV, and (c) chemical structure of Poly(acrylic acid) Partial Sodium Salt.

FTIR spectra of the four prepared samples were observed between 500 and 4000 cm^{-1} in both dry and humid states. The shift in the peaks was observed to determine the working principle of the humidity sensors. Most of the peaks correspond to the in-plane C–H bands. The bands at 1036 and 1251 cm^{-1} are attributed to aryl alkyl ether (C–O–C) symmetric and asymmetric stretching, respectively. Phenyl-oxygen stretching can be observed at 1201 cm^{-1}. The bands at 1386 and 1454 cm^{-1} exhibit symmetric and asymmetric C–H bending, respectively, in the CH_2 group. The two sharp bands at 2925 and 2955 cm^{-1} are assigned to asymmetric C–H stretching in the CH_2 and CH_3 groups respectively, while the band at 2865 cm^{-1} is assigned to symmetric C–H stretching in CH_3 [3]. The multiple medium intensity peaks between 1400 cm^{-1} and 1500 cm^{-1} and the one at 1603 cm^{-1} show the usual pattern for aromatic C=C stretching region. These peaks presenting C–H and C=C groups affirm the given structure of BEHP-co-MEH:PPV co-polymer in the thin film active layer. There is a notable difference in certain peaks presented for the films for dry and humid states and for different concentrations of PAAPSS. The intensity of the peaks at 1505 cm^{-1} representing C=O carboxyl bending and 1505 cm^{-1} $–COO^-$ asymmetric stretching become higher with increasing concentration of

PAAPSS [97]. The band intensity between 3300 cm^{-1} and 3700 cm^{-1} presenting non hydrogen-bonded OH groups in vapor phase increases immensely for humid samples showing the major contribution in humidity sensing behavior of the composite thin film [98]. The mentioned band becomes notably larger in magnitude for higher concentrations of PAAPSS indicating the major role played by the super hydrophilic polymer in water vapor adsorption. Also the change in magnitude of the medium intensity peak at 1641 cm^{-1} shows the water absorption through hydrogen bonding that is supposed here to contribute in the detection of lower humidity levels. Overall, the BEHP-co-MEH:PPV polymer provides a matrix to embed the PAAPSS particles in the thin film. The material itself is sensitive towards humidity changes but the sensitivity is much lower. Addition of PAAPSS increases the sensitivity several folds while maintaining the stability.

The surface SEM images shows the surface morphology of the thin films at different magnifications. The images indicate the presence of PAAPSS as white granules in samples 2-4. The number and size of the white particles increase with increasing concentrations of PAAPSS. The SEM images also indicate highly rough surface morphology of the active layer that is confirmed by the 3D surface profiles presented in ***Figure 2-12***(i-l).

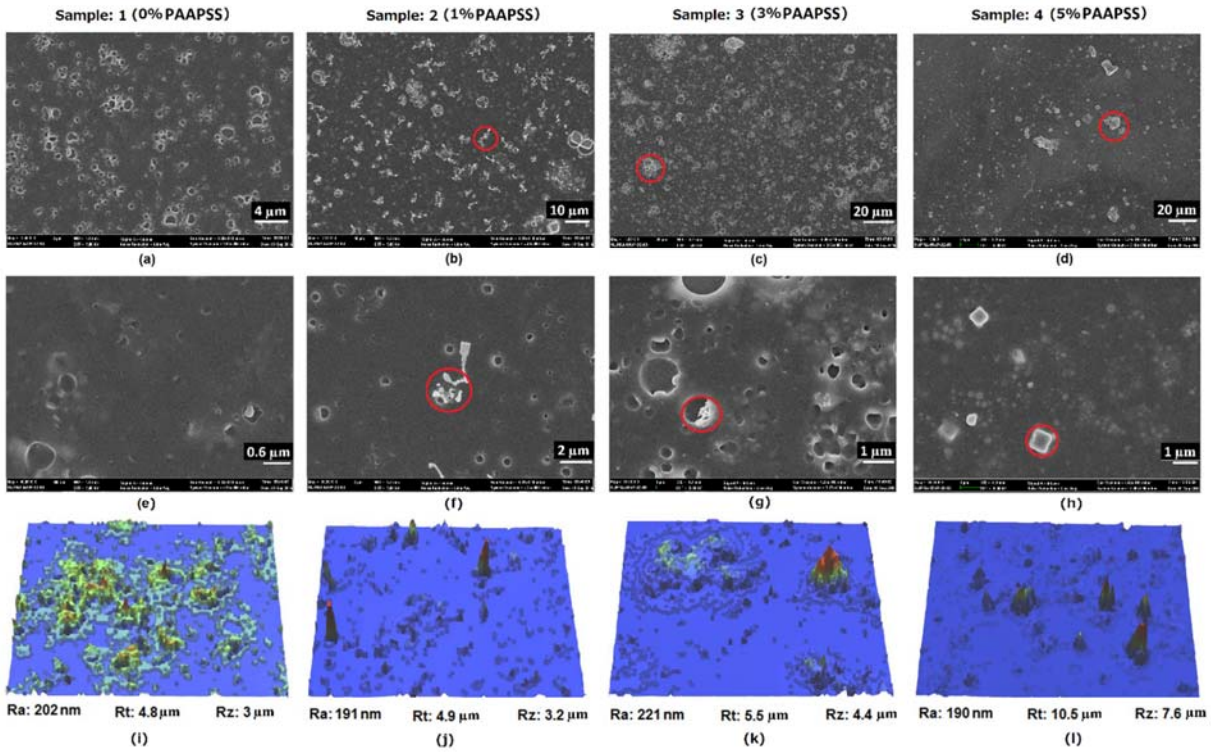

Figure 2-12: Surface morphology of the samples showing FE-SEM images at lower magnification of (a) sample 1, (b) sample 2, (c) sample 3, and (d) sample 4. SEM at higher magnification of (e) sample 1, (f) sample 2, (g) sample 3, and (h) sample 4. 3D surface profiles with roughness profiles of (i) sample 1, (j)

sample 2, (k) sample 3, and (l) sample 4.

We can see that the maximum roughness height R_t and the average distance between the peaks and valleys R_z increase considerably with increasing concentration of PAAPSS while the average surface roughness remains almost the same. The reason is the presence of the bigger particles of PAAPSS on the surface spread all over the film. The film thickness without PAAPSS was found to be ~442 nm using cross-sectional SEM as presented in supplementary Figure S2. The granules of PAAPSS do not increase the base film thickness but are spread at random locations. The average surface roughness when compared to the film thickness shows high surface roughness of the active layer. The parameters are suitable for high sensitivity and quick response time for a humidity sensor.

3) Finally, a hybrid nano-composite of 2D hBN flakes and PEO was prepared to fabricate the active layer of humidity sensors. An ultrafine powder of hexagonal Boron Nitride (hBN) was purchased from Graphene Supermarket. The average particle size of the powder was ~70 nm with a 99% purity. Isopropyl alcohol (IPA) with a purity of >99.7% and Polyethylene oxide (PEO) powder with an average molecular weight (M_v) of 200,000 were purchased from Sigma Aldrich. 2D hBN was exfoliated through the process described earlier. The PEO ink was prepared by dissolving the powder in deionized water by 5 wt%/vol. The mixture was put on a magnetic stirrer at 40ºC overnight until a clear homogenous solution was formed. After the two solutions were ready, the final ink for the active layer was prepared by homogenously mixing them in equal volume ratio of 1:1. The final ink was placed on a magnetic stirrer for 5 hours at 1500 rpm.

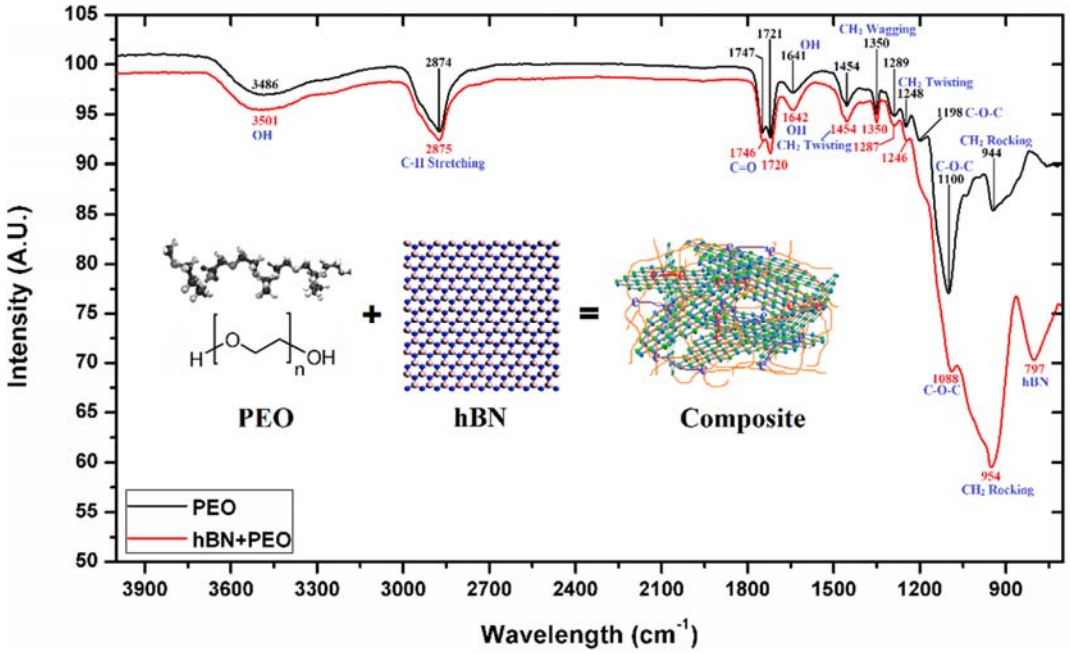

Figure 2-13: (a) FTIR spectra of pure PEO (black) and hBN + PEO composite (red) showing the characteristic peaks of the two materials with schematic representing the structure of the composite.

The FTIR spectroscopy results presented in ***Figure 2-13*** show the chemical structure of pure PEO polymer and the composite. Both the curves are plotted together for comparison purpose. The major difference in the spectroscopy data lies in the 797 cm^{-1} peak that represents the presence of hBN in the composite and can be attributed to out of plane B–N–B bending vibration (A_{2u} mode) [99]. The other labelled signature peaks attributed to C-H stretching mode, C=O, CH_2 twisting, rocking bands, and wagging vibrations modes, and triplet absorption bands of C-O-C stretching vibrations, confirm the presence of pure PEO in the composite. As the composite was heated beyond the glass transition temperature of PEO for curing the active layer thin film, the crystallinity of the polymer was reduced upon cooling down that is eminent from the diminishing of the triplet C-O-C peaks which represent the extent of crystallinity of PEO. The wide peak near 3500 cm^{-1} shows adsorbed OH- groups while the peak at 1640 cm^{-1} represents the bonded OH- groups [57]. The magnitude of the peak at 1640 cm^{-1} is slightly higher in case of the composite that shows its strong affinity towards water molecules which makes it perfect for the humidity sensing application.

4) Other carbon and graphene nano-ribbons based composites with polymers acting as binders were prepared for the fabrication of temperature sensors and human posture detection sensors. Activated Carbon with 100 mesh particle size in powder form, PVDF (Polyvinylidene fluoride), Toluene, and NMP (N-Methyl-2-pyrrolidone) were purchased from Sigma Aldrich. PVAc (Polyvinyl Acetate) beads by GPC with average Mw ~100,000 were used. 0.2 mm thick PET (Polyethylene Terephthalate) roll was used as substrate. Ink for active layer was synthesized by mixing

activated carbon with PVDF in 9:1 by weight. The contents were dissolved by 15 wt% in NMP solvent. The solution was placed on mechanical shaker at room temperature for 10 hours and was then kept on magnetic stirrer for 1 hour. The synthesized ink for micro-gravure printer had a viscosity of 20 cps and density of 1120 kg/m^3. The ink for protective coating was synthesized by dissolving 10% weight/volume PVAc in toluene solvent [100]. The mixture was placed on magnetic stirrer at 50 ºC for 3 hours to get a uniform homogenous solution and after that the inks were ready to be used for sensor fabrication.

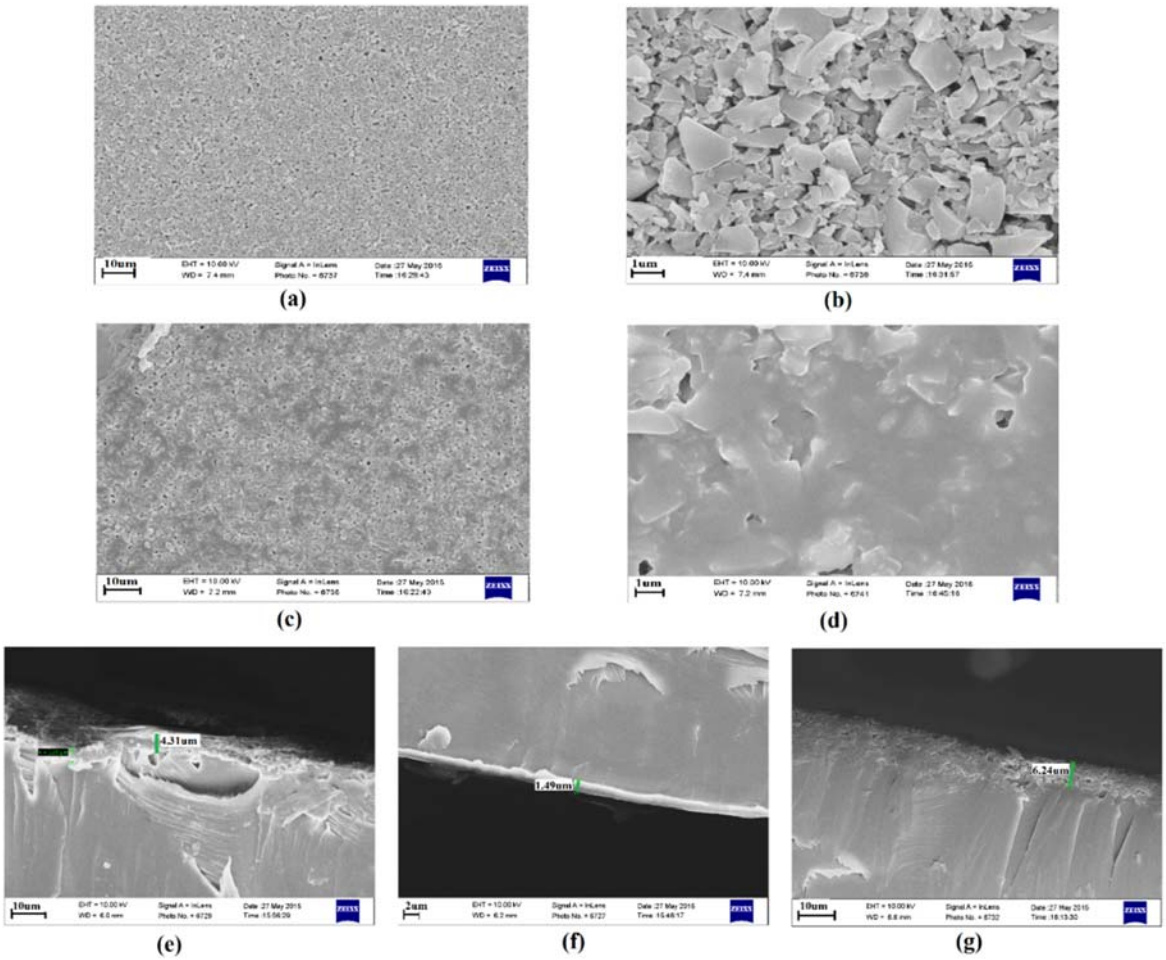

Figure 2-14: SEM images of the fabricated films. Surface SEM profile of the un-protected samples with scale 10 µm (a) and scale 1 µm (b), surface SEM profile of sample protected using micro-gravure printing with scale 10 µm (c) and scale 1 µm (d), cross-sectional SEM image of the un-protected film (e), PVAc coating only (f), and overall protected sensor (g).

The surface profile results shown in ***Figure 2-14*** clearly indicate that the active carbon layer had a more rough surface finish as compared to the finalized device after protective coating. The protective coating is not affecting the active layer beneath and just provides fortification to the overall device. The high surface roughness indicates loosely

arranged particles in the film displaying room for their mechanical motion on the application of external force upon the sensing layer through bending at different angles. The movement of particles by application of force improves the connection between them when the sensor is bent in negative direction thus reducing the device resistance and vice versa. These layer characteristics make the sensing layer suitable for flex sensor application.

5) The basic material for the fabrication of the active portion of the sensors was the commercially available conductive filament by BACKMAGIC3D with the diameter of 1.75 mm and volume resistivity of 0.6 Ω-cm. The filament formulation comprises of a composite of poly (lactic acid) (PLA) and graphene nano rods (GNR) that make it electrically conductive.

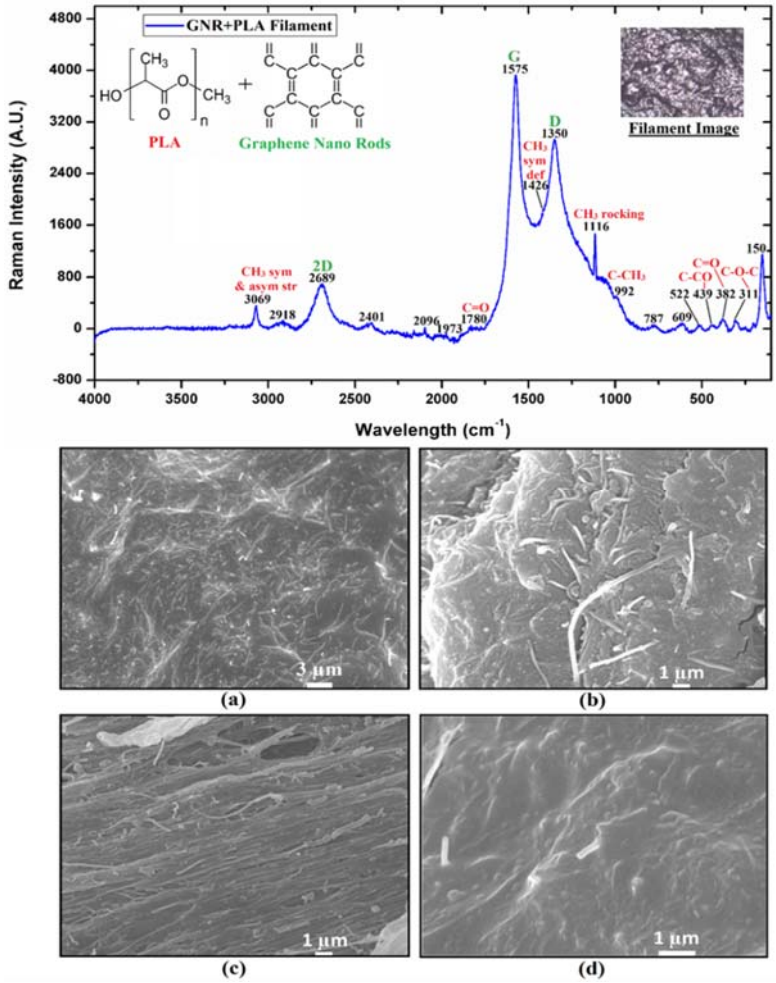

Figure 2-15: Raman spectroscopy data of the GNR-PLA 3D printing conductive filament showing the chemical structures and the different signature peaks of the two materials present in the composite and FE-SEM images showing morphology at different magnifications of (a) filament surface before printing, (b), filament cross-section before printing, (c) filament surface after printing, and (d) filament cross-section after printing.

FE-SEM images presented in ***Figure 2-14*** shows the microscopic structure of the material. The first two images

present the morphology of the filament surface and the filament cross-section before printing. Graphene nano-wires (GNR's) can be seen embedded inside the polymer matrix in random directions [101]. Cracks and dis-oriented graphene ribbons can also be seen in the broken cross-section of the filament before printing. The overall structure remains similar to that of initial one before printing. The cross-sectional image of the filament after printing shows the disappearance of cracks due to melting of the polymer. It also shows some embedded graphene ribbons that seem to have been a bit aligned after printing as verified by the surface morphology of printed filament.

The results of Raman spectroscopy show three very significant signature peaks of graphene at 2689 cm^{-1} (2D), 1575 cm^{-1} (G), and 1350 cm^{-1} (D) [102–105]. The difference in Raman spectroscopy data for the identification between graphene flakes, MWCNTs, and graphene ribbons lies in the intensity of the D band [106]. The intensity of D band in case of MWCNTs is lower as compared to the G and 2D bands while in case of graphene nano ribbons, the intensity of all the three signature bands are almost comparable [101,107]. This confirms the presence of graphene in the form of nano-ribbons in the composite that is ideal for high conductivity and strength for 3D printing applications. The other peaks in the spectrum labelled in the figure correspond to different functional groups and bonds present in PLA [108–111].

2.3 Bio Materials

Different biological materials were used in this research work for the fabrication and characterization of immunosensors. These include antibodies, antigens, blocking agents, and functionalization materials. Three different types of antibodies were used that can act as the receptors to their specific antigens. Detection of the antigens is important to diagnose and predict numerous diseases and irregularities in the human health. The anti-Prostate-specific antibody and the antigen were purchased from Sigma. The antibody had a protein concentration of ~1mg/ml while the antigen solution had ~0.2-0.6mg/ml protein content. Anti-Mouse IgG antibody buffered aqueous solution with concentration of 10-20mg/ml and normal mouse IgG antigen with a concentration of 1mg/ml were purchased from Sigma. NF-κB p65 rabbit mAb antibody with 100 µg/ml BSA solution was purchased from Cell Signaling Technology. NF-κB (p65) control peptide human antigen with ~1mg/ml protein concentration was purchased from Sigma. 30% Bovine serum albumin (BSA) solution in sodium chloride for blocking NSA was purchased from Sigma. 96% Butyltrichlorosilane (BTS) surfactant for functionalization was purchased from Sigma.

The surface of the few layered 2D sheets based active region was functionalized through silane based method using 2 vol% butyl-trichlorosilanes BTS [112–117]. This step is eminent to improve the specificity and reduce the non-specific absorption [118]. As a brief summary, the MoS_2 thin films submerged in the solution of ethanol and water (90% and 10% respectively) for 1 hour to produce free hydroxyl (OH) groups on MoS_2 surface [112,116]. Afterwards, for surface functionalization, BTS was added drop by drop in the solution at 2% vol/vol during continuous mechanical shaking. The Si atoms of BTS are attached to the MoS_2 surface via silane bonding. The samples were gently washed by IPA, dried with N_2, and were then heated at 110ºC for 60 min. After functionalization, the sensors were submerged in antibody solution containing BSA as the blocking agent and were incubated for antibody attachment to the SAMs. FTIR spectroscopy was done to study the boding between the MoS_2 active layer, the SAMs, and the antibody receptors. The FTIR spectrum of functionalized MoS_2 has been shown in ***Figure 2-16***.

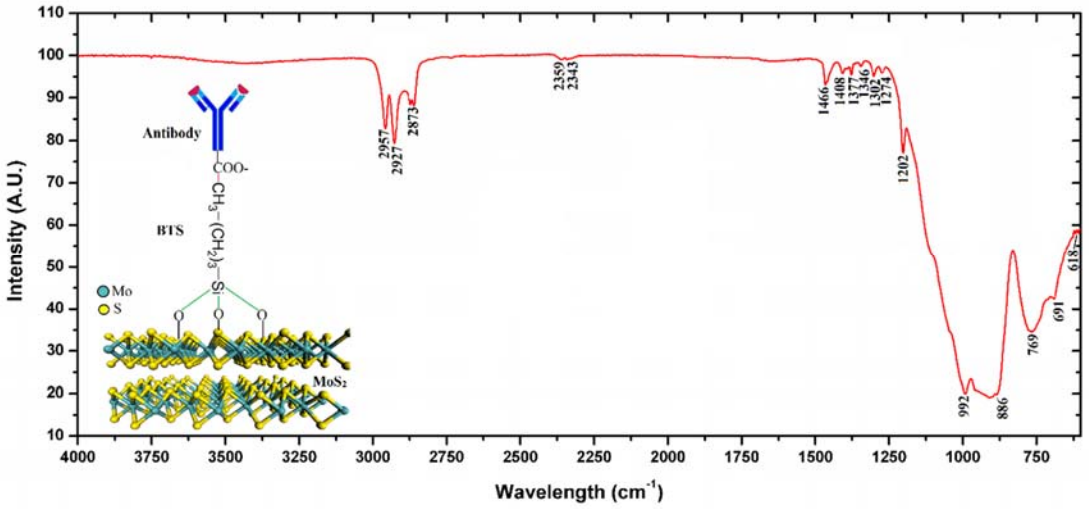

Figure 2-16: FTIR spectrum of functionalized MoS_2 and the schematic diagram showing attached BTS SAM's and antibodies on to the surface.

The absorption bands at 2343 and 2359 cm^{-1} may correspond to silane bonding [119]. The absorption peaks at 2873 and 2927 cm^{-1} correspond to asymmetric and symmetric stretching vibrations of methylene (CH_2) group whereas the absorption peak at 2957 cm^{-1} is attributed to the methyl (CH_3) stretching vibration [120,121]. This triplet band confirms the presence of alkyl-silane bonding on the MoS_2 surface. The absorption bands at 1377 and 1408 cm^{-1} may be assigned to CH_3 deformation and C-O-H bending. The absorption peaks at 1202, 1274, 1302 and 1466 cm^{-1} are assigned to C-C stretching, C-O stretching, out of plane C-H bending and C-H bending (scissoring) respectively that can be attributed to antibody attachment to the silane. The peak at 992 cm^{-1} can be assigned to the Mo-S band [120]. The absorption peak at 886 cm^{-1} may be assigned to the Si-O group, while the absorption band at 769 cm^{-1} is assigned

to Si-C group showing interaction between MoS_2 and silane. In the functionalized of thin films, the silane molecules displace the adsorbed water or OH groups from the MoS_2 surface. Because the water molecules tend to absorb on the defects rather than the perfect surface, it is clear that the silane moieties displace the water molecules from these defects [119,122]. These defects serve as the anchoring points (chemisorption) from which the polymerized BTS molecules can extend and cover larger areas of 2D MoS_2 flakes (physisorption) [119,122]. This method almost ensures that even if the defects are not perfectly similar in the flakes, the resulting functionalization will be repeatable [123] due to covering large area of flakes with BTS and the sensor results for multiple trials and samples with little error prove the repeatability [15].

A standard protocol with few modifications was adopted for immobilization of the antibodies. The antibodies were first diluted in saline/PBS to make solutions of 1μg/ml protein concentration. 3% BSA was added to the antibody solutions for blocking and minimize the non-specific absorption (NSA) [124]. The fabricated sensors were then submerged into these solutions and were left for 1 hour on mechanical shaker for incubation. As a result, the antibodies/receptors were thoroughly physisorbed into the MoS_2 sensing layer with the blank regions blocked by the BSA. The functionalized surface enables covalent bonding of the antibodies in addition to just flat dispersion on surface that is significant to improve the specificity. The sensors were rinsed with DI water to remove any traces of non-immobilized molecules. The immobilization and specific binding was investigated by laser fluorescence microscopy. The as used NF-κB and IgG give red colored fluorescence for the antigens and green for antibodies. Glass slabs without electrodes coated with MoS_2 were incubated in 1μg/ml antibody solution for NF-κB and 10μg/ml for IgG. Similar treatment was used for blocking and immobilization. The samples were then treated with three different concentrations of IgG antigen and a single concentration of NF-κB antigen. The laser confocal microscopy gives fluorescence only at the locations of immobilization for both antibodies and antigens. This process makes sure that only immobilized antibodies and bound antigens play their role in sensing behavior of the devices. No green fluorescence should be observed on the areas that are blocked and do not have immobilized antibodies. Similarly, no red fluorescence should be visible outside that area to confirm specific binding and selectivity of the sensor. The results presented in ***Figure 2-17*** [15] show no antigen (red) fluorescence for control sample while both red and green colors are observable for different concentrations of antigens.

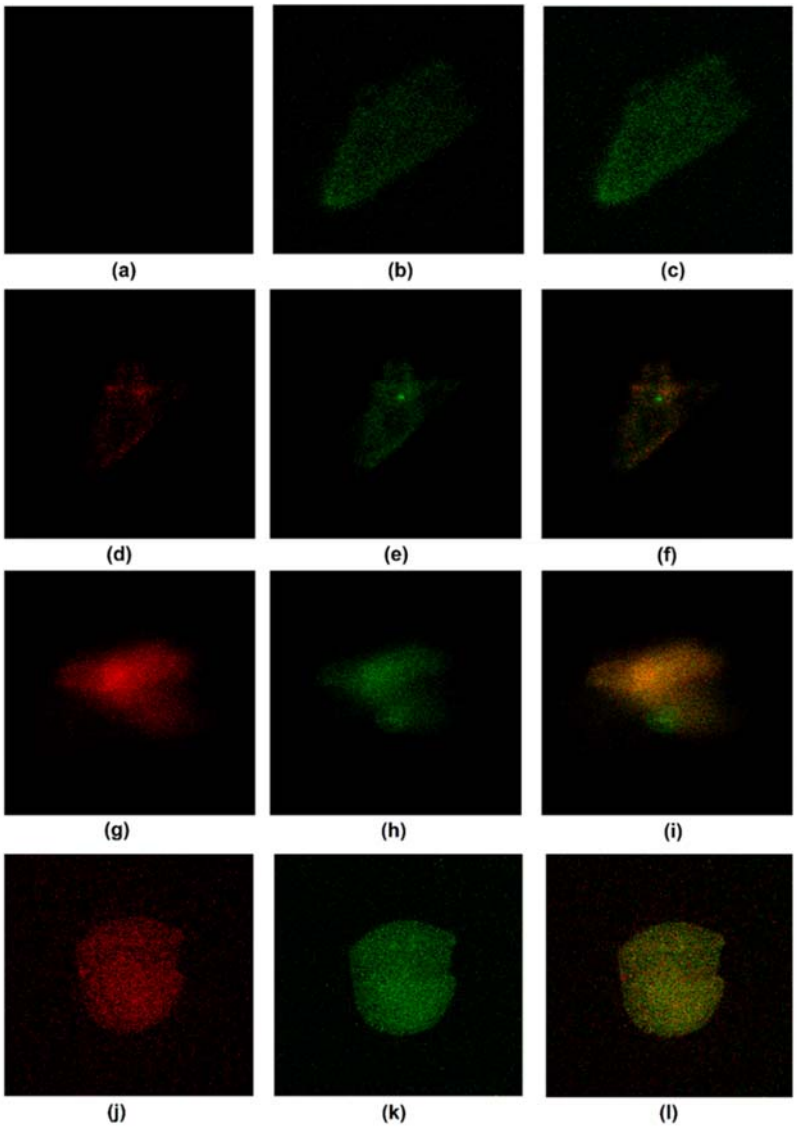

Figure 2-17: Confocal microscopic images showing antibody-antigen complex formation (a-c) zero IgG antigen concentration with only antibody visible (green), (d-f) 3µg/ml IgG antigen (red) and IgG antibody (green), complex (orange), (g-i) 6µg/ml IgG antigen (red), antibody (green), complex (orange), (j-l) NF-κB 400ng/ml antigen (red), NF-κB antibody (green), complex (orange)

The color intensity for higher antigen concentrations is higher and the overlapping orange color intensities also increase in this case representing successful complex formation. Also, there is no fluorescence observable at surrounding areas of the immobilized antibody-antigen complex confirming the selective binding and specificity of the sensors.

3 Sensor Fabrication

This research work focuses on the fabrication of electronic sensing devices through all printed techniques. This approach has many advantages over the conventional lithographic techniques like low research and development cost and simpler process. Printing techniques allowed us to fabricate many different devices with design modifications for optimization of the structures and parameters. As it is an additive manufacturing approach, the material usage is also minimal and any kind of multi-layered complex device structure can be fabricated with ease. The production time for the development and optimization is also very little as changes in design can be made pretty seamlessly and quickly. The major drawback of printing approaches, however, is that they still lack behind in accuracy and performance when compared to the clean room based MEMS fabrication methods. Also, printing technologies are still a bit lagging in terms of mass production of the devices when compared to the conventional methods. Despite that, printing fabrication methods are more favorable when it comes to design and optimization for research and development purpose. After the optimized parameters, structures, and materials are found, we can shift to conventional approaches for better performance accuracy for mass production.

There are two major portions in an electronic sensing device, one is the transducer part that comprises of conductive electrodes and the other one is the active sensing portion to detect the target analyte and generate a signal that can be converted to electrical signal through the transducer. In this research work, different pattern printing methods have been used according to the requirement for the fabrication of transducer electrodes and thin film deposition techniques have been used for the fabrication of active layer fabrication. A usual complete device fabrication process for bi-layered devices with different active layer material categories used in this research work is presented in ***Figure 3-1*** [82].

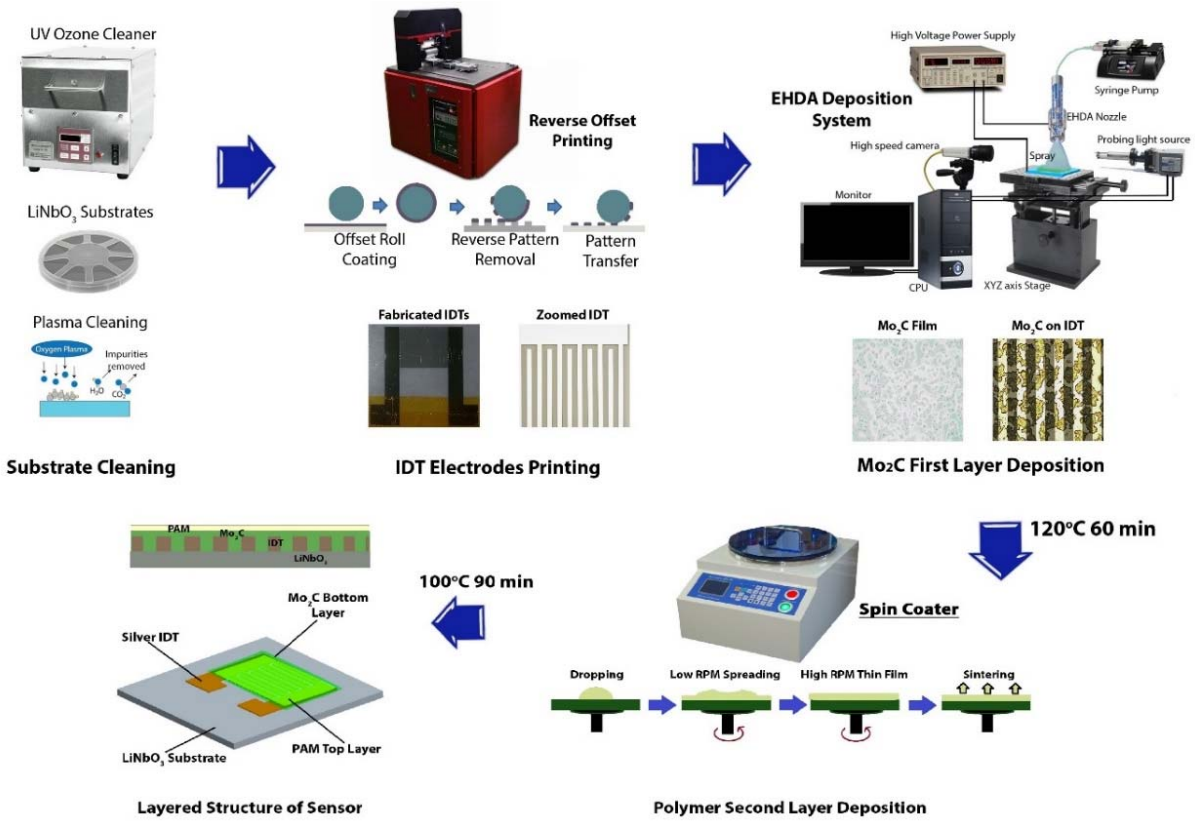

Figure 3-1: Step by step details of printed fabrication process for a general bi-layered sensing devices.

128º Y-cut $LiNbO_3$ substrates were first cleaned through plasma treatment. Reverse offset printing was used to fabricate silver electrodes on the substrate. The electrodes were of interdigital type structure with 40 pairs of fingers, each finger with a width of 50 µm. Electrohydrodynamic atomization (EHDA) was used to deposit the active layer of Mo_2C ink that is a suspension prepared in a conductive solvent while spin coating was used for the deposition of insulating polymer based thin films [82].

3.1 Electrode Fabrication

Electrode fabrication requires the printing system to print patterns in any shape and of any size with high accuracy and repeatability. The electrodes need to have high electrical conductivity and smooth finishing. Three major printing techniques were used to print the transducer electrodes for our sensing devices.

3.1.1 Reverse offset printing

Highly accurate and conductive electrodes were fabricated through reverse offset printing. Silver conductive ink was used by Silverjet DGH ink for reverse offset (viscosity: 1.5cps, surface tension: 24.4mN/m, dispersion matrix: octane

based). Reverse offset printing works on the principle of transferring a fixed design pattern from the host substrate to the target substrate through a PDMS blanket roll. Multiple design of interdigitated transducer (IDT) electrodes were prepared and the cliché was fabricated for each design [12]. The process details and working principle of the printing system are explained in ***Figure 3-2***. The fabricated electrodes by reverse offset printing were cured at 200ºC for 2 hours for all devices.

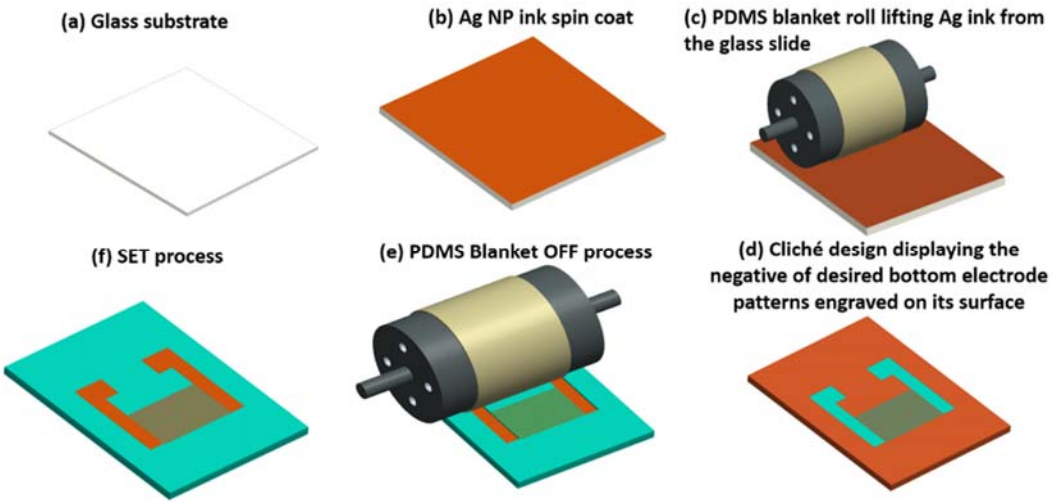

Figure 3-2: Step by step fabrication process of reverse offset printing for electrode fabrication.

The advantages of using reverse offset printing method is that this system is mass production compatible and if the process parameters are optimized carefully, it is capable of printing very high quality patterns that can compete with the conventional lithographic techniques. Pattern sizes of up to 20 µm were printed successfully with very high quality finish. The system was mostly used to print the bottom transducers for the sensing devices and then the top sensing layer was deposited onto them through other printing methods.

3.1.2 Screen printing

Screen printing is one of the most common and simple printing techniques around. The method is used to print patterns and even films onto the target substrate. Screen printing was used to fabricate electrodes on onion membrane in this research work. Other pattern printing techniques like DOD and reverse offset could not be used in this case due to certain limitations. The high pressure in case of reverse offset printing damages the membrane while the un-even surface of the membrane make it difficult to print electrodes on it through electrostatic disposition techniques. The detailed fabrication process of single cell thick onion membrane has been presented in ***Figure 3-3*** [125].

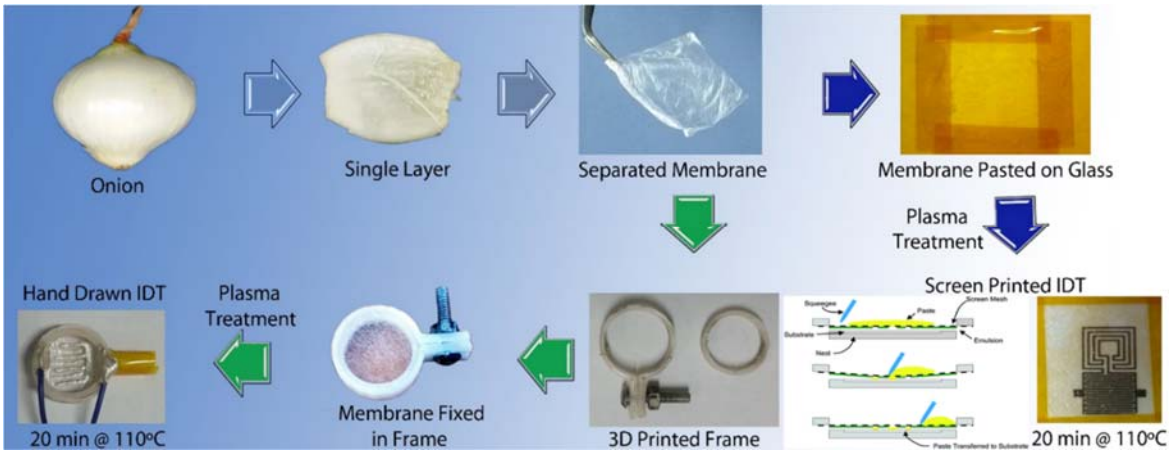

Figure 3-3: Step by step fabrication process of onion membrane based humidity sensor fabrication with screen printed and drawn transducer electrodes.

Screen printing has certain advantages that it can print on rough surfaces easily like in our case of onion membrane. It also exerts low pressure on the target substrate and does not damage it. But, there are also some limitations of this system like it is not capable to print very fine patterns like the other techniques. The printing resolution is quite low while the print quality is not very fine. The printed electrode thickness is also high that is not desirable in case of very thin film based sensing devices. It worked in our case as no top sensing layer was to be deposited onto the onion membrane.

3.1.3 Drop on demand patterning

Micro conductive patterns of any design and shape can be printed using Electrohydrodynamic (EHD) drop on demand (DOD) printing technique. The detailed system schematic and working principle are presented in ***Figure 3-4***.

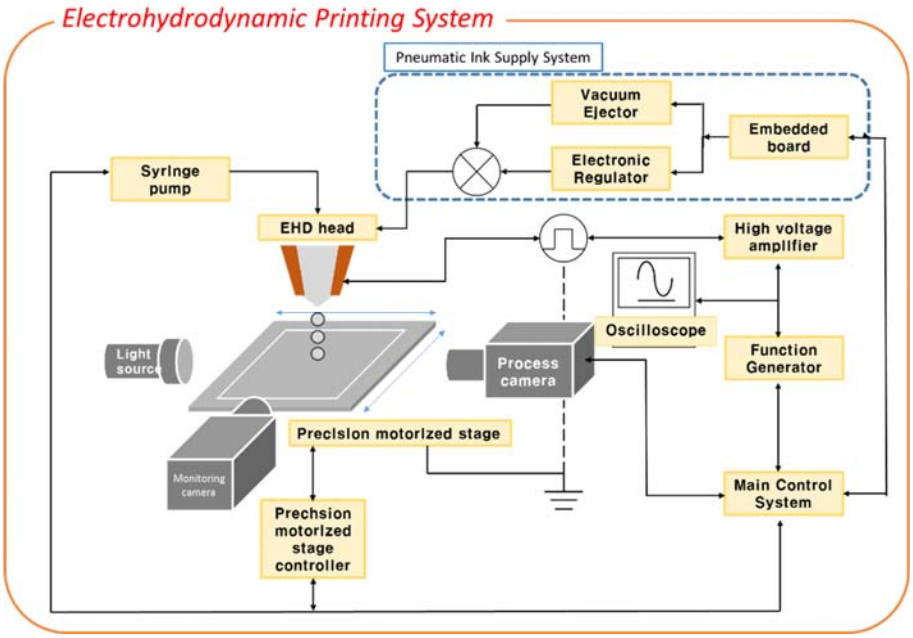

Figure 3-4: Detailed schematic of the drop-on-demand Electrohydrodynamic micro printing system.

There are many advantages of using this system for transducer electrode printing as this system can be used to print micro patterns up to 5 µm on any kind of flat and smooth surface. The system is capable of printing any shape of patterns and is ideal for printing top electrodes for the multi-layered devices with low surface roughness. The system can also be used to repair already printed MEMS based devices with high precision and accuracy. The major disadvantages associated with this system are its vulnerability to accumulated electrostatic charges on the target substrate surface and its inability to print onto the surfaces with comparatively high surface roughness. The system was used to print transducer electrodes for our FET based sensing device.

3.2 Active Layer Deposition

The second major portion of an electronic sensing device it the active sensing region. In this research work, all types of sensing devices have thin films as the sensing areas fabricated through different materials as per device and application requirements. Different printing systems were used for thin film deposition of different categories of materials.

3.2.1 Electrohydrodynamic atomization (EHDA)

Electrospray deposition (ESD) system works on the atomization of the conductive liquid inks based on high magnitude of electrostatic charges at the tip of the nozzle. A modified and more sophisticated version uses hydrodynamic

pressure in addition to electrostatic charge and is known as Electrohydrodynamic atomization (EHDA) system [126]. The detailed system schematic has been presented in ***Figure 3-5*** [57].

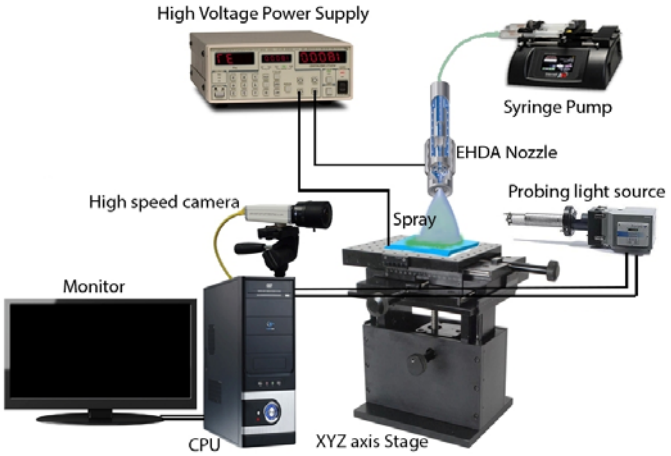

Figure 3-5: System details of electrospray thin film deposition process.

EHDA system can be used to deposit thin films with high quality based on any conductive material or suspension in a conductive solvent. The system was widely used in this research work to deposit active layers of the sensing devices for the compatible materials. The parameters used for the materials deposited through this system are presented in ***Table 3-1*** [13,15,57,82].

Table 3-1: Optimized parameters for thin film deposition of different materials through EHDA.

Parameter	MoS_2	PEO	Mo_2C/Cr_3C_2
Flow Rate	200 µl/hr.	600 µl/hr.	300 µl/hr.
Nozzle to Substrate Distance	15 mm	15 mm	15 mm
Stage Speed	5 mm/s	6 mm/s	5 mm/s
Nozzle Diameter	210 µm	120 µm	210 µm
Number of Passes	5	3	5
Voltage Range for Stable Jet	5.4-6.1 kV	6.6 kV	5.9-6.8 kV
Syringe Internal Diameter	12 mm	8 mm	12 mm

EHDA system is ideal to deposit very fine and accurate repeatable thin films for multi-layered devices but the major limitation is that the target material or ink much have a certain level of conductivity. Insulator materials cannot be deposited through EHDA and other methods have to be used for them. Also, the droplet size in the EHDA process is larger that results in higher film roughness and higher minimum possible thickness for complete covering of the area.

3.2.2 SAW-EHDA hybrid deposition system

Surface acoustic wave Electrohydrodynamic atomization (SAW-EHDA) system is a hybrid thin film deposition system based on the combination of SAW and EHDA systems. It combines the advantages of both and removes the non-overlapping limitations. The particle size achieved through this system is 10 times smaller as in case of EHDA system and thus, lower surface roughness with smaller film thickness can be achieved through this system. It also solves the continuous materials supply issues related to the SAW based deposition systems and lowers the conductivity requirements too. PEDOT:PSS thin film was deposited through this system for our device fabrication. The system schematic and optimized set of parameters for the selected material are presented in ***Figure 3-6*** [3].

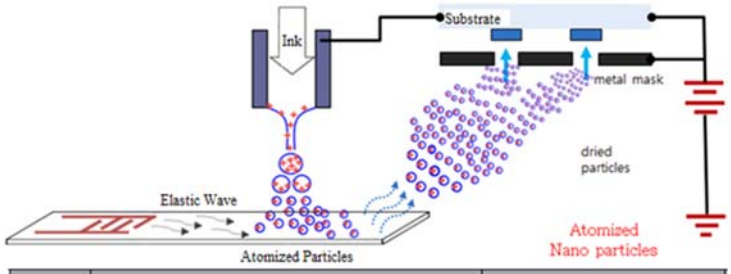

	Parameters	PEDOT:PSS
1	Nozzle diameter	210 μm
2	Flow rate	700 μl/h
3	Mask diameter	3 mm
4	Nozzle to IDT distance	5 mm
5	IDT to mask distance	35 mm
6	Mask to substrate distance	10 mm
7	Nozzle (−ve)—applied voltage	−4.539 kV
8	Mask (+ve)—applied voltage	1.50 kV
9	Substrate (+ve)—applied voltage	3.35 kV
10	Applied frequency	19.8 MHz
11	Power	5 W
12	Deposition time	30 min

Figure 3-6: Schematic of SAW-EHDA hybrid thin film deposition system and the optimized set of parameters for the deposition of thin film of PEDOT:PSS.

The ink conductivity requirements for this system are higher when compared to the simple EHDA based system. Also, the limitation lies with the density of the materials used. High density materials and larger chunks cannot be deposited through this system. Another major drawback is that the ink needs to be in solution form rather than as a

suspension to be able to be used for this system. In case of conductive solvent in a suspension of an insulating material, only the solvent will be deposited leaving behind the actual active material. So, the system can be best used to fabricate multi-layered devices without damaging the lower layers for the materials with good conductivity, low density, and available in solution form.

3.2.3 Spin coating

Spin coating technique is the simplest and most common method for thin film fabrication. Any kind of materials in liquid form can be used with this system without the consideration of viscosity, conductivity, particle size, or density. The system process is presented in ***Figure 3-7*** [1,12].

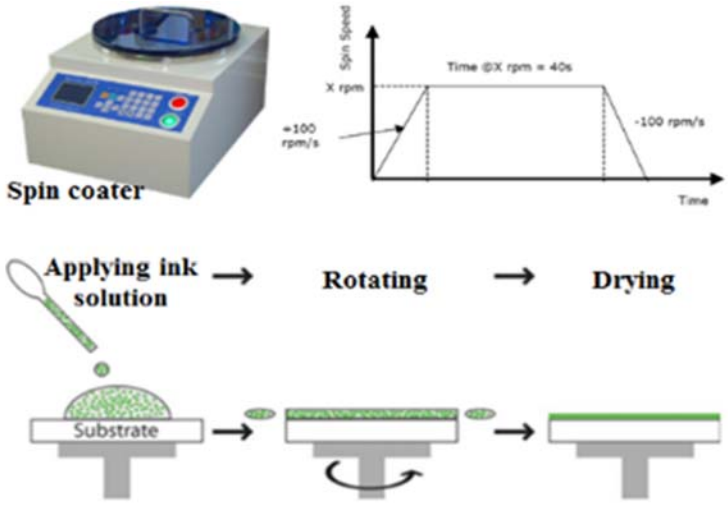

Figure 3-7: Schematic and working principle of spin coating system.

The major limitation of this system is that it is vulnerable to damage the lower layers in case of multi-layer device fabrication. Also, very thin films of suspensions and 2D materials cannot be fabricated through this system as it either throws away the particles due to centrifugal forces or result in agglomeration due to centripetal forces. Spin coating has only been used as a back-up option in this research work for the materials that were not compatible with any of the other available thin film deposition systems.

3.2.4 Microgravure printing

Microgravure printing was used in this work to fabricate large area coatings for the flexible human posture sensors. Carbon/polymer based active material composite was deposited in the form of thin film onto a flexible PET substrate roll. The system images, process schematic, and the images of fabricated devices are presented in ***Figure 3-8*** [100].

PET roll with a thickness of 0.2 mm and a width of 140 mm was used as large scale substrate for sensors. The web tension has a voltage controlled open-loop passive controller with a maximum torque output of 3 Nm at 100% output. The tension controller output was set at 15% and the temperature of the in-situ curing chamber was fixed at 130 ºC.

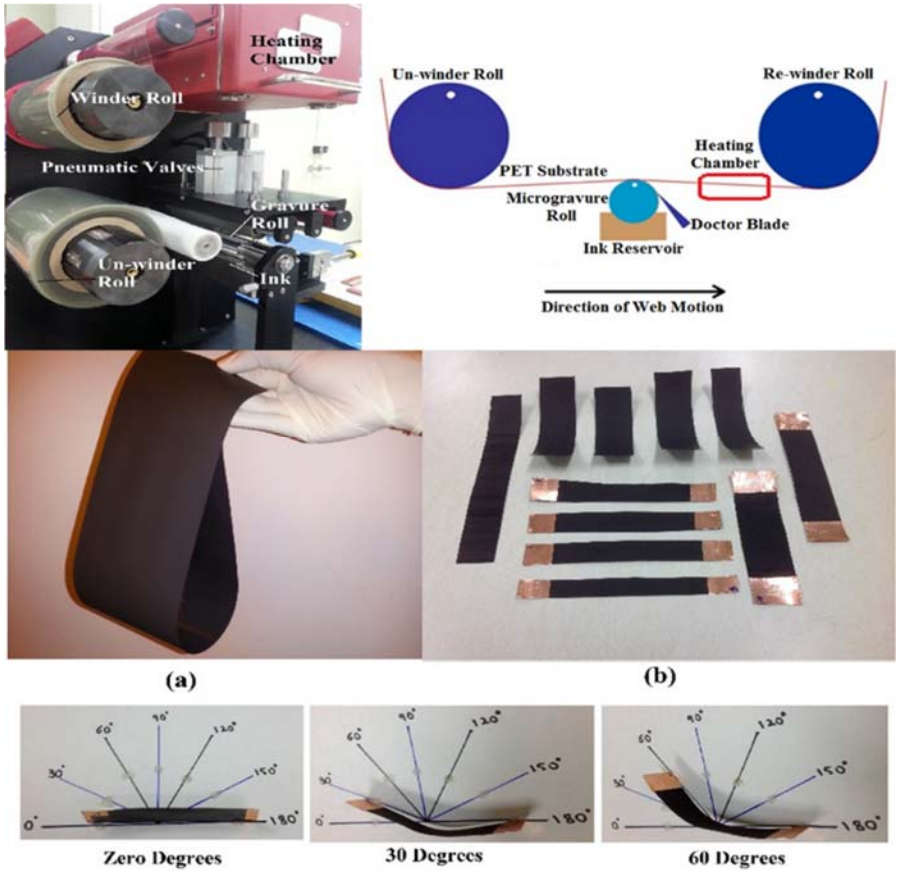

Figure 3-8: Microgravure printing process and the large area thin film coating results of the fabricated posture sensing flexible devices.

For the fabrication of the active layer, the web velocity was fixed at 3mm/s and the gravure roll velocity was kept at 5 mm/s. This implies that the thickness of the coated film will be approximately 1.66 times higher than the minimum achievable thickness for the specific ink as there is a linear relationship between the ratios of gravure roll speed to web speed in range of 100% to 200% [127]. The thickness depends on the ink properties as well as the velocities of the moving web and the gravure roll. If the velocity of the web and the gravure roll are equal, the thickness is the minimum achievable for a uniform and continuous thin film. If the velocity of the gravure roll is higher than that of the web, the thickness will increase as the number of passes will increase. The gravure roll used for the active carbon layer deposition was 150 mm in width with 45º line patterns and coated the whole PET substrate. After the active layer deposition, the sensors were protected with a coating of PVAc deposited through the same fabrication system.

4 Analysis of Sensors

Different types of sensing devices fabricated in this research work were analyzed for their output performance through specifically designed characterization systems. Accurate and reliable analysis of fabricated sensing devices is of crucial importance as it allows us to optimize the performance parameters according to the required specifications and goals.

4.1 Environmental Sensors

Environmental factors like temperature, humidity, light, etc. have to be monitored and controlled for various applications and industry including medical, food, agriculture, and others [128–130]. There is vast research going on in sensor development for accurate monitoring of the environmental parameters. The goal of this research is to develop sensing devices with higher accuracy, robustness, sensitivity, stability, small size, and fast response. Different researches focus on improving one or two of the many parameters in humidity sensors while compromise the remaining ones. That can be useful for a target specific application for example the detectable range is important in long term environmental sensors [1] but the response time and sensitivity are not very crucial; in case of medical applications, the response and recovery times are crucial [3] but the range can be compromised.

4.1.1 Characterization setup

State of the art environmental chamber was constructed for the evaluation of the environmental sensing devices. The setup consists of a sealed environmental chamber with controlled levels of temperature and humidity inside that. The detailed schematic of the characterization setup is presented in ***Figure 4-1***.

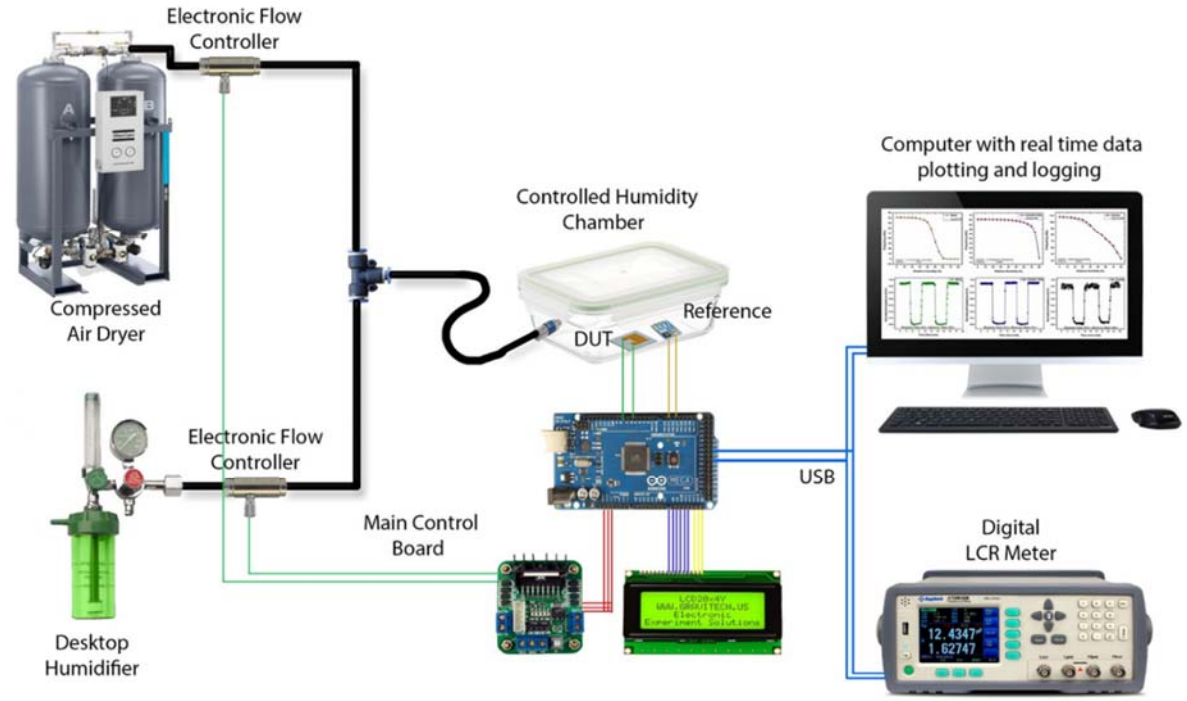

Figure 4-1: Detailed schematic of the environmental sensors characterization setup.

The figure shows the main parts of the system including a desktop humidifier as the source for increasing the humidity levels inside the sealed chamber. The humidifier works on the principle of atomization of water into micro particles that are fed into the chamber through a duct with an electronically flow controlled valve. The dehumidification or desiccation of the chamber is done by purging the chamber with dry air from a dual cylinder compressed air dryer. Both the streams of dry air and humid air from the humidifier are combined at the input duct of the chamber and the level of relative humidity is controlled by controlling their individual flow rate through a feedback based PID control system. The reference values of temperature and humidity inside the test chamber are recorded and used as the feedback also using a commercial high precision humidity sensor (HTU-21D) with a resolution of 0.04%RH and an accuracy of ± 2%RH. The temperature coefficient for the reference sensor is -0.15%RH/ ºC and the response time is <5s. The reference sensor is also used for temperature control of the chamber that is controlled by a hot Peltier plate fixed at the base of the chamber to increase the temperature from room temperature up to 80ºC. For temperature below room level, the position of Peltier cooling plate is reversed. All data logging and sensors interfacing plus the control system implementation of the environmental chamber is done using an Arduino MEGA microcontroller based processing circuit. The electrical characteristics of the fabricated sensing devices are measured and recorded through a desktop LCR meter Applent AT826. Both the LCR meter and the Arduino based

circuit are connected to a host computer for real time data plotting and logging of all the factors. Personalized GUI based software was developed for easy user interface and interaction.

4.1.2 Humidity sensors

The percentage of quantity of water vapors present in the air at a certain temperature that is required for saturation at that particular temperature is known as relative humidity. Relative humidity is a crucial environmental factor in industry, food, and health care applications. There is a lot of research underway on the development of accurate, cheap, and easy to interface sensors for the applications of monitoring and control of environmental humidity [34,128–130]. Most of the current research works on humidity sensors target one or more parameters while compromising the rest that is only acceptable for application specific devices, for example, humidity sensors with fast response and recovery times but non-linear curve shape and limited range of detection serves the purpose for a breath analyzer [3,131], wide range and linear sensors with stable response but long response and recovery times can be used for conventional environmental sensors [38,132,133], highly sensitive sensors with slow response working only in either lower or higher humidity are suitable for food industry [134,135], and so on. Researchers working in different areas of technology use the knowledge and equipment at their disposal to try to improve most of the performance parameters while keeping the cost low and the fabrication easy. To achieve this goal, scientists have used different sensor structures, transduction techniques, and working mechanisms like Interdigitated Transducers [28–30], Surface Acoustic Waves [31–33], Quartz Crystal based Transducer [27], Field Effect Transistors [34–36], and other structures [23,37–39] and techniques [40–43]. Resistive and capacitive type sensors, however, have been the major focus owing to their low cost, simple fabrication, easier deployment in real life applications, and above all, good performance [44–46]. In case of capacitive and resistive type sensors, scientists develop novel materials and their composites to achieve their desired performance parameter. There is a huge number of material categories that have been developed and tested in resistive and capacitive sensors including ceramics, metal oxides, polymers, bio-materials, 2D materials, transition metal dichalcogenides (TMDs), carbon and its derivatives, composites, supra molecules, block copolymers, and so on [21–27,136–144]. Among different materials used, hydrophilic polymers have always been one of the preferred choices for humidity sensing devices owing to their high affinity towards water molecules resulting in higher sensitivity and wide detection range. Some of such previously reported polymers include composites of PVA [1,145–147], polyacrylic acid [12], PEDOT:PVMA composite [41], Polyaniline [148,149], PoPD [150], PVP [151], poly diethynylbenzene [152], and so on. The major focus

in most of the research in material based humidity sensors had been on the development of either a single material or a composite to achieve the targeted performance but they have mostly used single layers of the developed material as the sensing layers and have ignored the importance of device structure and configuration [139,141,153]. This no doubt leads to improvement in the targeted parameter but effects the other interlinked ones like curve linearity, user friendly readout signal, response time, etc. Other researchers have tried to change the configuration and structure by using bi-layered sensing films and even successfully improved certain parameters, yet, compromising the response time, detection range, and linearity [38,154–157].

1) The focus of this research is to keep in view both the material aspect and the importance of device configuration and then employ it to fabricate sensors without compromising any major performance parameter. The device structures and materials were optimized step by step after going through many designs and material categories to achieve the results of an ideal sensing device that can be used for any kind of application. The research on humidity sensors started with a single layered device with an FET type transducer structure with Nickle Phthalocyanine (NiPc) as the sensing material. The device structure along with the main results and the summary of the major performance parameters is presented in ***Figure 4-2***.

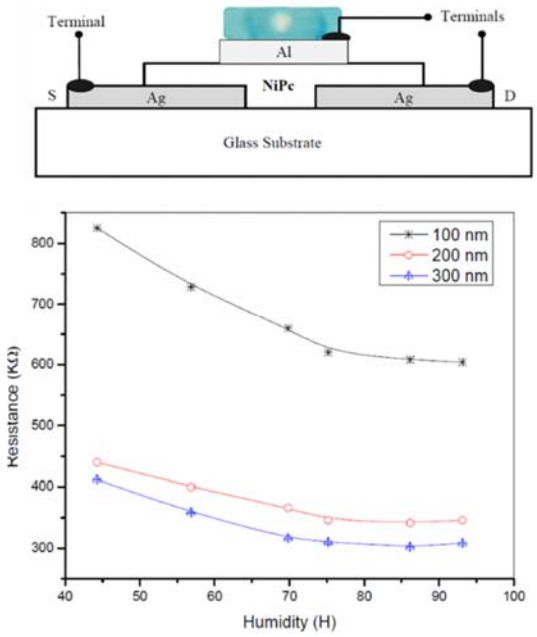

Parameter	Comment
Sensitivity	Low
Range	Poor
Transient Response	Slow
Stability & Accuracy	Low
Robustness	OK
Linearity	Poor
Temperature Dependence	High
Selectivity	Not Found
Low %RH Detection	Poor

Figure 4-2: Device structure of the FET type humidity sensor with resistive response curves and the performance parameter summary.

The summary shows the device to be capable of sensing humidity in range of 45% RH to 95% RH but the overall performance of the device is poor. It can only be used in target specific applications and cannot be used in general

environmental monitoring.

2) In the second device, the structure was changed to an IDE based transducer with large surface area but the sensing portion was comprised of a single layer of a conductive polymer PEDOT:PSS. The thin film deposited through SAW-EHDA had high surface area to volume ratio with thickness less than 100 nm. The sensors work on the principle of change in resistance for changing level of relative humidity. As PEDOT:PSS is a conductive polymer, the increase in amount of adsorbed water vapors results in the increase in ionic and electronic current through the thin film thus dropping the device resistance. As the sensors have very thin sensing film, the change in capacitance is minimal and the sensors cannot be used as capacitive or impedance based device for read-out. The results presented in ***Figure 4-3*** show that the sensor had a very fast transient response near 150 ms with a reasonable range of detection (RoD) from 0% RH to 90% RH but a comparatively low sensitivity and low humidity detection. The output response curve shape of the sensors is also non-linear that results in difficulties to design an accurate read-out interface circuit.

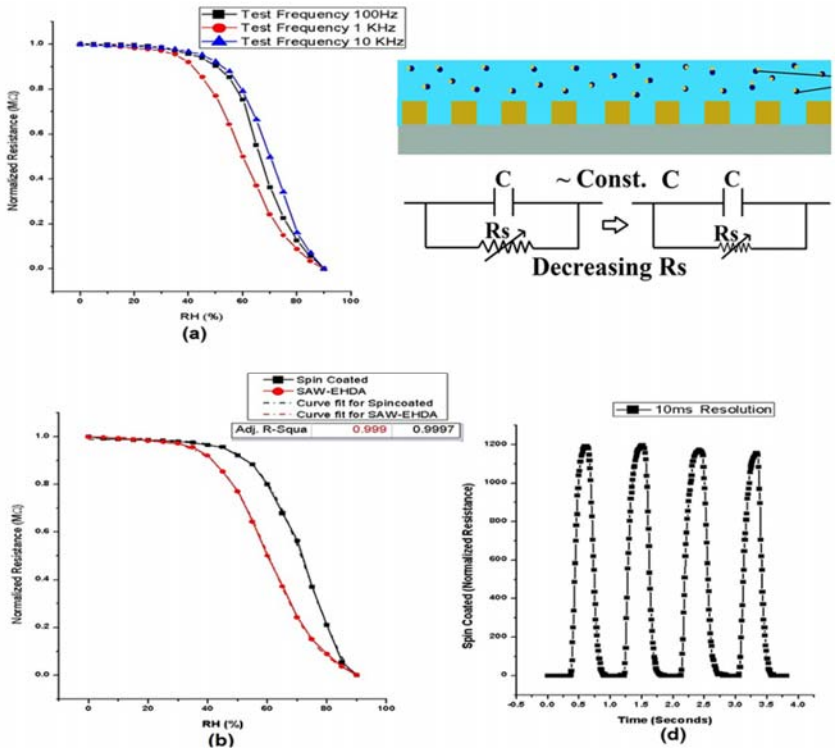

Figure 4-3: Resistive response of the PEDOT:PSS based single layered humidity sensor along with transient response and sensing mechanism and structure.

3) The third device was based on the same structure but the active layer materials was changed to a composite of conductive and insulating polymers of PEDOT:PSS and PVA respectively. PVA is a hydrophilic polymer with good affinity towards water molecules and can uptake reasonable quantity of water resulting in higher sensitivity. The

reason for using a combination of these polymers was aimed to improve the sensitivity and sensing range and improve the robustness. The results and structure of the device are presented in ***Figure 4-4*** which shows that the sensitivity has been considerably improved but the response time has been very slightly compromised by a fraction of a second with an increase in hysteresis and decrease in RoD. The problems of low RH sensitivity and the response curve non-linearity persist with this device too.

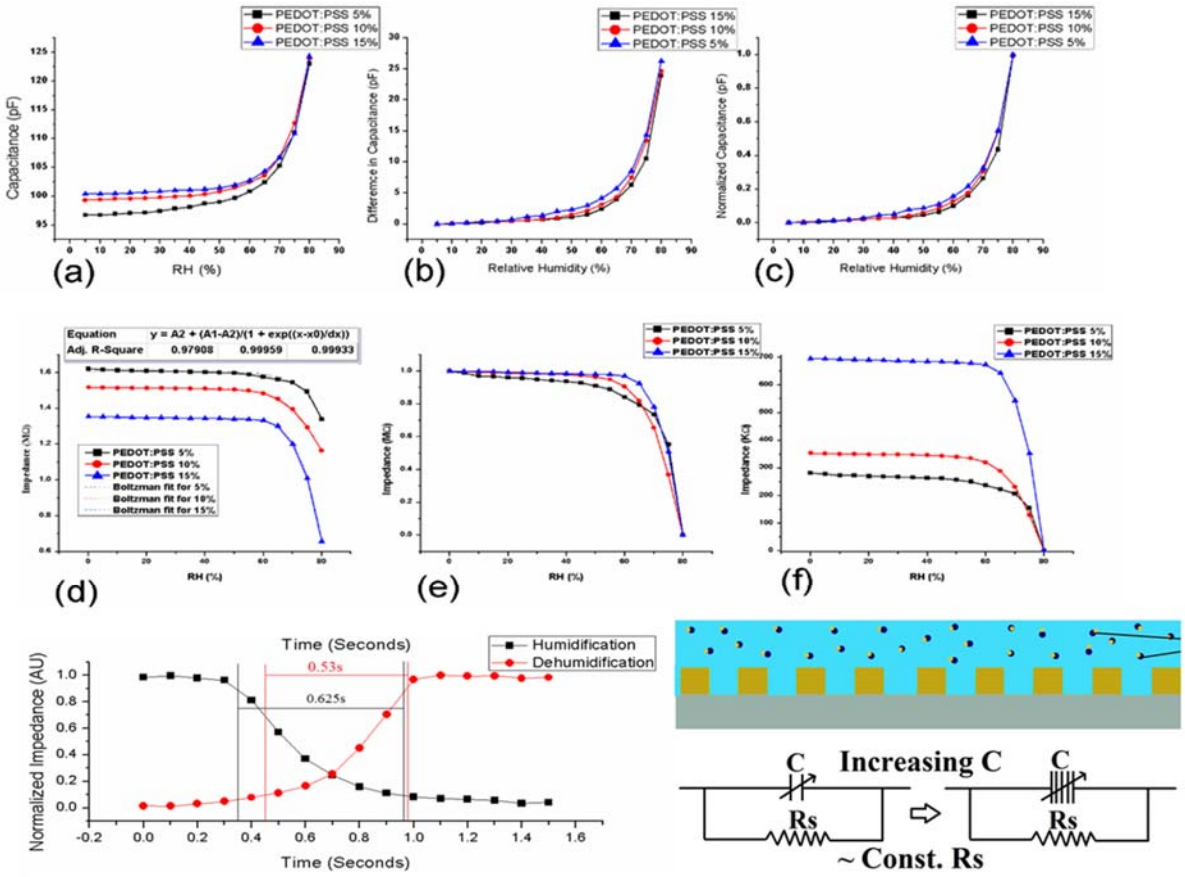

Figure 4-4: Results of the humidity sensor based on PVA+PEDOT:PSS composite sensing layer and the device structure and sensing mechanism.

4) The first three experiments show that there is a requirement of a material or a composite with very high sensitivity that can be achieved with a super-hydrophilic polymer that has a very high affinity towards water. A composite of poly acrylic acid partial sodium salt powder dispersed in BEHP-co-MEH:PPV polymer solution with chloroform as the solvent was used to fabricate the active layer of the next sensor. The reason of using non-aqueous solvent and polymer binder solution was to keep the PAAPSS particles dispersed without letting them swell from absorption of water from the solvent. The results of the device along with the structure and summary are presented in ***Figure 4-5***. The results show that the sensitivity of the device was highly increased and the sensors could be used for a wide

range but the relative sensitivity for low RH levels was still not good. The sensors work on the principle of increase in capacitance with increase in the dielectric constant of the thin film upon water absorption. The transient response was also slower (in range of 5-6 s) as the drying of PAAPSS took longer time. The sensors still had a poor linearity and the temperature dependence was medium that is not appreciable.

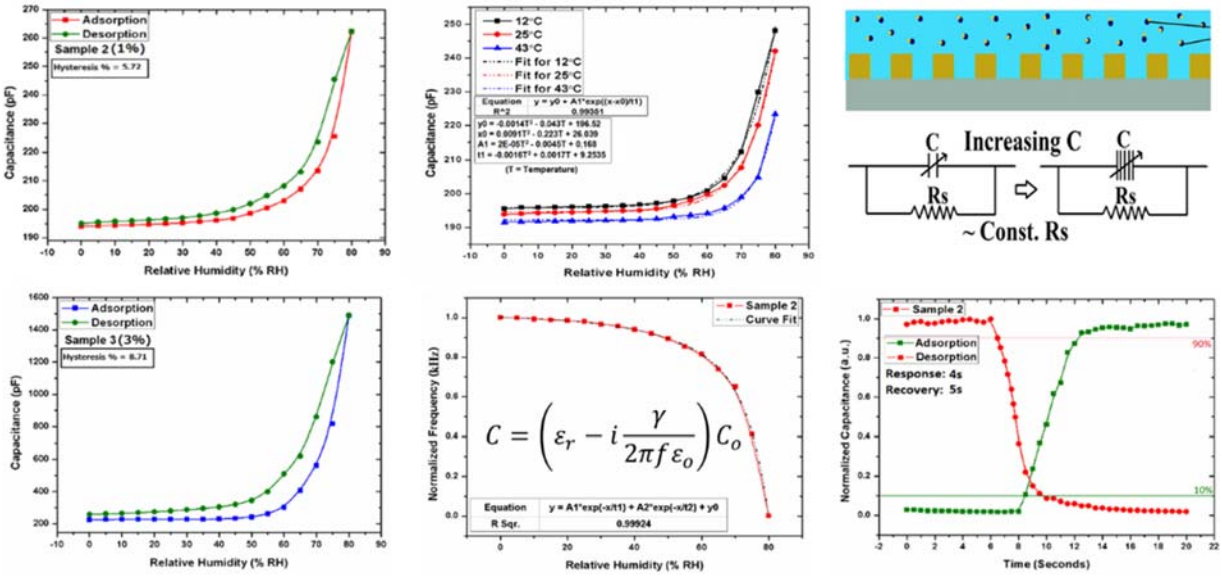

Figure 4-5: Capacitive response of the BEHP-co-MEH:PPV+PAAPSS based humidity sensor with its device structure and working principle.

A detailed comparison table of the single layered humidity sensors performance parameters is presented below in **Table *4-1***.

Table 4-1: Comparison of performance parameters of single layered humidity sensors.

Parameter	NiPc FET	PEDOT:PSS	PVA+PEDOT:PSS	Onion Membrane	Super-hydrophilic	Modified PEO
Sensitivity	Low	Low	Low	Low	High	High
Range	Poor	Wide	Good	Good	Good	Wide
Transient Response	Slow	Fast	Fast	Medium	Medium	Medium
Stability & Accuracy	Low	Low	Low	High	High	High
Robustness	OK	Low	High	High	High	High
Linearity	Poor	Poor	Poor	Poor	Poor	High
Temperature Dependence	High	High	High	Medium	Medium	High
Selectivity	Not Found	Not Found	Not Found	Not Found	Not Found	Not Found
Low %RH Detection	Poor	Poor	Poor	Poor	Poor	Good

5) To solve the problem of response curve linearity, the device structure was re-designed from a conventional single

layered active area on IDT to a bi-layered device. The electrical and mathematical model of the device was studied and materials with suitable humidity sensing properties were selected for the two layers. A unique combination of 2D flakes of transition metal carbides (Mo_2C and Cr_3C_2) along with a medium range hydrophilic polymer polyacrylamide (PAM) were used to fabricate the two layers. The effect of layer thickness on the linearity was also studies along with the individual sensing behaviors of the materials and their composites. The results of the individual single layered sensors based on the 2D materials and the polymer are presented in ***Figure 4-6***. The first thing that can be noted directly by looking at the curves is that the overall impedance of all the devices decrease non-linearly with increasing levels of relative humidity in the environment. When assessed separately, some useful information about the working principle and the magnitude of change in impedance can be extracted from the results. We can see that the impedance of the Mo_2C/Cr_3C_2 based sensor shows a change of ~7 kΩ for the first half of relative humidity and ~33 kΩ for the second half. The impedance for PAM based sensor shows a change of ~35 kΩ for the first half and ~200 kΩ for the second half.

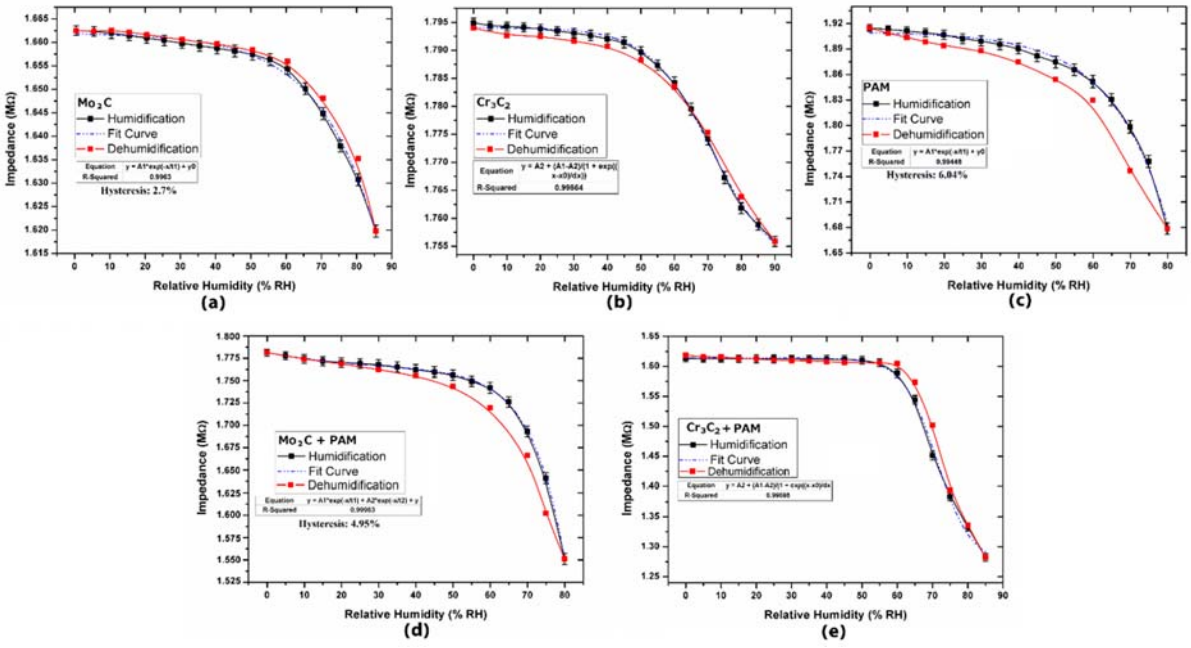

Figure 4-6: Impedance response of single layered sensors with active layers of (a) Mo_2C, (b) Cr_3C_2, (c) PAM, (d) Mo_2C + PVA, and (e) Cr_3C_2 + PAM.

The structure of PAM has repeating cross-linked chains containing amide groups. The amide groups, made up of a Nitrogen atom bonded to two Hydrogen atoms, have Hydrogen bonding forces which strongly attract water. Water diffuses into the polymer network and is held within by strong attraction to the amide groups but can be removed upon drying of the sample. At higher levels, the water molecules are freely held inside resulting in much larger

changes in dielectric constant of the films. The sensors with composite based active layers show similar behavior as there is no direct interaction between the Mo_2C/Cr_3C_2 particles and the polymer matrix. Both materials independently contribute in the humidity sensing resulting in similar response curve shapes. In case of polymers, the sensing principle can be described in terms of change in capacitance resulting from the adsorbed water molecules in the film. The capacitance increases with increasing humidity and the impedance decreases according to equation 1. For the Mo_2C/Cr_3C_2 based sensor, the series resistance of the device decreases with increasing humidity due to the flow of ionic current through the exfoliated flakes. This in return results in decrease in impedance according to equation 1.

$$Z = {}^{1}/_{2\pi fC} + R_s \quad (1)$$

Here, "Z" is the impedance, "f" is the test frequency, and "C" is the capacitance. Based on the different sensing principles and the magnitude of change in impedance in different regions for the Mo_2C/Cr_3C_2 based films and polymer based films, a new bi-layered structure was proposed for the sensing area. The aim of this scheme was to reduce the non-linearity in the response curves. As we can see that the change in impedance in the first half of PAM based sensors (~35 kΩ) is comparable to the change for the second half for Mo_2C/Cr_3C_2 based sensors (~33 kΩ). If we can limit the PAM based film to sense humidity based on change in capacitance for the first half and then use the Mo_2C/Cr_3C_2 based film for the second half, we can achieve a nearly linear response curve. That was the reason behind choosing PAM as the top layer and Mo_2C/Cr_3C_2 as the bottom layer. The equivalent circuit of the bi-layered sensor is presented in ***Figure 4-8***. The PAM top layer plays the major role in humidity sensing for low humidity levels based on the change in capacitance while very few water molecules can reach the bottom layer of Mo_2C/Cr_3C_2 to contribute in ionic current resulting in resistance change. This means that the resistance of the sensors remain almost constant for the first half while capacitance increases. For the second half, the top PAM layer is almost full with absorbed water molecules and the surplus molecules escape to the bottom layer of Mo_2C/Cr_3C_2 resulting in the change in resistance. This results in an almost linear response of the sensors for the bi-layered active area. The terms C_{eq} and R_{eq} represent the effective capacitance of the two films dominated by PAM and the effective resistance dominated by Mo_2C/Cr_3C_2 film respectively. The terms R_i and C_1 collectively represent the interface impedance of the two films. A physical interface between the two films acts as a barrier for the low energy-low concentration molecules, ions, and electrons to travel to the bottom layer at low relative humidity. When the humidity levels increase significantly, the barrier

allows the flow between the two films that results in impedance drop. In case of IDT based sensors, the major role in sensing is played by C_{eq} and R_{eq} and the simplest equivalent circuit of the bi-layered sensor can be described as a parallel RC circuit [158]. The results of the bi-layered sensors for average of three trials are presented in ***Figure 4-7*** along with the comparison of the response curve shapes of all fabricated sensors.

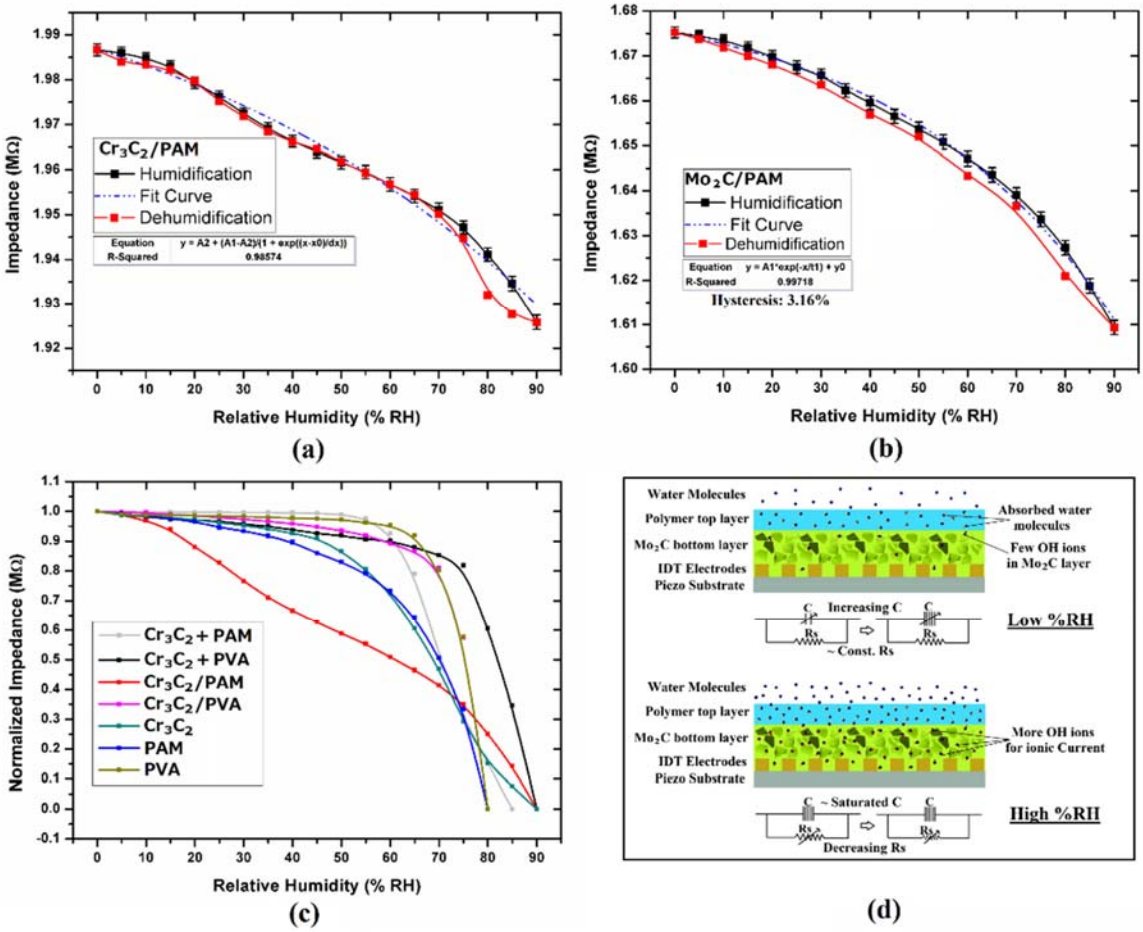

Figure 4-7: Impedance response of bi-layered sensors with active layers of (a) Cr_3C_2/PAM, (b) Mo_2C/PAM, (c) comparison of normalized response curve shape of all sensors, and (d) sensing mechanism and working principle of bi-layered device.

The results show that an almost linear response has been achieved for the PAM/Cr_3C_2 and PAM/Mo_2C based sensors as expected. The overall impedance of the bi-layered device changes from 1986 kΩ at 0% RH to 1926 kΩ at 90% RH. This means that the net change in impedance for the full range is 60 kΩ which shows an absolute change of 660 Ω/%RH. The comparison of response curve shapes of all sensors clearly shows the improvement achieved in case of bi-layered sensor. To optimize the parameters and to make the response curve shape closer to linearity, four different samples with varying combinations of PAM and Cr_3C_2 film thicknesses were fabricated. The effect of film thickness on the device performance along with the stability data of the device recorded over a time period of 40 days are

presented in ***Figure 4-8***.

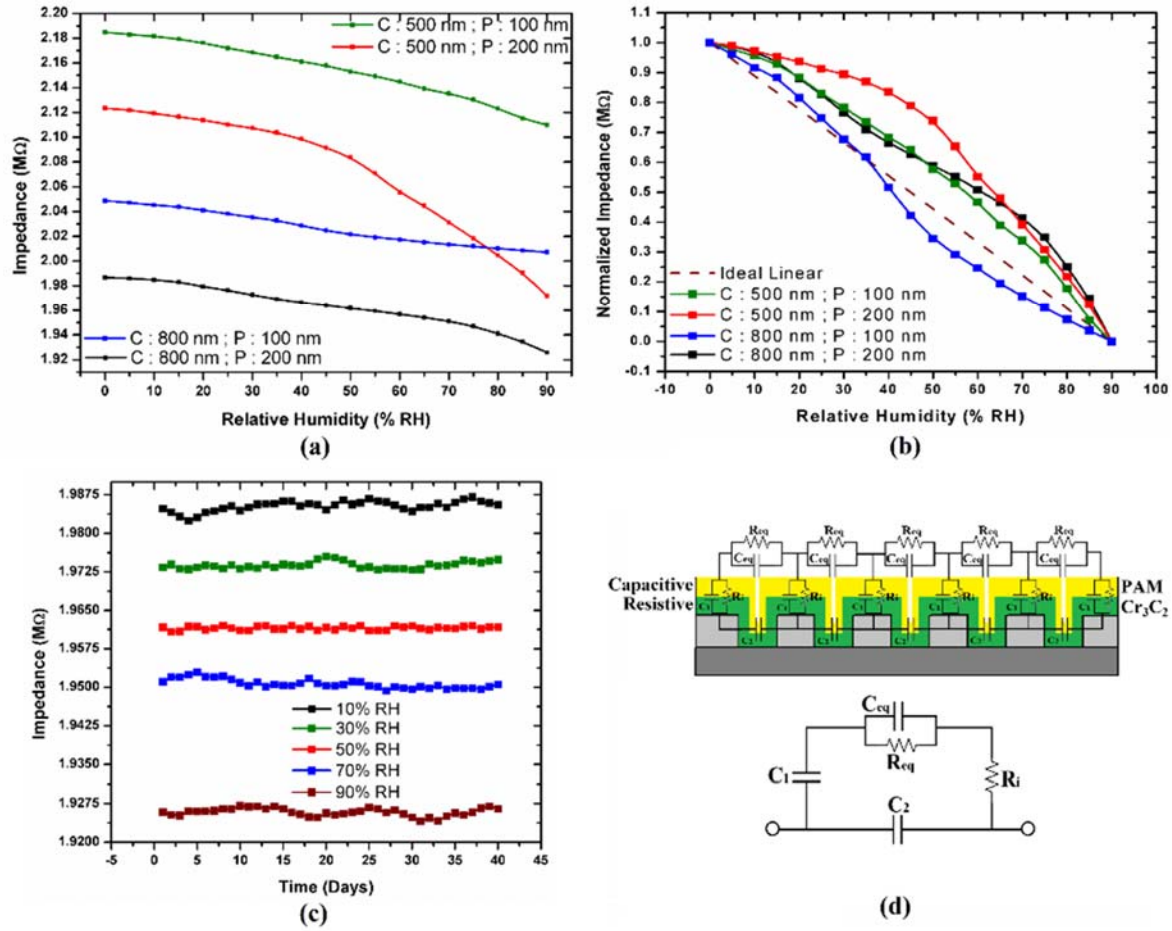

Figure 4-8: Effect of film thickness on the performance of sensors with (a) showing actual impedance values of all sensors, (b) showing normalized curves for linearity comparison, (c) showing stability data of the sensors over 40 days, and (d) equivalent circuit of the bi-layered sensor on IDT electrodes.

The thickness dependent results show that the intrinsic impedance of the sensors increase with decreasing film thickness as expected. Both materials have almost same effect on the overall impedance of the sensors. The plots indicate that the curve shape can be tuned towards maximum linearity by controlling the film thickness of both materials. Selecting the ideal combination requires further experimentation but a trend can be predicted based on the current results. The trend shows that reducing the thickness of PAM thin film while increasing the thickness of Cr_3C_2 film tends to shift the output towards linearity. The predicted combination is expected to lie between 100-150 nm film of PAM and 600-700 nm film of Cr_3C_2. The stability of the sensors was tested by recording their impedance at 5 different humidity levels for 40 consecutive days. The sensors were left at room conditions after recording the data until next day. The stability curves show good stability of the sensors in open environment with negligible error in the medium range while small deviations at minimum and maximum relative humidity levels. The output of the

sensors was converted to frequency using an oscillator based circuit details of which are presented in ***Figure 4-9*** along with the results of the frequency output of the composite based and bi-layered sensors. It can be observed that the response curve shapes for frequency output are similar to those of impedance output of the respective sensors. The only difference is in the curve shape of the Cr_3C_2/PAM and Mo_2C/PAM bi-layered sensors showing a perfect linear output after multiple number of trials. The reason for this change was investigated using the formulae of frequency output of the circuit and the effective capacitance. For capacitors showing a leakage current through the electrodes, the system involves other circuit elements also in addition to capacitance and the effective capacitance of the whole system can be represented using equation 2 [159].

$$C = \varepsilon^* C_o = \left(\varepsilon_r - i\frac{\gamma}{2\pi f \varepsilon_o}\right) C_o \quad (2)$$

Where C_o is the actual capacitance, γ is the conductance, and f is the frequency. In the bi-layered sensor case, there is a big role of the leakage current through the device as the bottom layer is working on the principle of resistance change.

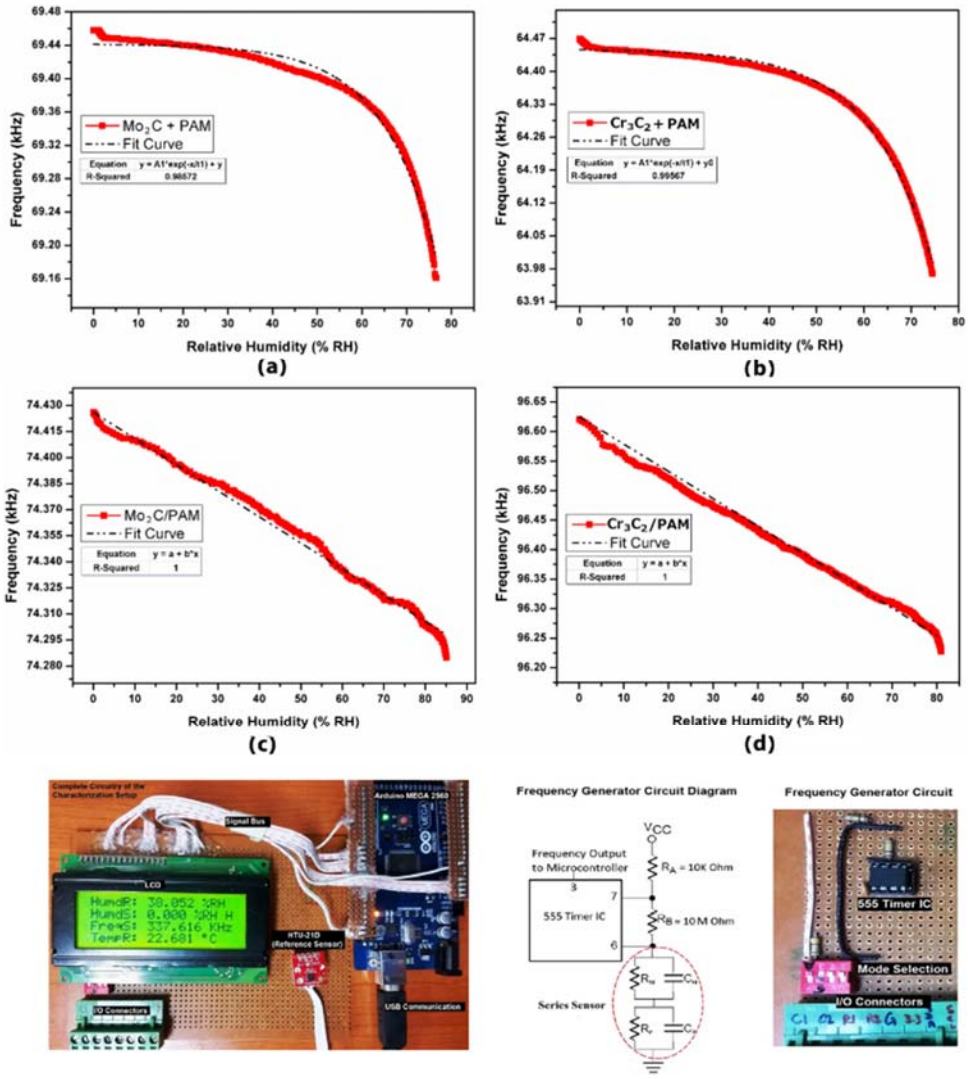

Figure 4-9: Frequency output response of composite based and bi-layered sensors with active layers of (a) Mo_2C + PAM, (b) Cr_3C_2 + PAM, (c) Mo_2C/PAM, (d) Cr_3C_2/PAM, and (e) frequency readout circuit design and equivalent circuit of the sensor.

This means that the effective capacitance of the system changes with some non-linear factors unlike the impedance. The sensor is considered as a capacitor in the oscillator circuit to convert its response to frequency. The formula for the output frequency of the oscillator circuit is given in equation 3 [125].

$$f = \frac{1.49}{(R_A+2R_B)C} \quad (3)$$

R_A and R_B are two fixed resistances in the circuit and C represents the capacitance of the sensor as presented in equation 2. Even if we do not consider the overall effective capacitance of the sensor but rather consider the sensor as an equivalent circuit with series parallel combinations of capacitor and resistors, the effective values of R_A and R_B are also changed along with the value of capacitance. This involves an additional nonlinear factor in frequency output

equation that is possibly cancelling out the negative nonlinearity in the frequency response. The sensors show an absolute change of 4.81 Hz/%RH for the frequency response between 0%RH to 80% RH. The linear output is ideal for commercial and accurate humidity sensors fabrication with good responsivity and wide range. The sensors were finally tested for their response and recovery times (10% to 90% of maximum value). A breath detection system [1] was used for this purpose and the results for composite based and bi-layered sensors are presented in ***Figure 4-10***. The scale on x-axis is in seconds showing fast response and recovery times for all the four types. For the bi-layered sensor of our interest, the response time was measured to be 1 s while the recovery time was ~1.6 s. These values show excellent response of the sensors towards quickly changing humidity levels. The use of piezoelectric substrate helps to produce surface acoustic waves that can reduce the recovery time of the sensor by energizing the adsorbed molecules [1]. These values obtained for the fabricated sensors clearly out-perform most of the high end commercial sensors and shows the potential of these devices to replace the existing technology.

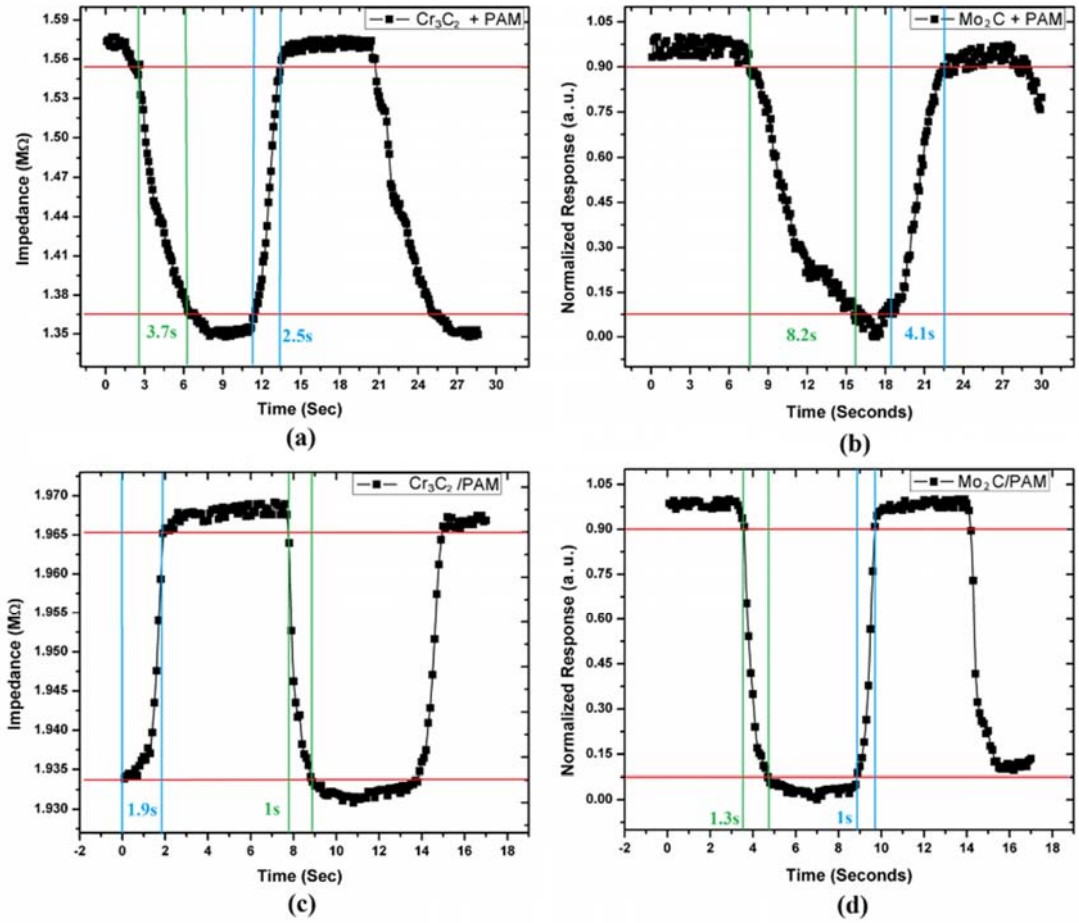

Figure 4-10: Response and recovery time measurement of sensors with active layers of (a) Cr_3C_2 + PAM, (b) Mo_2C + PAM (c) Cr_3C_2/PAM, and (d) Mo_2C/PAM.

6) The bi-layered sensors showed excellent linearity but with a compromise on the sensitivity of the device. Further research was done in materials perspective to improve the sensitivity while keeping the linearity intact. For this purpose, thin films of pure PEO with high molecular weight as the humidity sensing active layers for impedance based humidity sensors fabrication. Polyethylene oxide (PEO) is a polymer hydrogel possessing ionic conductivity that varies with different percentage of absorbed water molecules and ions. This property makes it a good candidate to be used in humidity sensors' active layers. The degree of crystallinity of PEO thin films decrease with increasing humidity that facilitates the ion conduction in the thin films, thus reducing the film impedance. The thin films of PEO in their semi-crystalline solid form were tested for their impedance response towards humidity. A different set of samples were heated beyond the melting point of the polymer converting the thin films to amorphous phase and the film morphology to waxy solid state. Ionic conduction was enhanced in the amorphous films due to their high affinity towards even low concentrations of water vapors resulting in highly sensitive and stable linear relative humidity sensors. The two types of sensors were tested for their impedance response towards change in relative humidity. A total of 12 samples were prepared with 6 of them cured at 60ºC and the rest 6 cured at 100ºC. The sensors were further divided in to three groups based on the three different film thicknesses (200 nm, 300 nm, and 400 nm). Two samples of each thickness were fabricated for both main categories hereby referred to as crystalline (60ºC) and amorphous (100ºC) samples. The results and comparison of the crystalline and thermally modified amorphous PEO based device are presented in ***Figure 4-11***.

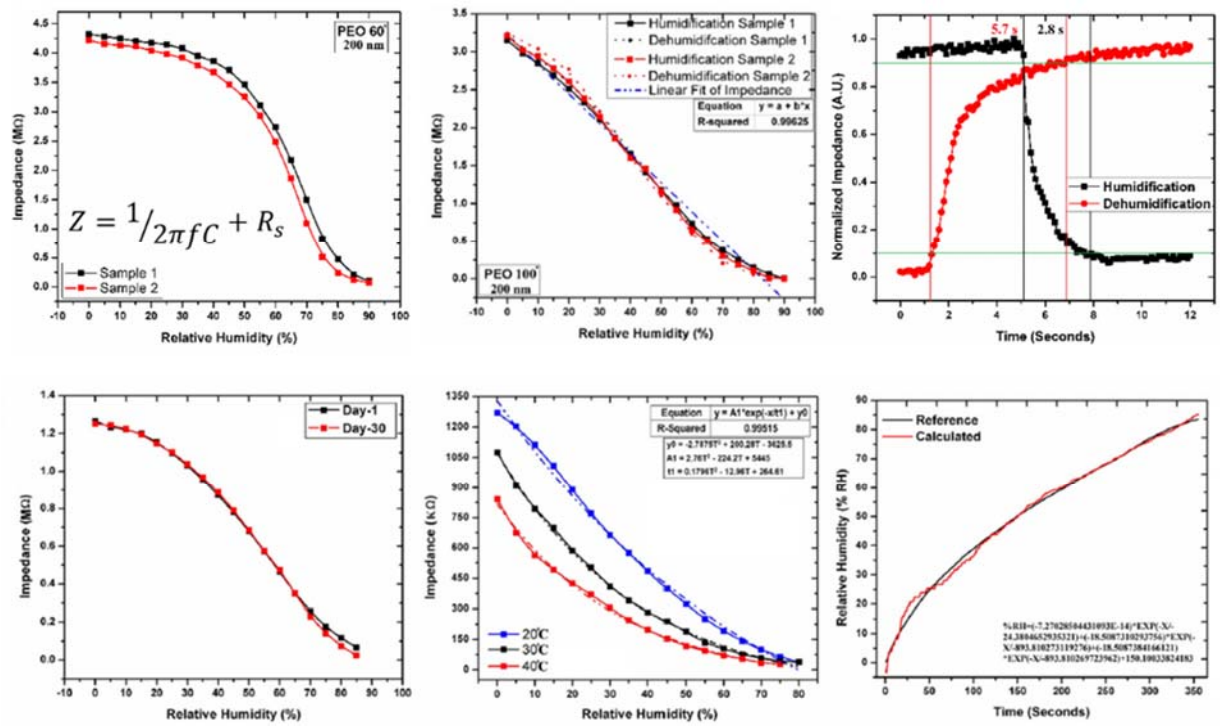

Figure 4-11: Impedance response of sensors based on (a) crystalline PEO, (b) modified PEO, (c) response time curves of amorphous device, (d) repeatability after 30 days, (e) temperature dependance curves, and (f) accuracy of detection.

The results show that the overall behavior of all sensors is the decrease in impedance of the sensors with increasing humidity levels. The intrinsic impedance increases with decreasing film thickness and almost has a linear inversely proportional relationship. The crystalline thin films show a non-linear behavior towards humidity sensing and the sensitivity is comparatively lower in the low humidity region while increases exponentially for higher humidity levels. The sensors based on amorphous PEO thin films also show inversely proportional impedance response towards humidity detection. The difference here is the response curve shape that is very close to linearity for the case of amorphous PEO films based sensors. The sensors are equally responsive towards low humidity levels as they are towards higher humidity levels. The intrinsic impedance of the sensors is also inversely proportional to the film thickness as in case of crystalline sensors. The impedance response gets saturated once the relative humidity reaches 90% RH and there is no more observable change in the impedance. This defines the range of detection for the sensors to be from 0% RH to 90% RH. The amorphous sensors show highly stable and repeatable response towards humidity detection. The results from sets of two samples fabricated at same conditions with same parameters are exactly overlapping with an average error of only ±2.4%. The humidification and desiccation curves show very low average hysteresis of only 2.37% for all samples combined with the minimum hysteresis value of 1.78% for the films with

least thickness of 200 nm as expected. The sensitivity was also maximum for the 200 nm thin film based sensors due to their higher intrinsic impedance and was equal to 35 KΩ/%RH. The response curve shapes for all amorphous sensors is almost linear with comparatively higher linearity visible in the samples with 200 nm thickness. This means that lower the film thickness, better is the overall performance of the sensor towards humidity detection in case of amorphous PEO thin films. The stability was investigated by recording the response curves of the sensor on the first day of fabrication and then leaving them in an open environment for 30 days. The complete impedance versus humidity curve was recorded again at day 30 and both curves were plotted overlapping each other. The average percentage standard deviation was calculated to be only 1% showing high stability and repeatability of the sensors. As temperature is an important factor in determining the ionic conductivity of the amorphous PEO thin films, the temperature dependence of the fabricated humidity sensors was investigated by taking their response curves at 3 different temperatures. The results show that the intrinsic impedance of the sensors decrease at higher temperatures and that is due to enhanced ionic conductivity of the amorphous PEO film at high temperatures. This results in higher sensitivity at lower humidity levels at elevated temperature. The mathematical relation between the temperature and impedance response of the sensors was also calculated. The results show that the sensors should be most suitable to be used for humidity sensing in temperatures up to and below 40ºC. The data was then used to find best fit curves and equations for our sensors that were solved by a microcontroller IC to directly output the sensors' response in terms of relative humidity. The results show excellent performance of the fabricated devices comparable to the high end commercial sensor with an average error of less than ±5%. The response and recovery times calculated for the crystalline sensor were 1.1 s and 1.7 s respectively while they were 2.8 s and 5.7 s for the amorphous PEO sensor. The recovery time is longer in the amorphous films owing to their enhanced affinity towards the water molecules that makes it difficult for the trapped OH^{-1} ions and water molecules to easily escape the film. The results however show the performance characteristics of the amorphous PEO thin film based sensor to be excellent and proves it to be ideal for real life applications requiring high sensitivity, accuracy, wide detection range, and fast response and recovery times.

7) A hybrid nano-composite of 2D hBN flakes and PEO polymer was then employed for humidity sensing active layer fabrication. Three different types of sensors were fabricated based on the active layer thickness having further three samples for each type making it a total of nine samples. The electrical response of all the devices was recorded as the change in impedance vs the change in relative humidity of the environment. The device results including

impedance response, response time, stability, and selectivity are presented in ***Figure 4-12***. The intrinsic device impedance of the sensors with maximum active layer thickness was found to be the minimum and vice versa. This was expected as the active layer thickness has a direct relationship with conductivity. Also, the curve shape for the device with highest active layer thickness was found to have more non-linearity when compared to the rest that can be attributed to the trapping of water molecules inside the thick film results in sudden drop of the impedance. The overall response curve of the sensors can be considered nearly linear that is desired for better performance and higher stability and repeatability.

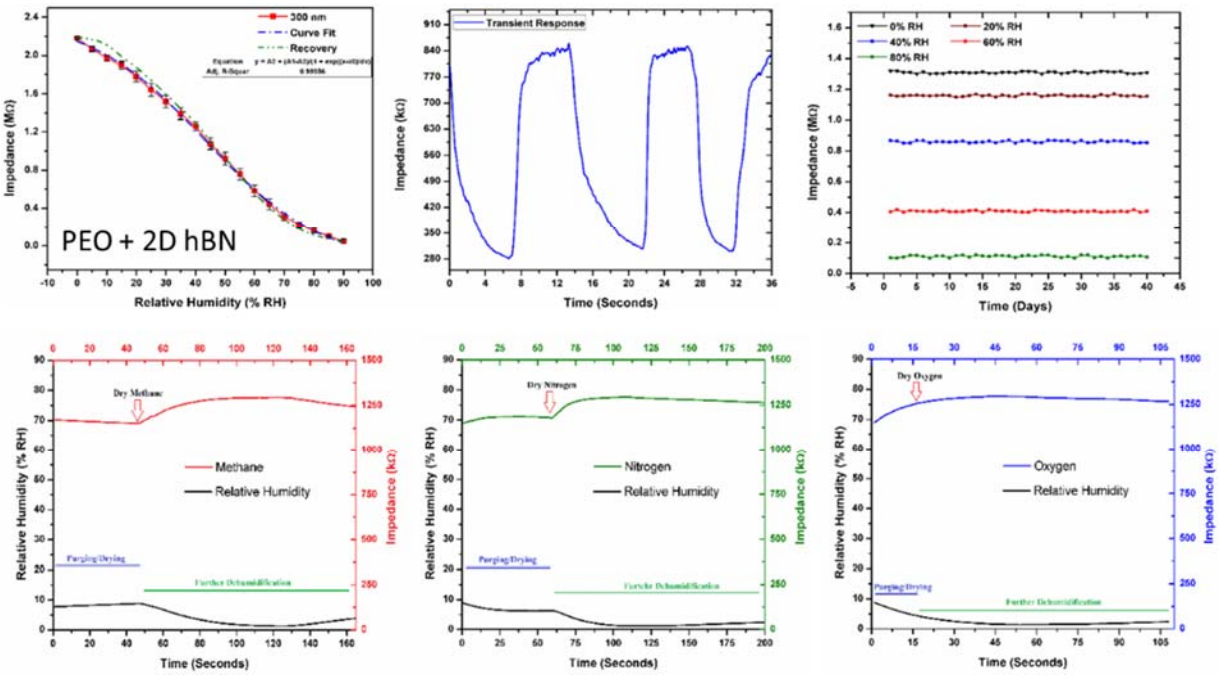

Figure 4-12: Performance of the hybrid device showing (a) impedance response of the sensor, (b) response time curves, (c) stability over 40 days, (d-f) selectivity for various gases.

The stability and repeatability of the sensors was investigated by recording full range response curves of the three samples of a single device type. The results show that all the three device samples have almost overlapping response curves with an average error of 2.61% that require minimal individual device tuning for quality assurance and accuracy. Furthermore, the devices were tested for their robustness and stability by recording the device impedance at five different humidity levels for consecutive 40 days. The devices were stored at room conditions otherwise. The results show that the output of the devices is highly stable with an average error of <2% that is better than most of the high end devices. The transient response of the sensors was recorded to investigate the response and recovery times of the devices upon humidification and desiccation. The transient response was measured by using two air

streams, one of compressed dry air, and the other of a highly humid air directly from the humidifier [57]. The perpendicular vector of the active area of the sensors was pointing towards the opening of the tube joint positioned at a distance of ~2 cm. Two electronic valves were quickly opened and closed just at the backend of the opening to expose the sensors directly to the output. The impedance data of the sensors was recorded and logged into a computer with a resolution of 0.1 s. Most of the humidity sensors are not tested for their selectivity towards the analyte and are prone to interference when exposed to certain gases. The fabricated devices here were tested for their selectivity towards various gases to ascertain no interference in the readings. The controlled humidity chamber was first purged using dry air from a dehumidifier. This step was eminent to make sure no other gases are present at that point. The relative humidity inside the chamber was reduced to around 8% through this step. After getting a stable reading, different dry gases were introduced into the chamber to check their effect on the device impedance. The relative humidity was continuously monitored inside the chamber during this process. The results of selectivity experiments show that as soon as the dry air is introduced into the chamber, the impedance of the device further increases but if the black curves showing the relative humidity are carefully observed, they show that the dry gas further purges the chamber and removes all the left our water molecules. The relative humidity drops from 8% to 0% and then quickly becomes stable. Similarly, the device impedance also becomes stable once the relative humidity is fixed even if the concentration of the gas increases. Similar behavior is eminent for all the three gases ascertaining that the fabricated humidity sensors are in-sensitive to common gases and have a high selectivity towards humidity.

8) Another device structure based on dual-element transducer was designed for the humidity sensors aiming at high performance parameters. Flakes of few layered MoS_2, a 2D transition metal dichalcogenide (TMD), were used in a unique combination with a conductive polymer PEDOT:PSS to fabricate a dual transducer element sensor where both the materials independently detect humidity in different ranges and their response is electronically merged achieve the desired parameters. 2D MoS_2 flakes have been employed for gas sensing applications but not tested for humidity senor fabrication yet. The thin film of 2D MoS_2 flakes possess a very high surface area to volume ratio and are ideal to detect low humidity levels with ultrahigh sensitivity. Three sensors were fabricated based on the active layers of PEDOT:PSS, MoS_2, and a series combination of both. The impedance of the all the sensors was recorded with respect to change in relative humidity and the test frequency was maintained at 1 kHz. The relative humidity of the controlled environmental chamber was slowly increased from 0% RH to 80% RH and the corresponding impedance values of the sensors were recorded. The results of the impedance response are presented in ***Figure 4-13***. The results show

that the impedance of the sensors decrease with increasing humidity levels for all three types. In case of MoS_2 based sensor, the relative decrease in the magnitude of impedance is very high for the initial half of the humidity range while it slowly gets saturated while entering the second half. The decrease in impedance for the MoS_2 based sensor is mainly due to the resistance drop of the thin film as soon as the humidity of the system is increased. Water vapors are readily adsorbed by the highly porous surface of the MoS_2 thin film and result in an ionic plus proton hopping based current flow through the few layered sheets of the 2D MoS_2 flakes. This quickly reduces the sheet resistance and the impedance of the sensor drops. Once the overall impedance of the sensor reduces from around 2.4 MΩ to several KΩ, the response gets saturated and no visible change is observable upon further increasing the humidity. The major part in case of MoS_2 for impedance change is played by the ionic current while a minor part is also played by the increase in capacitance of the thin film when the water molecules are physisorbed by the active layer. This increases the dielectric constant of the film, thus increasing the capacitance in return.

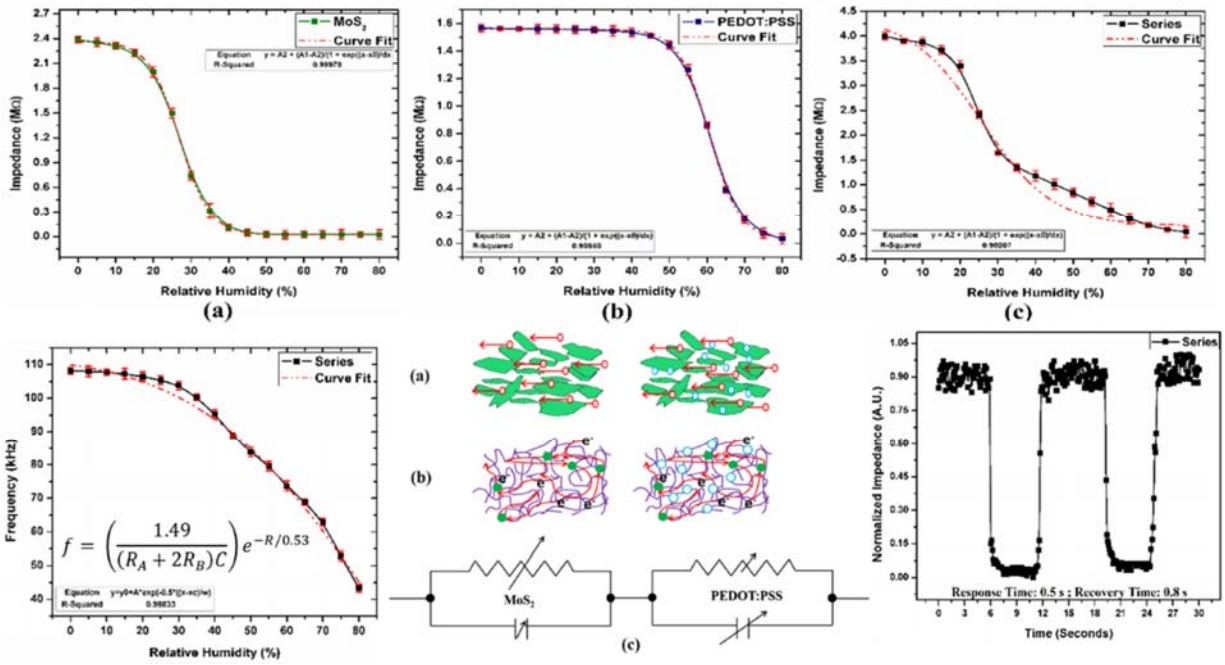

Figure 4-13: Impedance response of the sensors with active layers of (a) MoS_2, (b) PEDOT:PSS, (c) series sensor, (d) frequency response of the series device, (e) sensing mechanism and device model, and (f) response time of the series sensor.

In case of PEDOT:PSS based sensor, there is a relatively small change in impedance for the first half of humidity range while the impedance quickly drops while entering the second half. PEDOT:PSS is a conductive polymer and its resistance also drops with increase in relative humidity but the change is very small because the water molecules do not directly get involved in generating ionic current but only result in facilitating the flow of electronic current by

providing better paths to the already flowing current. This is why the relative change in the magnitude of impedance is very small for the lower humidity levels. At higher levels, the effect of change in capacitance of the thin film through physisorbed water molecules dominates in changing the impedance of the sensors. As the magnitude of impedance is still near 1.4 MΩ for PEDOT:PSS at the start of the second half, there is enough room for further decrease in impedance for the higher half of relative humidity. The simplified equivalent circuit of the resulting device shows that the total effective impedance of the two sensors will be the sum of the impedances of the two individual sensors. In ideal condition, MoS_2 based sensor will play its role for the first half in humidity detection and PEDOT:PSS based portion will play its role for the second half. The overall impedance changes from 4 MΩ to 10 KΩ from 0% RH to 80% RH. This give us an ultrahigh sensitivity of 50 KΩ/%RH that is higher than most of the reported sensors in literature with a wide detection range. To make a sensor suitable for commercialization, its output response should be in terms of a parameter that is easy for read out circuits available to the end user. For this purpose, we have converted the output of our sensors into change in frequency using an oscillator circuit. We can observe here that the magnitude of frequency decreases with increasing humidity for all three types of the sensors. The behavior of change in magnitude and the curve shapes have small differences when compared to the impedance response of the sensors. That can be explained using the frequency response formula of the circuit presented in equation 4.

$$f = \left(\frac{1.49}{(R_A+2R_B)C}\right) e^{-R/0.53} \quad (4)$$

R_A and R_B are two fixed resistances in the circuit, C represents the capacitance R represents the resistance of the equivalent circuit of the sensor. The equation is the modified form of a simple 555 timer based oscillator including the factor of a parallel resistance in the equivalent circuit of the sensing device. The effect of resistance is exponentially non-linear on the frequency and as the resistance decreases, the frequency also decreases. Due to the addition of a non-linearity in the output, the frequency response is not exactly the same as that of impedance response but the major theme is same, that is, increasing humidity decreases the frequency. It can also be observed that the curve shape of the frequency response is even closer to linearity that is better for the end user applications. The response and recovery times calculated for the MoS_2 based sensor were 0.4 s and 0.6 s respectively while they were 0.2 s and 0.3 s for the PEDOT:PSS based sensor. The series sensor gave response time of 0.5 s and recovery time of 0.8 s. The results show excellent performance characteristics of the series based sensor that are ideal for real life applications requiring high sensitivity, wide detection range, and fast response and recovery times.

In quest of good performance and low cost, researchers often tend to get inspiration from nature or use some basic off the shelf house hold materials for certain applications. This allows them to obtain properties and performance that are not usually possible even with expensive laboratory synthesized materials and chemicals. For example, carbonized chicken eggshell membranes with 3D architectures have been used for the fabrication of high-performance electrode materials for super capacitors owing to the suitable properties of the membrane [160]. Single cell thick onion membrane has been used to make artificial muscles that can both contract and expand upon bending [161]. The physical properties of the onion membrane suggested that it can be used for the certain application. Invertase-nanogold clusters decorated onion membrane has been used for fluorescence-based sucrose sensor [162]. In addition, further high level research is underway on wearable, implantable and transferrable devices [163]. Electronic device fabrication on very thin substrates is of high interest in this regard as these substrates exhibit high conformability, bendability, and lightness; which are crucial attributes for biological tissues sensing and wearable or implantable devices [164]. Most common methods of transfer printing of devices include water soluble sacrificial layers [165], PDMS stamping [166,167], and gecko printing [168]. A solution-based in-situ transfer method has also been used for hybrid thin film fabrication and transfer onto arbitrary substrates [169]. A high-yield two-step transfer printing method for large-scale fabrication of organic single-crystal devices on arbitrary substrates has been reported [170]. Nanowire devices have also been fabricated on diverse substrates by simple transfer printing methods [171,172]. Researchers are trying to combine the low cost, high performance, environmental friendliness, and transferrable printed electronic devices to achieve the best results. The conventional transfer printing methods are usually very complex involving multiple steps and are highly sensitive with high chances of device malfunction while transferring [130]. Moreover, the substrates yet used have only one function to support the device printed on them with no intrinsic sensing properties demanding additional functional layers to be printed on top. These polymeric thin film substrates are also not always bio-compatible.

9) An effort was made to employ a single-cell thick onion membrane as a humidity sensing active layer for the fabrication of an impedance based sensor while it also doubles as the device substrate owing to its high robustness and easy handling. Onion membranes are composed of plant cells which means they have an outer cell wall in addition to a cell membrane. This allows them to retain their structure even in case of deformation in the inner cell body upon dehydration[173]. The cell boundary acts as an osmotic membrane that is permeable to external solutions until an equilibrium is reached [173]. This phenomenon makes the membrane suitable to absorb permeable solvents

including water and can be used as a humidity sensing layer while its ultra-low thickness allows it to be transferred to arbitrary shaped substrates with high conformability. The transfer process is single step, very simple, and quite safe for the device. The overall device, thus, is a biocompatible, biodegradable, and disposable organic device that can be transferred to any arbitrary surface with a pretty good performance characteristics of relative humidity sensing from 0%RH to 80%RH. The results of the device performance are presented in ***Figure 4-14***. The impedance of the membrane depends largely upon water content inside the cells. The water adsorbed by the membrane can dissolve the dried organic materials inside the cells and provide a path for the flow of current.

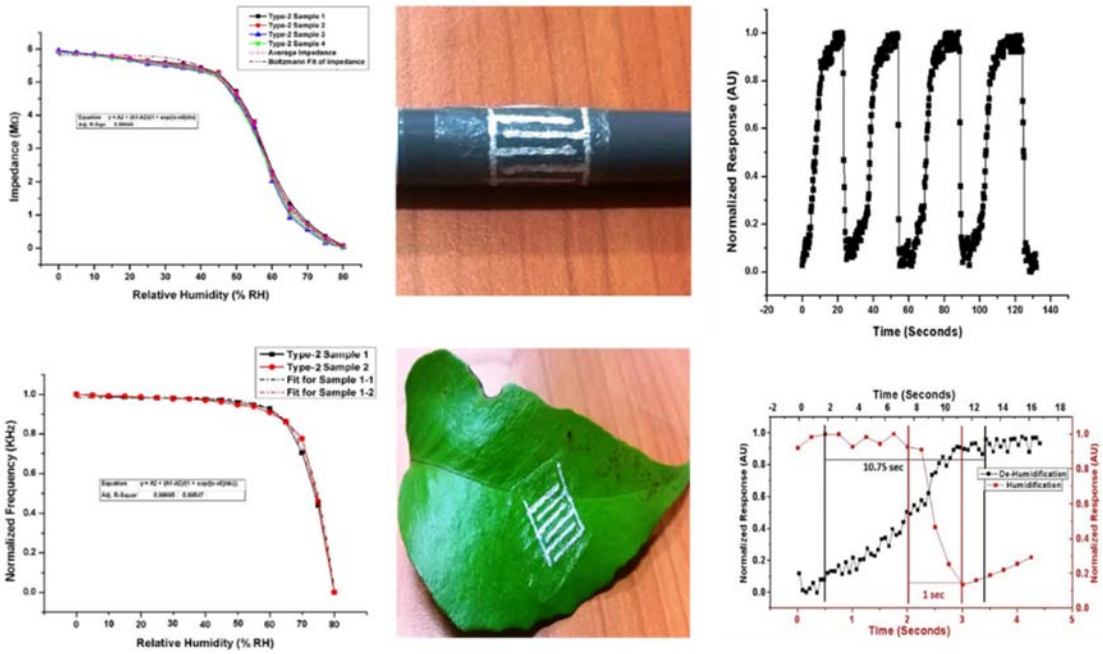

Figure 4-14: Impedance and frequency output response of the sensor, device after transferred to arbitrary surfaces, response time curves.

The water itself is also a comparatively very good conductor and its relative permittivity value also differs significantly from that of the dried membrane. Water is adsorbed or released by the cells following diffusion and osmosis principles through the cell membranes. Whenever there is a difference in the water contents level inside the cells and the outside environment, the membrane tries to gain equilibrium through diffusion and osmosis. The membrane keeps on releasing to or adsorbing the water vapors from the outer environment until an equilibrium state is reached between the inner cell environment and the outer environment. This fact is taken in to consideration and it serves as the basic working principle for the fabricated humidity sensors. The impedance response results indicate that the overall impedance of both types of the sensors decrease non-linearly with increasing relative humidity level. The output responses in terms of normalized frequency vs relative humidity also show that the frequency output of the

circuit decreases by increasing the humidity level of the chamber similar to the case of impedance. The response time estimated was 1.5 seconds while the recovery time was approximately 10.75 seconds. The fabricated sensor was then transferred/mounted onto various arbitrary shaped surfaces as target substrates. The substrates included flat surfaces, curved surfaces with different curvature radii, and arbitrary uneven surfaces. For transferring the device, the target surface was first wetted by water droplet and the non-printed side of the membrane was carefully placed on the wet surface. The membrane readily absorbs the water on the target surface upon coming in contact and becomes soft and highly flexible. In short, we can state that the response of transferrable biocompatible sensors fabricated by using a single cell thick onion membrane as both the substrate and the active layer for humidity sensing devices exhibit remarkable performance.

A detailed comparison table of the humidity sensing devices fabricated in this work with the humidity sensors in literature and top quality commercial sensors is presented as ***Table 4-2***.

Table 4-2: Detailed comparison of the performance parameters of humidity sensors in literature and market.

Materials	Material Category	Sensing Mechanism	Detection Range	Sensitivity	Response Time	Recovery Time	Selectivity	Error	Curve Shape	Reference
Polyaniline	Conductive Polymer	Resistive	47-87% RH	(12.5 kΩ/sq.)/%RH	27 s	60 s	Not Measured	5%	Linear	[149]
Polyaniline	Conductive Polymer	Resistive	20-85% RH	0.3 kΩ/%RH	5 s	Not Measured	Not Measured	Not Measured	Exponential decay	[174]
Graphene Oxide	2D Conductive material	Resistive	35-75% RH	49 nS/%RH	0.1 s	0.09 s	Not Measured	Not Measured	Linear	[175]
Polyvinyl Alcohol	Insulating Polymer	Optical	30-95% RH	0.54 nW/%RH	2 s	Not Measured	Not Measured	1 %	Almost Linear	[176]
Onion Membrane	Bio Material	Impedance Based	0-80% RH	Not Measured	1 s	11 s	Not Measured	5 %	Exponential Decay	[125]
Zinc Oxide	Inorganic Material	Resistive	5-85% RH	42.678%	3 s	12 s	Not Measured	Not Measured	Non-linear decay	[177]
Titanium Dioxide	Ceramic Nanoparticles	Resistive	30-90% RH	3.6 mV/%RH	58 s	65 s	Not Measured	Not Measured	Almost linear	[178]
PDEB	Organic Polymer	Impedance Based	15-92% RH	120 kΩ/%RH	Not Measured	Not Measured	Not Measured	3%	Exponential Decay	[152]

PPA, PDEB, & NaPSS	Substituted Polyacetylenes	Impedance Based	10-90% RH	100 kΩ/%RH	18 s	Not Measured	Not Measured	Not Measured	Non-linear decay	[155]
Graphene	2D Materials	Resistive	35-95% RH	15 %	Not Measured	Not Measured	Not Measured	Not Measured	Almost Linear	[179]
Graphene Oxide, Silicon	2D Material, Inorganic Material	Resistive	10-100% RH	27 µV/%RH	19 s	10 s	Not Measured	Not Measured	Almost Linear	[38]
Graphene, PSS	2D Material, Conductive Polymer	Impedance Based	30-95% RH	10 kΩ/%RH	3 s	22 s	Not Measured	Not Measured	Almost Linear	[180]
QC-P4VP, RGO	Polyelectrolyte, 2D Materials	Impedance Based	10-90% RH	1 kΩ/%RH	21 s	78 s	Not Measured	Not Measured	Non Linear Decay	[181]
Zn), CuTCNQ	Organic/Inorganic junction	I-V curves	0-75% RH	Not Measured	60 s	30 min	Not Measured	Not Measured	Linear	[182]
Graphene Oxide, PNaPSS	Composites	Capacitive charge pump	0-80% RH	35 µV/%RH	Not Measured	Not Measured	Not Measured	Not Measured	Almost Linear	[183]
LiCl, HPPMs	Composite porous polymer, Salt	Impedance Based	10-90% RH	Not Measured	2 s	32 s	Not Measured	Not Measured	Linear	[184]
Ce-doped ZnO	Inorganic Materials	Impedance Based	11-95% RH	1 MΩ/%RH	13 s	17 s	Not Measured	Not Measured	Non-Linear	[185]
TiO_2, LiCl	Inorganic Materials	SAW Based	25-65% RH	Not Measured	0.75 s	1 s	Not Measured	Not Measured	Non Linear Decay	[186]
HTU 21D	MEMS	Digital Output	0-100% RH	10 bit data	5-10 s	10 s	High	5%	Calibrated	Commercial
DHT22	Polymeric	IDT Based	0-95% RH	Digital output	5 s	>20 s	Not mentioned	2%	Calibrated	Commercial
Si7021	MEMS	Digital Output	0-80% RH	12 bit data	5 s	18 s	High	3%	Calibrated	Commercial
HS3 probe	Interchangeable	Analogue Out	0-100% RH	0.1 V/%RH	Not mentioned	Not mentioned	Not mentioned	1%	Calibrated	Commercial
2D hBN + PEO	Polymer + 2D Material	Impedance Based	0-90% RH	24 kΩ/%RH	2.6 s	2.8 s	High	2 %	Almost Linear	Current Work

The table clearly shows that the humidity sensing devices fabricated in this research work outperform most of the previously reported sensors in the literature and are better than most of the commercial sensors in terms of many performance parameters. This ascertains the role of materials and device structures to optimize the performance of the sensing devices.

4.1.3 Temperature sensors

A majority of research on temperature sensors development for target specific applications focuses on resistive sensors based on thermocouples and meander type electrodes [187–191]. Researchers try to change the materials of the electrode and their dimensions to achieve the required performance parameters like wider detection range and higher sensitivity [192–195]. The major drawbacks of this design include high processing temperature for fabrication, complex fabrication, low sensitivity, failure upon exposure to water, and complicated integration and conformability with 3D printed and arbitrary structures [196–198]. There is a lot of room available to solve these issues and develop sensors that can be seamlessly printed along with the main device or robot body. Advancement in 3D printing and additive manufacturing has enabled the fabrication of electronic sensing devices that were not possible through conventional methods [50,51]. They allow liberty in design and specifications and make it possible to fabricate embedded devices like sensors, organic light emitting diodes (OLED), field effect transistors (FET), and actuators inside a printed 3D structure [199]. A detailed review on 3D printed sensors has been presented in [52] which sheds light on the possibilities that this technique possesses in the field of printed electronics and functional device printing. Various printing methods and materials have been employed by researchers to fabricate devices like accelerometers, electrocardiography (ECG) electrodes, optical sensors, pressure sensors, tactile sensors, displacement sensors, temperature sensors, biosensors, chemo sensors, gas sensors, flow sensors, humidity sensors, antennas, and so on. Novel materials possessing properties like conductivity [53,54] and piezoelectric charge [55], compatible with 3D printing have been developed to give functionality to the printed structures rather than fabricating non-functional 3D models [56].

Graphene and polymers like PLA have been used in the form of composites to synthesize conductive functional materials compatible with 3D printing but their use has been mostly in applications to make conductive paths and circuit traces [200,201]. Commercial conductive filaments based on graphene and PLA composites compatible with FDM are also available. A linear resistive temperature sensor has been 3D printed through fused deposition modeling

(FDM) using a conductive filament based on poly lactic acid (PLA) and graphene nano rods (GNR) composite. The sensor is capable of measuring temperature variations based on the change in resistance of the printed pattern. As PLA is in-sensitive to and in-soluble in water, the sensor can be used both in air and under water without any need of encapsulation. Graphene nano rods give the printed patterns a conductive property while the PLA acts as a binder matrix. When the temperature rises, there is physical expansion of the polymer matrix at microscopic level that reduces the contact between the conductive GNRs and the resistance increases. Upon cooling down, the physical properties are retained and the resistance drops again. The results of the electrical characterizations of the sensors are presented in **Figure *4-15***.

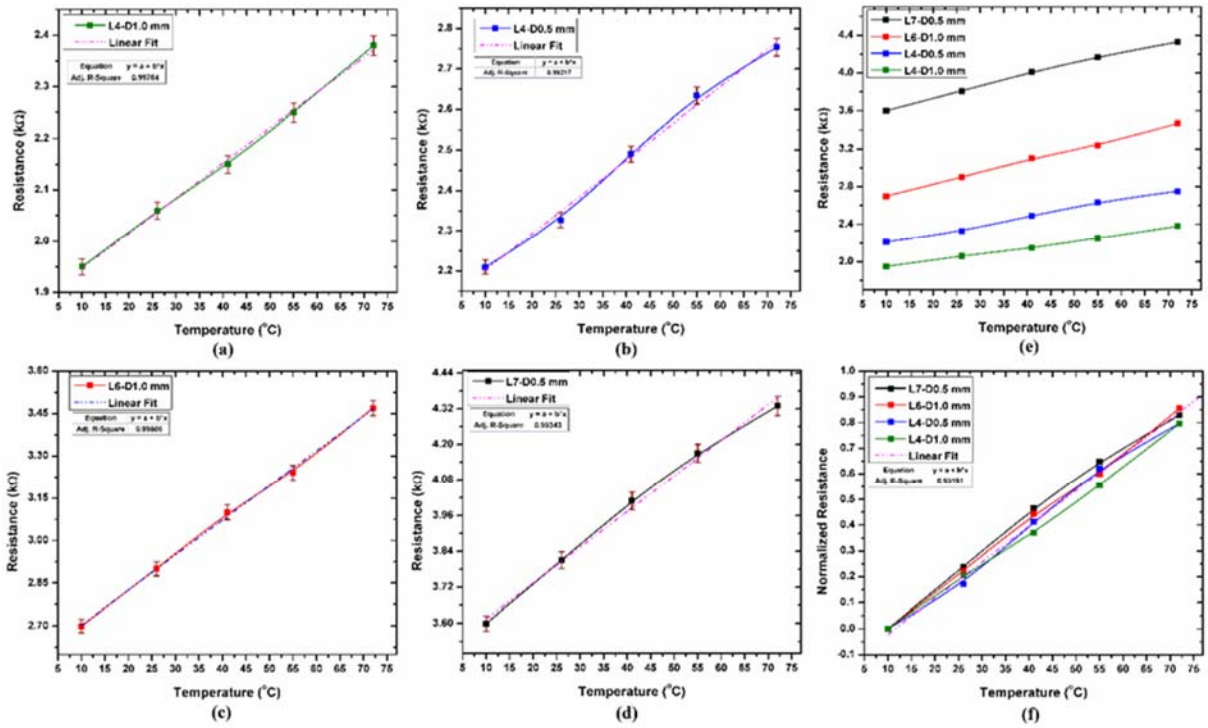

Figure 4-15: Resistive response of the sensors under water showing (a-d) the effect of changing the length and diameter of the printed patterns, (e) effect of dimensions on intrinsic resistance, and (f) normalized data showing linear behavior independent of dimensions.

Four sensors with different dimensions were printed to investigate the effect of length and cross-sectional diameter on their sensing performance. Three sets of readings were taken for each sensing device to verify the repeatability and statistical significance of the data. Error bars are included on each point that indicate the standard deviation of the readings. The magnitude of error bars indicate little error that is acceptable for the sensors in research. They also indicate that the readings of the sensors remain consistent and in the same range for repeated test cycles. The resistance of two sensors with an active region length of 4 mm and diameters of 1 mm and 0.5 mm lies between 2

kΩ to 3 kΩ approximately while of those with lengths of 6 mm and 7 mm lies between 3 kΩ to 4 kΩ approximately. All sensors have approximately equal lengths of printed connector lines. The major factor affecting the intrinsic/base resistance of the sensors is the length of the active region that is inversely proportional to the resistance. The diameter of the patterns has a direct relation with the sensors on the other hand. The sensor with the smallest diameter and the longest pattern has the highest resistance while the one with biggest diameter and shortest length has the lowest. Higher basic resistance results in higher sensitivity and vice versa. Absolute sensitivity per unit change of a linear sensor is the slope of the data and can be calculated using equation 5 [57]. The maximum recorded sensitivity for the fabricated sensors was ~13 Ω/ºC while the minimum sensitivity was ~7.2 Ω/ºC.

$$Sensitivity = (R_{max} - R_{min})/(T_{max} - T_{min}) \quad (5)$$

As the polymer matrix is based on PLA, the maximum operation temperature of the devices is limited up to 70ºC beyond which there is a permanent deformation and the resistance does not return to its original value. As the glass transition temperature of PLA is near 58ºC, the recommended operation temperature ranges up to and below 60ºC to get the most stable results with low hysteresis [202,203]. The operating temperature does not have any lower limit that makes the overall range well suitable for terrestrial and under water basic environmental and weather monitoring. The device with length of 4 mm and diameter of 0.5 mm was used to test the stability and transient response of the sensors. The resistance of this particular device changes from around 2 kΩ to 3 kΩ. The stability data of the sensors for a continuous 100 min operation shows that the output of the sensors remain stable and is free of any noise and uncertainty. The hysteresis in the sensors readings was recorded and the results are presented in ***Figure 4-16***.

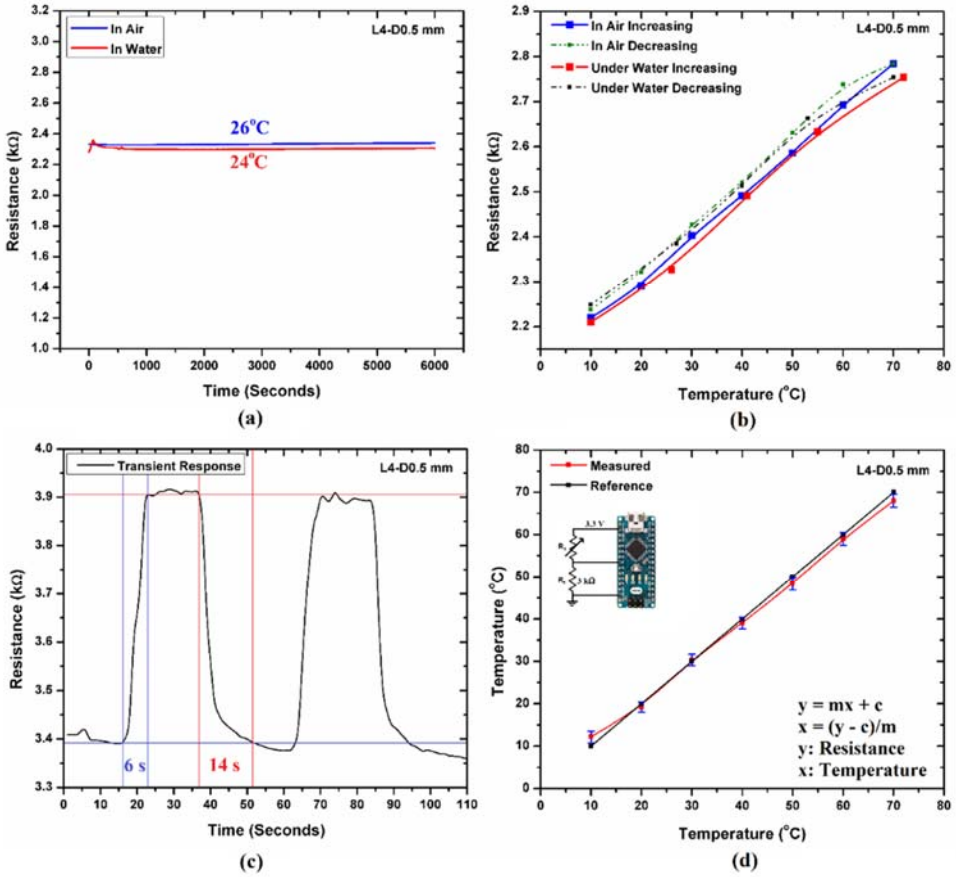

Figure 4-16: Performance evaluation of the device showing (a) stability for continuous operation for 100 mins, (b) hysteresis curves for in air and under water measurements, (c) transient response curves, and (d) measurement of actual temperature versus reference sensor.

The average percentage hysteresis was calculated using equation 6 [82] and was found to be 5.43%. In this equation, "n" is the number of samples, "y_k" is the measured value of the resistance and any given point, and "y_{max}" and "y_{min}" are the maximum and minimum values of resistance respectively. The results show that the sensors have an acceptable level of small hysteresis that does not have a significant impact on the accuracy and is comparable to the high performance devices developed previously.

$$Average\ Hysteresis = \left[\sum_{k=0}^{n} \frac{y_{k+1} - y_k}{y_{max} - y_{min}}\right] / n \qquad (6)$$

The transient response of the sensors presented shows that the response time of the sensors to change their value from 10% to 90% of the maximum for 0ºC to 50ºC was 6 s while the recovery time back to initial value was 16 s. Both these values are comparable to the high performance sensors presented in the literature.

The fabricated sensors were connected in a potential divider configuration to an ADC input of an Arduino based

microcontroller circuit that converts the digital data first to voltage, then to the resistance of the sensors, and finally to temperature. Equation 7 was used to convert the resistive response of the particular sensor into temperature output. Here "*D*" represents the digital data output of the ADC, "R_{ref}" represents the reference resistance, "*m*" shows the slope, and "*c*" represents the intercept. The fixed reference resistance used in the circuit was 3 kΩ whereas the slope was ~10 and the intercept was calculated to be ~2100.

$$Temperature = \Big(\big(R_{ref} + c\big)D - \big(cD_{max}\big)\Big)/\big(mD_{max} - mD\big) \quad (7)$$

The response of the sensor was recorded and plotted against a commercial reference sensor for comparison and the results show highly stable and accurate operation of the device in real life temperature measurement. A detailed comparison of the developed sensors with the similar and well recognized works in literature has been presented in ***Table 4-3***. The table covers the summary of all major performance parameters to evaluate the quality of the sensors and also includes the device structure, materials, and working principles. Information on similar commercial sensors is also included to give a better idea about the performance requirements of application specific sensors in this category.

Table 4-3: Comparison between performance parameters of different commercial temperature sensors and those in literature.

Materials	Fabrication Method	Device Structure	Sensing Mechanism	Detection Range (ºC)	Sensitivity	Transient Response	Environment	Curve Shape	Reference
Gold	Sputtering	RTD	Resistive	Up to 120	5 mΩ/ºC	1.7 s	Dry Only	Linear	[204]
PDMS +Ag Flakes	Mold and Filler	Single line pattern	Thermal Expansion	Up to 80	0.375 Ω/ºC	400 s	Dry Only	Non-linear	[205]
Silver	Inkjet Printing	Meander	RTD	Up to 60	4.5 Ω/ºC	NC	Dry Only	Linear	[206]
RGO +AgNC	Mechanical Masking	Single line pattern	Resistive	Up to 80	0.405 Ω/ºC	NC	Dry Only	Linear	[18]
Graphene	Inkjet Printing	Film on electrodes	NTC Resistor	Up to 160	0.0148 K^{-1}	10 s	Dry Only	Non-linear	[207]
Graphene	Lithography	FET	Mobility dependent	Up to 600	3.15x10^{-3}/ºC	NC	Dry Only	Non-Linear	[208]
ITO, Ag, HSMG	Laser Ablation	Thin Film Resistors	Resistive	Cryogenic	NC	NC	Dry Only	Non-Linear	[102]
Graphene PEDOT:PSS	Inkjet Printing	Meander	NTC Resistor	Up to 45	0.06%/ºC	20 s	Dry Only	Linear	[209]
GNWs PDMS	Polymer Assisted	Thin Film Resistor	Thermal Expansion of	Up to 120	109 Ω/ºC	1.6 s	Dry Only	Non-Linear	[16]

	Transfer		PDMS						
Silicon	MEMS	DETF	Resonant Frequency	Up to 60	632 ppm/K	4 s	Dry Only	Linear	[210]
Silver	Inkjet Printing	Meander	RTD	Up to 100	0.155 Ω/ºC	NC	Dry Only	Linear	[211]
CNTs	Lithography	Layered Electrodes	Ionization	Up to 100	0.04/K	NC	Dry Only	Non-linear	[212]
TMP36	Lithography	MEMS	Voltage output	Up to 125	10 mV/ºC	20 s	Both Dry and Wet	Linear	Commercial
LM35	Lithography	MEMS	Voltage output	Up to 125	10 mV/ºC	8 s	Both Dry and Wet	Linear	Commercial
DS18B20	Lithography	MEMS	Digital Output	Up to 100	12 bit resolution	NC	Both Dry and Wet	Digital	Commercial
TMP37	Lithography	MEMS	Voltage Output	Up to 100	10 mV/ºC	NC	Both Dry and Wet	Linear	Commercial
GNR+PLA	*3D Printing*	*Single line pattern*	*Thermal expansion of polymer*	*Up to 70*	*12 Ω/ºC*	*6 s*	*Both Dry and Wet*	*Linear*	*Current Work*

The table indicates that the current sensor competed with the best of the sensors previously reported for the same applications. The sensor has better sensitivity than most of the previously reported devices while the transient response is also amongst the best. The sensor can be operated in both dry and wet conditions that is a better characteristic than most of the competitors. The limitations, however, are the smaller detection range and possibly less accuracy when compared to the commercial devices.

4.2 Bio Sensors

Biosensors cover a wide variety of sensing devices including immunosensors, DNA & RNA sensors, bacteria sensors, ECG, EEG, breath detection, blood pressure monitors, O_2 sensors, pH sensors, toxicity sensors, heavy metal ion detectors, glucose sensors, muscle movement detectors, electronic nose, electronic tongue, cell detectors, and so on. Each one of the mentioned sensor types is a field in its own with a lot of research going on. Like the other sensor categories, the main goal of research in biosensors is also improving the performance parameters. In this research work, two of the mentioned sensor types including immunosensors and muscle movement detectors have been developed. The aim was to develop multi-reagent immunosensors for point of care diagnosis and flex sensors for human posture detection for human machine interface (HMI) and as translators for sign language for vocally impaired.

4.2.1 Immunosensors

Immunosensors are compact analytical devices that are used to detect the formation of a complex resulting from an antigen-antibody interaction using transduction techniques to generate an interpretable and process able output signal. The different types of transducing mechanisms are based on difference in generated signals or changes in properties when a complex is formed [213]. Immunosensors are well recognized standard bio detection devices employed in laboratories for disease diagnosis, food industry for safety testing, and for general environmental contamination monitoring. The essential foundation of all the immunosensors is to specifically recognize antigens by antibodies to form a stable complex [214]. Immunosensors have been successfully fabricated and tested to reliably sense various bioactive elements like DNA [6], viruses [7,8], enzymes and cell receptors [9], glucose and other chemicals, proteins, and hormones [10,11], etc.

There are a number of working principles on which the immunosensors can be fabricated. They can be based on chromatography, fluorescence, electrochemical variation, mass spectrometry, surface plasmon resonance, lateral flow, etc. [47–49]. Electrochemical immunosensors have received considerable attention owing to their ease of use, reasonable limit of detection (LoD) with a small sample volume, and being a simple analytical platform [215]. The most promising applications of electrical biosensors include situations where low cost, small setup size, and speedy results are crucial but high end and high accuracy results are not a priority for example, in point of care diagnosis for house hold personal use, emergency situations like in an ambulance, routine clinical checkups, water quality check, and screening [216]. There are further different categories in the electrochemical immunosensors based on their working principles that include coated paper based chemristors [217], potentiometric sensors [218], amperometric sensors [219], sandwich type structures [220], IDT based sensors [221], and most commonly, field effect transistors (FETs) [222].

FET based biosensors have attracted much attention owing to their rapid, inexpensive, and label-free detection. They have lower sensitivity as compared to other non-electrical methods but that problem is being addressed by using 1D and 2D structures like nanowires and 2D transition metal dichalcogenides (TMDCs) instead of bulk materials [59,223]. TMDCs have multiple layers with strong in-plane bonds and weak out-of-plane interactions enabling easy exfoliation into 2D sheets having scalable bandgaps making them ideal for using in electronic sensing devices. The examples of these materials used for bio sensing include MoS_2, $MoSe_2$, WS_2, and WSe_2 [59,224,225]. The most common among these TMDCs is MoS_2 that has been employed in various sensing applications like gas sensing, chemical vapor sensing, and

bio sensing, etc. based on its excellent electrical properties and comparatively easier synthesis and processing [226,227]. Yet, the biggest limitations with using lower dimensional materials in FET based bio sensors are the severe fabrication challenges, impairing their practical applications [223].

In this research work, we have fabricated an impedance based immunosensor using an interdigitated transducer (IDT) electrodes with MoS_2 as the electrically active sensing layer. This design compensates for the lower sensitivity issues associated with general FET based sensors by offering a large surface area for detection and combines the advantages of TMDCs by implying a few-layered TMDC material as the active layer [228]. The fabricated sensor is aimed for clinical commercialization to detect general antibody-antigen based bioactive elements. The fabricated sensors were then employed for the targeted detection of the specific antigens including prostate specific antigen (PSA), mouse immunoglobulin-G (IgG), and nuclear factor kappa-light-chain-enhancer of activated B cells (NF-κB).

PSA is a widely used clinical tumor biomarker for prostate cancer detection [229]. PSA sensors have a wide range of reported limits and ranges of detection including [229–231]. The minimum required detectable amount of PSA in human blood serum is 2ng/ml for clinical diagnosis [216,232] while the normal range is 0 to 4ng/ml. ***Figure 4-17*** presents the response of the fabricated sensors for quantitative detection of PSA. The results indicate that the immunosensors are highly responsive towards PSA detection.

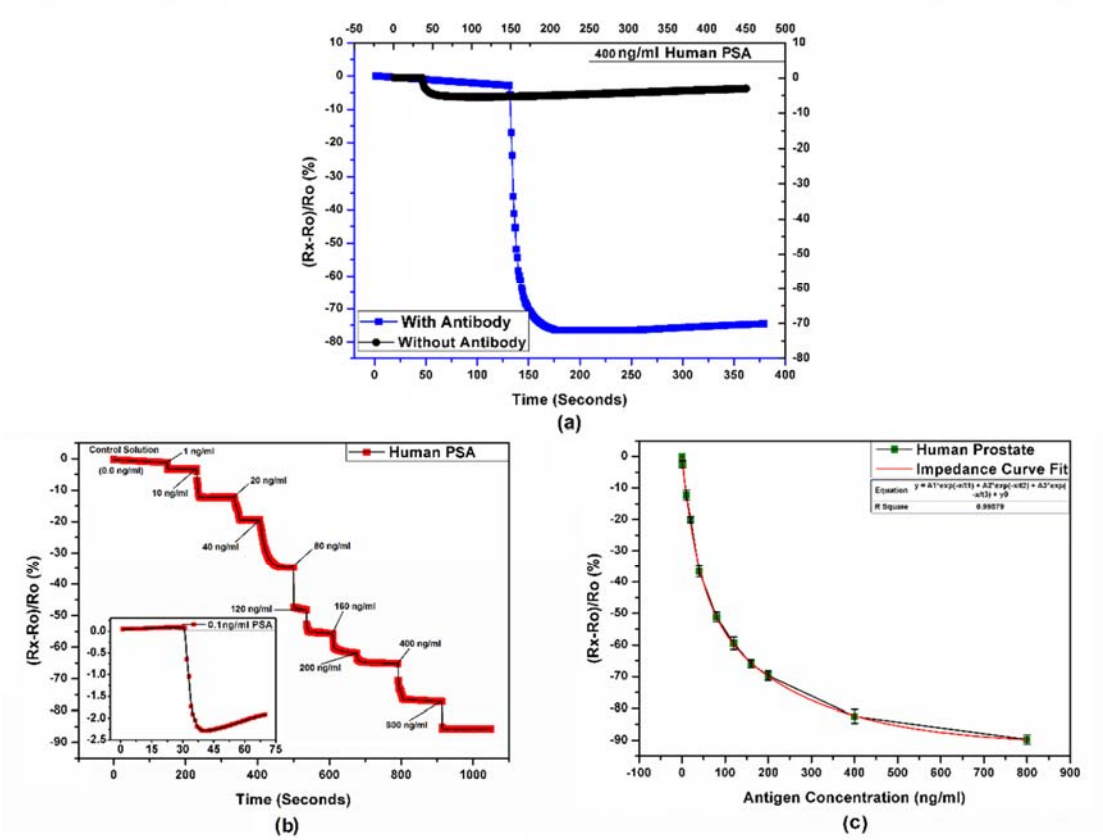

Figure 4-17: Output characteristics of PSA immunosensor (a) response for 400ng/ml PSA with and without immobilized anti-PSA antibodies, (b) step response curve showing stable readings with time for increasing concentrations of PSA with inset showing LoD curve for 0.1ng/ml PSA, and **(c)** response curve representing the behavior of the sensors for the full tested range of PSA concentrations.

The effect of target specific detection through antibody immobilization was investigated by using the sensors coated with MoS_2 thin film with and without immobilized antibodies were used for PSA detection. It can be seen that the resistance of the sensor still drops a little bit for a 400ng/ml PSA solution due to the general conductivity of the protein and sudden distortion in the electric field of the IDT but as there are no antibody attachment sites available on the surface, the effect slowly dies off and the resistance slowly climbs back up. It is important to note that the maximum change is only ~8% in this case that further reduces to ~3% after few minutes. The same concentration of PSA for the sensor with immobilized antibodies shows a ~78% change in impedance and the readings remain stable even after 6 minutes indicating the successful antibody-antigen complex formation. This shows a signal to noise ratio (SNR) of >10 that has a high significance value [233]. These results confirm high selectivity of the sensors for the specific type of antigen detection with negligible response towards unwanted compounds present in the test sample. The time based step response indicates quick detection of varying concentrations of antigen in the solution and show that the readings remain stable. The concentration vs percentage change for three trials indicates the response curve

shape of the sensor output towards different PSA concentrations. If the sensor is aimed for quantitative detection of the analyte, the range of detection (RoD) is very important. RoD is the ratio of the largest measurable target concentration and the limit of detection where the upper limit is set by the saturation of electrode/probe. The RoD for PSA for the fabricated sensor is 1ng/ml to 800ng/ml while the limit of detection is 0.1ng/ml. Both these values lie well within the required clinical ranges for prostate cancer diagnosis.

Serum immunoglobulin level measurement is a routine clinical practice as it gives important information about humoral immune status [234]. Various sensors for the detection of IgG have been fabricated using a variety of sensing techniques and different ranges of LoD and RoD [220,235–240]. ***Figure 4-18*** presents the response of the fabricated sensors for quantitative detection of mouse IgG. The results for 400 ng/ml IgG show a high significant SNR of >11 proving the high specificity of the sensors similar as in case of PSA. The LoD for IgG was found to be 1ng/ml while the RoD of 9000 (1ng/ml to 9µg/ml) was achieved. The readings become quickly saturated for higher concentrations of IgG that was found to be the result of lower concentration of immobilized antibodies.

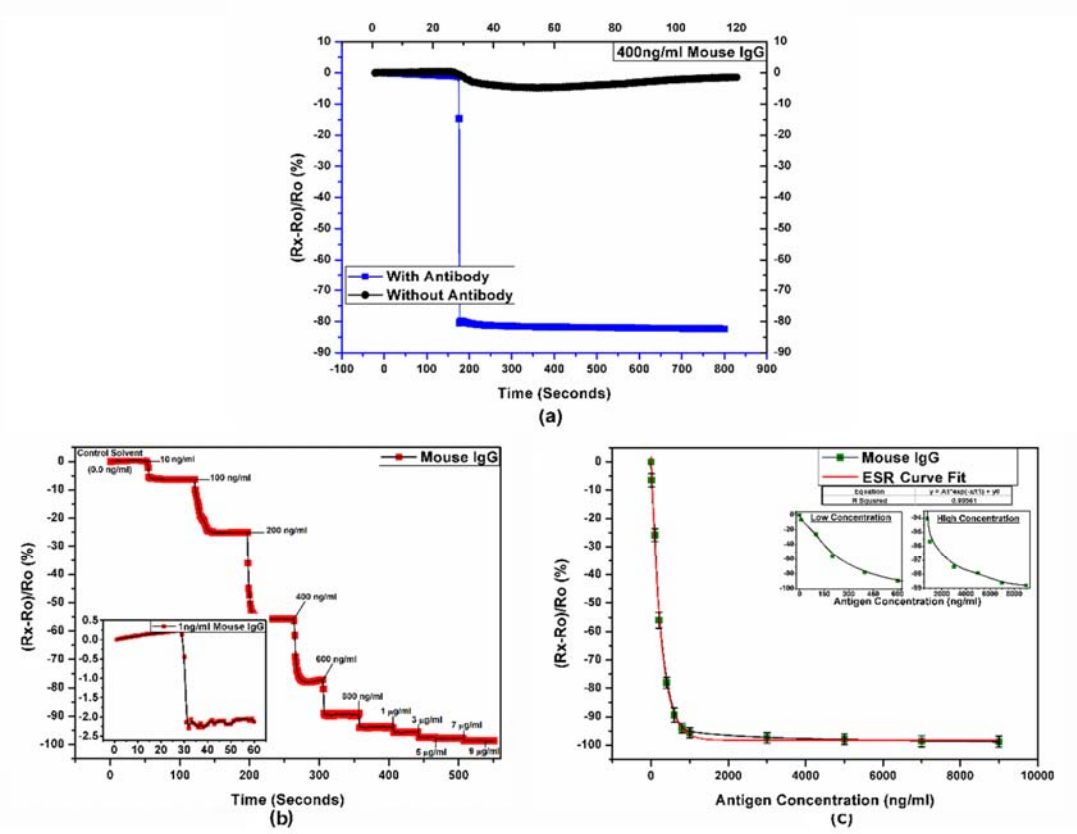

Figure 4-18: Electrical characteristics of the IgG immunosensor (a) response towards 400ng/ml IgG with and without immobilized anti-IgG antibodies, (b) step response for increasing concentrations of IgG with inset showing LoD curve for 1ng/ml IgG, and (c) response curve for the full tested range of IgG with insets

showing the separated curves for low (0-800ng/ml) & high (800-9000ng/ml) concentration ranges.

For a better detection range, comparable amount of antibodies to the targeted amount of antigen have to be immobilized. In this case, the immobilized antibodies are in concentration of 1µg/ml while the targeted detection is for 9µg/ml of antigen. The results would have been much better if a 10µg/ml solution was used for antibody immobilization as presented in case of POC diagnosis.

Transcription factor of the nuclear factor κB (NF-κB) is involved in large number of genes regulation and is associated with diseases like inflammation, asthma, atherosclerosis, septic shock, arthritis, and even cancer [241,242]. The antibody used here, NF-κB p65 recognizes endogenous levels of total NF-κB p65/RelA protein and does not cross react with other NF-κB/Rel family members. One of the few reported ones use biomarkers and optical methods and their LoD and RoD are not clearly defined [243]. The literature suggests that there is not enough work done on direct NF-κB quantitative detection. ***Figure 4-19*** presents the response of the fabricated sensors for quantitative detection of NF-κB.

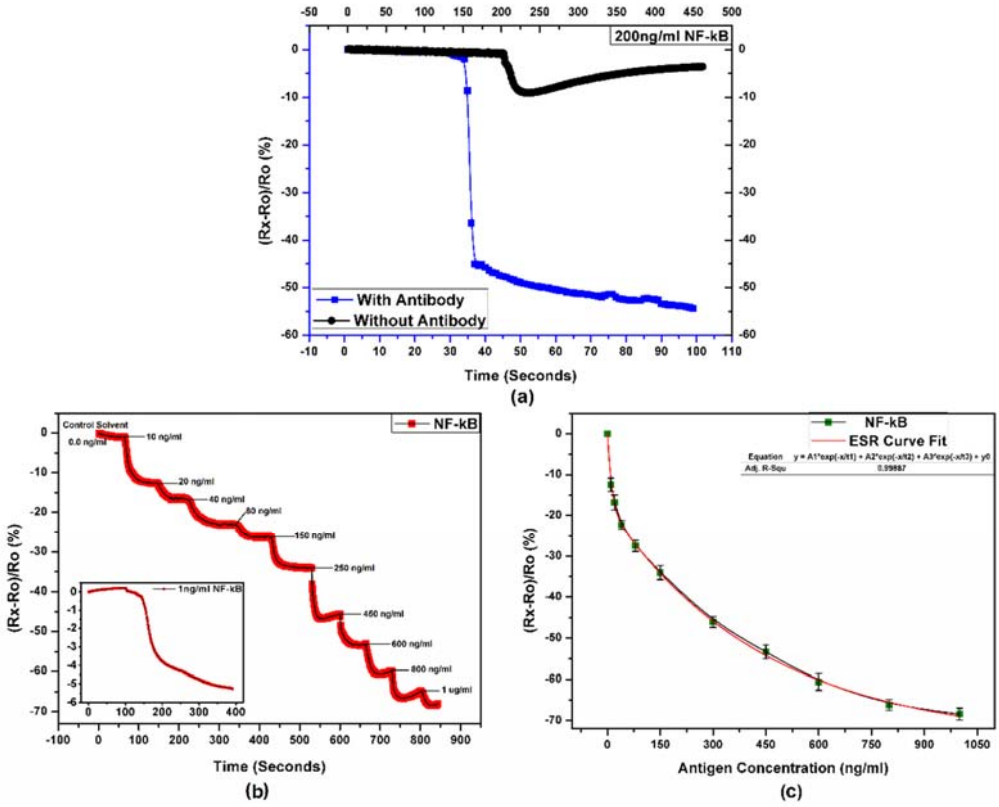

Figure 4-19: NF-κB immunosensor response (a) addition of 200ng/ml NF-κB to sensors with and without immobilized antibodies, (b) step response showing stable readings with time for increasing concentrations of NF-κB with inset showing LoD curve for 1ng/ml NF-κB, and (c) response curve for the full tested range.

The results show that the SNR for NF-κB is ~5, the LoD is 1ng/ml, while the RoD is 1000 (1ng/ml to 1000ng/ml). The results show that the developed setup is ideal for commercialization as a general purpose household self-diagnostic kit for multiple bio-reagents after further refining using microfluidic chambers, higher resolution reference sensors, rigorous calibration using large number of samples and testing on various bio-reagents.

4.2.2 Point of care diagnosis

For electrical characterizations, a 100µl control solvent was added to the active portion of the fabricated sensor and the impedance and AC effective series resistance (ESR) were recorded at 0% antigen concentration as the reference/control value. The followed protocol is similar to the water gated FET based sensors [223] but the third (reference) electrode is not required in this scheme as CV is not used here but the net change in resistance between the two electrodes is recorded. A small sinusoidal voltage of a particular frequency was applied and the change in resulting AC current output was measured similar to chronoamperometry. The ratio of input voltage and output current gives the effective impedance. This method is also referred to as electrical impedance spectroscopy by some researchers [216]. The principle of impedance change is majorly dependent on dielectric charge transfer and electrolyte conductivity rather than the redox reactions. The advantage of using this scheme is that even if there is a redox reaction occurring in the faradic zone, the direct electron transfer will also result in the change in impedance of the sensor, thus improving the sensitivity by a great extent. Small amounts of specific antigens were added to the solvent that were selectively bound to the antibodies immobilized on MoS_2 thin film resulting in impedance change. The real time data was automatically logged in and plotted on a computer with a sampling rate of 1s. The complete process of fabrication, functionalization, detection and characterization is presented in ***Figure 4-20***. The concentration of the antigens were kept being increased to a point until the readings start to saturate and there was no significant change in response upon further increase in concentration.

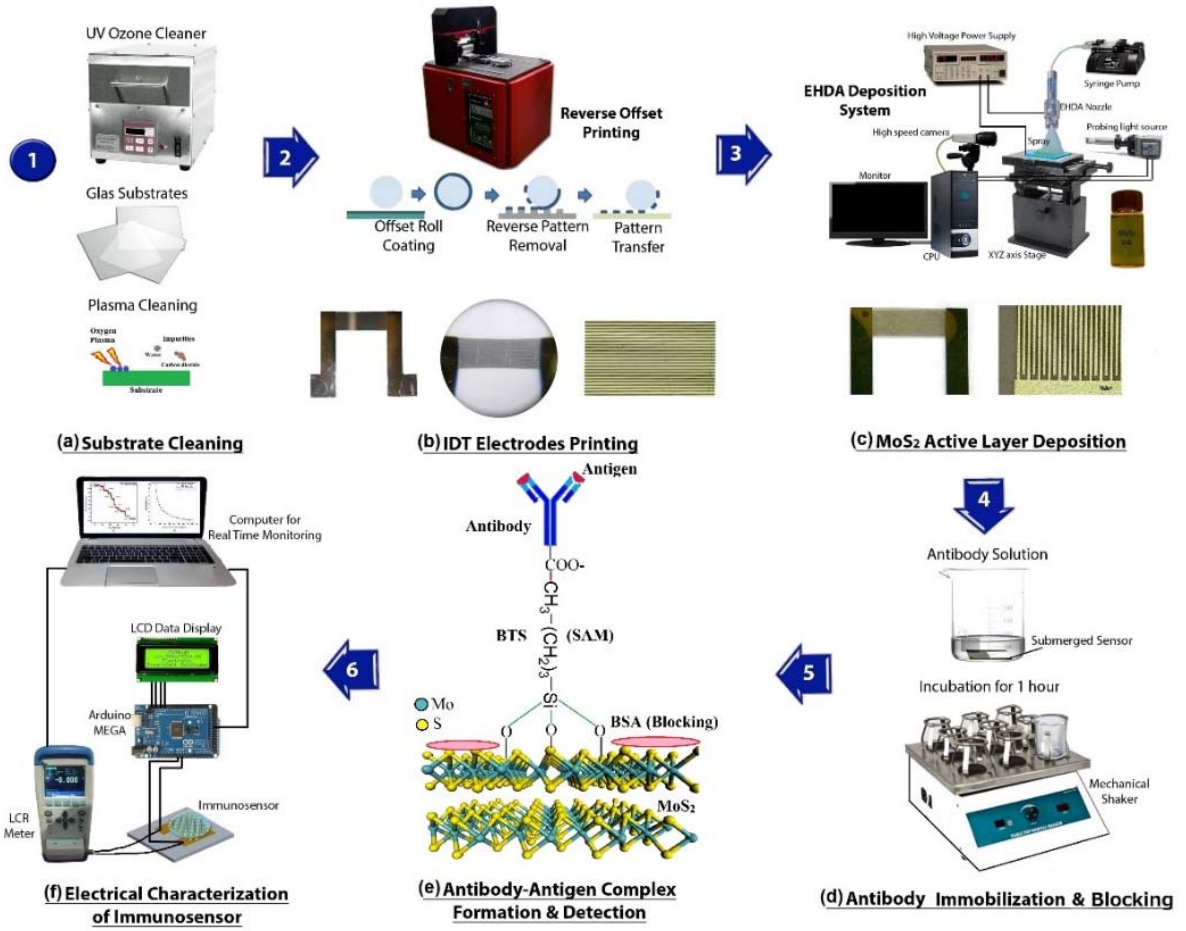

Figure 4-20: Process flow diagram of sensors fabrication and characterization (a) Substrate cleaning by plasma, (b) Electrode fabrication by reverse offset printing, (c) MoS2 active layer deposition by EHDA, (d) Antibody immobilization and blocking, (e) Antibody-antigen complex, and (f) Sensors' electrical response

Point of care (POC) diagnosis is the real time sensing of the target analytes or bio-reagents. POC devices currently available for clinical tests include detectors of bacterial infections, viral infections, non-communicable diseases (PSA for prostate cancer, proteins for inflammation), and parasitic infections [244]. In this research work, we selected IgG as the target analyte to be detected using the POC setup. The same system can be used with other bio-reagents after individual calibration. The system was first optimized using known concentrations of IgG and the trends were calculated. The POC system and step by step detection process is presented in ***Figure 4-21***. After calibration, the system was used for the quantitative detection of the IgG antigen. A smartphone application was designed for a guided seamless diagnosis. The readings are displayed after an average of 40 seconds when the system calculations are finished.

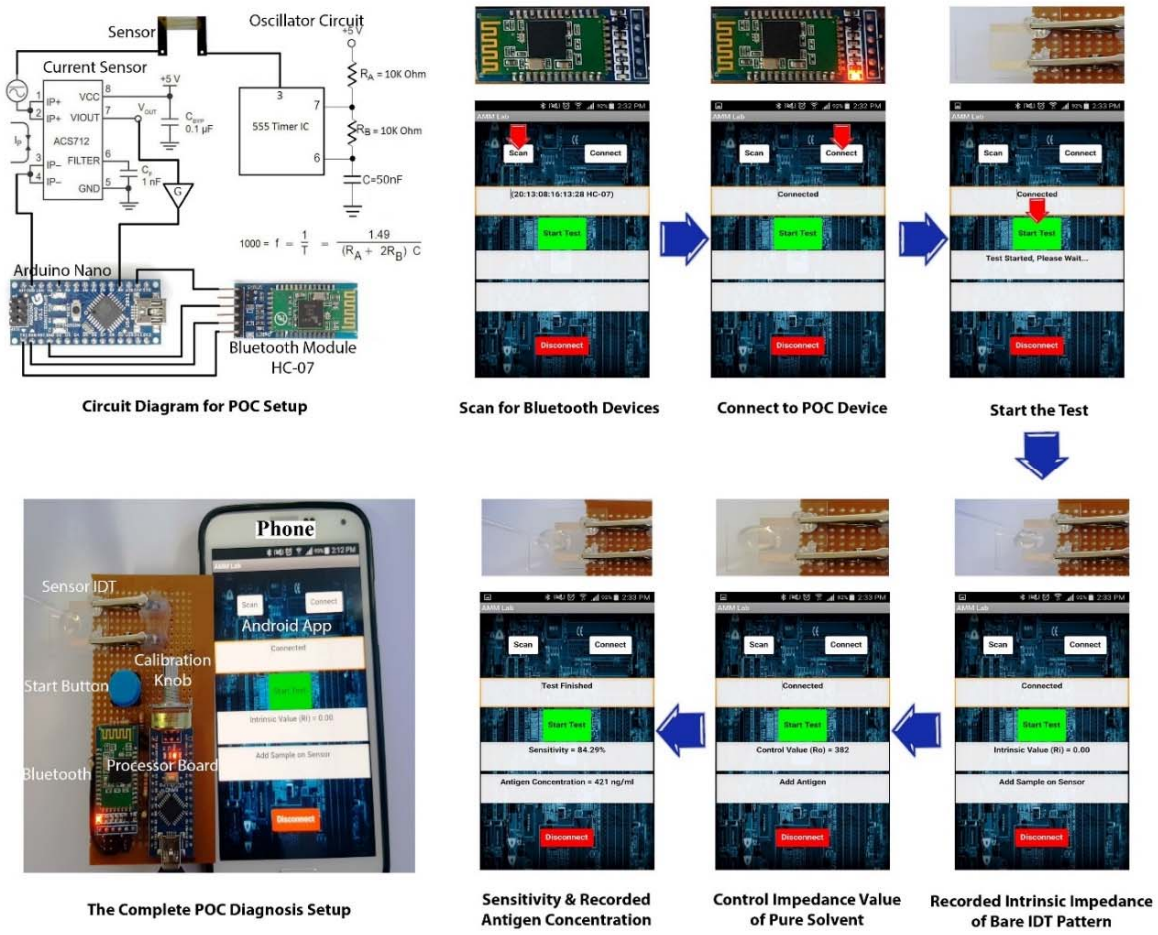

Figure 4-21: Point of Care (POC) Diagnosis process with (a) showing the circuit diagram, (b) showing the real picture of setup, and (c) showing the step by step diagnosis process using the developed Android smart phone application.

The basic circuit diagram for the detection circuit is presented here in but the detailed circuit diagram is not presented that also includes amplification and conditioning portions to improve signal to noise ratio (SNR) and sensitivity. First, the reading of the current without the control solvent was recorded and then the control was added to start calibration and record the base impedance. After that, a known amount of antigen is added to the control solvent and the system automatically waits for the readings to get stabilized. The percentage sensitivity is calculated and stored. The general purpose immunosensors were tested for POC diagnosis using IgG as the target bio-reagent. Four different concentrations of IgG were used for calibration of the test setup. Intensive programming routines were used for minimizing the error and improve repeatability. The system was optimized to detect the IgG in range of 0 ng/ml to 600 ng/ml where it shows almost linear behavior. The results of percentage sensitivity from the calibration readings for known solutions of 0 ng/ml (control), 100 ng/ml, 300 ng/ml, and 600 ng/ml having 3 sets of samples for each concentration are presented in ***Figure 4-22***. The results show stable behavior of the fabricated test setup with

an average error of approximately ±5.8%.

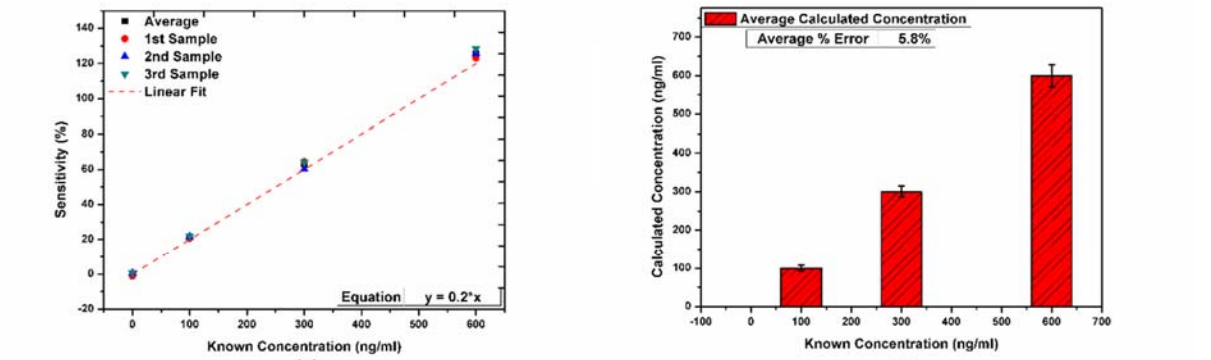

0 ng/ml				100 ng/ml				300 ng/ml				600 ng/ml			
Ro	Rx	% S	Conc (ng/ml)	Ro	Rx	% S	Conc (ng/ml)	Ro	Rx	% S	Conc (ng/ml)	Ro	Rx	% S	Conc (ng/ml)
380	375	-1.32	-6.58	367	443	20.71	103.54	370	608	64.32	321.62	376	839	123.14	615.69
371	373	0.54	2.70	381	464	21.78	108.92	384	615	60.16	300.78	380	858	125.79	628.95
370	372	0.54	2.70	366	447	22.13	110.66	366	601	64.21	321.04	368	841	128.53	642.66

(c)

Figure 4-22: Results of IgG detection using POC setup (a) calibration readings for known concentrations, (b) difference between calculated and known values, and (c) presenting the table with all actual recorded readings from POC diagnosis setup.

For the final device evaluation, two different concentrations that were not used in calibration were detected using the setup. For 400 ng/ml solution, the output given by the system was 421 ng/ml that has an error of approximately +5.4%. For 200 ng/ml known concentration, the recorded output was 213 ng/ml showing +6.9 % error. Further calibration and fine optimization can be done to make the results more consistent and further reduce the error percentage. For initial stages, the stability and repeatability of the presented diagnostic setup is very acceptable.

4.2.3 Body posture detection sensors

Flex sensors are widely used in human machine interface (HMI) devices to control their operation using gestures [245–249]. Flex sensors are also used to interpret sign language by mounting them on gloves and interfacing with signal processing circuits [250–252]. Strain and flex sensors have been applied in health monitoring to measure the muscle joint angle and movement [253–255]. Flex or bend sensors are simpler form of strain sensors that can only measure bending in contrast to strain sensors that are also able to measure elongation or strain in addition to bending. This simplicity makes the flex sensors easier and cheaper to fabricate as compared to strain sensors [246]. Mostly, the working principle of cheap flex sensors is based on resistive active layers whose resistance changes upon the change in bending angle with respect to their resistance while at straight position [256].

A highly stable low cost flex sensor has been fabricated in this research work using micro-gravure mass production

roll-to-roll printing system. The active layer was fabricated on PET substrate using composite of Activated Carbon with PVDF. PVDF has been added as a binding agent to improve the mechanical stability of the active layer. Protective coating of PVAc was deposited on top of active layer using the same system. The sensors' electrical response was measured using *Applent AT825 LCR Meter* and by connecting it to computer for data logging and processing. The measurement setup for different bend angles is similar as used in [257] and the system schematic is presented in ***Figure 4-23***. The setup is capable to take user input of angle from a GUI based software and can precisely bend the sensors to the target angle while simultaneously recording the resistance of the device in an automatically generated computer log file. *Arduino UNO* was used for multi-channel interface and data processing for sensors mounted on glove.

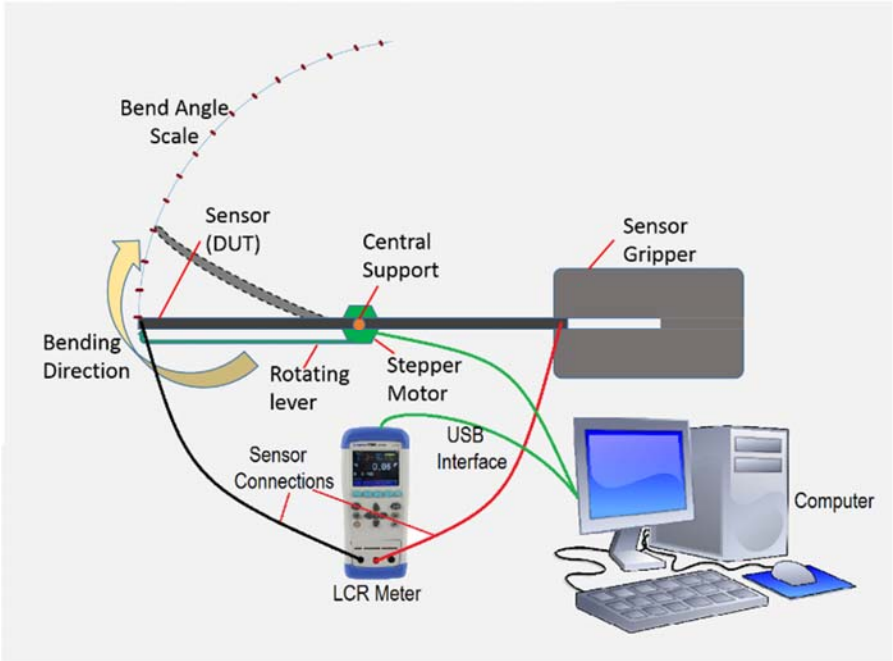

Figure 4-23: The schematic diagram of system used for sensors characterization at different bend angles with computer controlled rotation at specified angle.

The resistance of all the four sensors with micro-gravure based protective coating is plotted in ***Figure 4-24*** along with the normalized response of all types of different sensors fabricated for testing and optimization and the results of robustness testing of the protected and non-protected devices for several hundreds of bending cycles. The figure also shows the sensors mounted onto a glove to act as human posture detectors for muscle movement detection and for human machine interface (HMI) systems. The results show promising response of both the protected and un-protected sensors towards positive and negative bending. Sensors with different lengths and widths were tested for

both types and the best recorded response for protected sensors was 2.3 MΩ to 3 MΩ to 3.6 MΩ for -120º to 0º to 120º bend while for non-protected sensors was 0.25 MΩ to 0.4 MΩ to 0.55 MΩ for -120º to 0º to 120º bend. The average change in resistance for the protected sensors is ~40% reduction for a bend of -120º and ~60% increase for a bend of 120º. The protective coating of PVAc further enhances the sensor stability and durability by keeping the active carbon layer intact and preventing any damages due to wear off of material on contact.

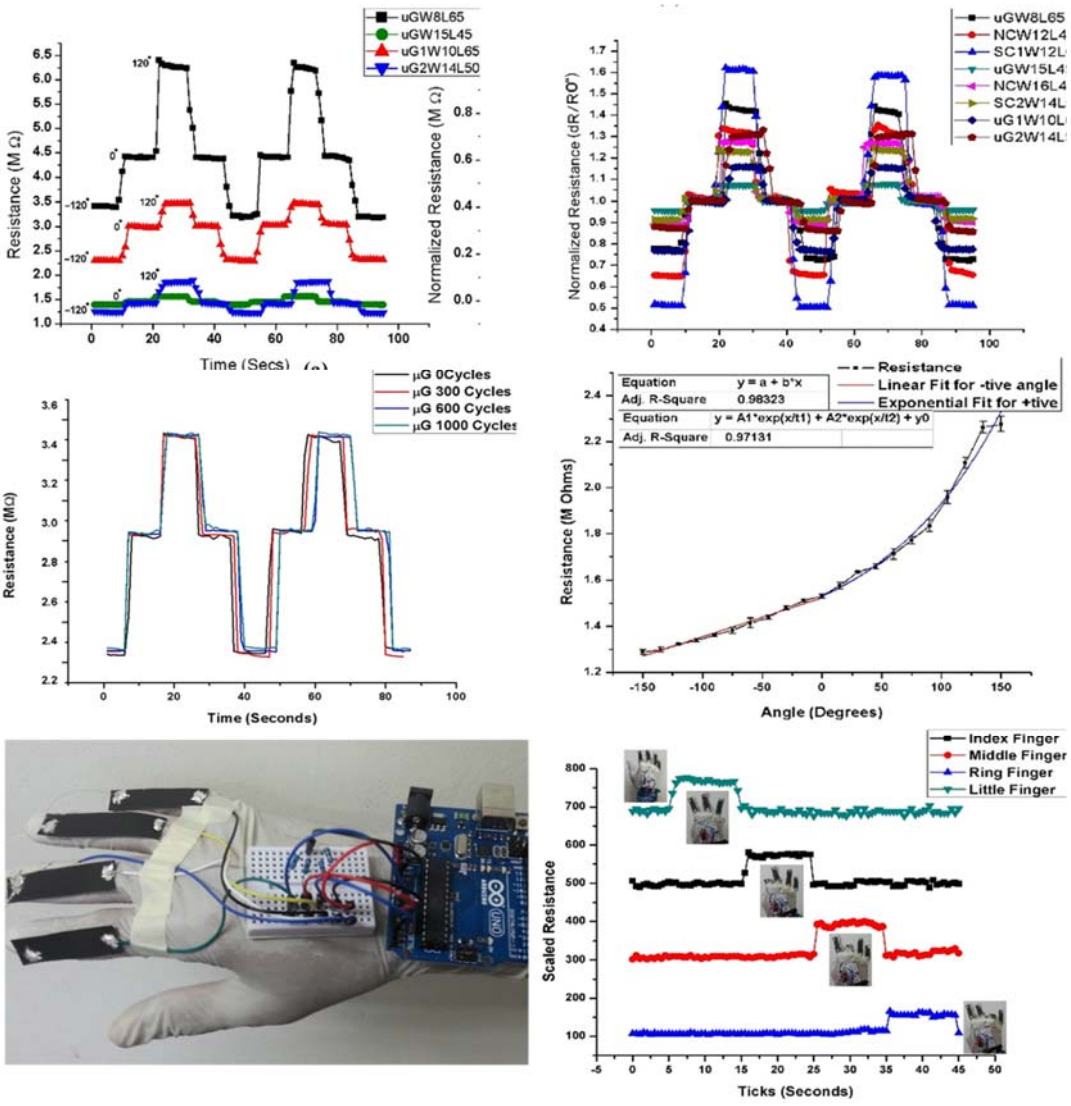

Figure 4-24: Response curves of the sensors (a) with protective coating, (b) normalized response, (c) robustness results protective coating, (d) response curve for -150° to 150° bend angles, (e) sensors mounted on glove, and (f) detection of human finger posture.

The sensors with protective coating have higher average resistance but about same percentage resistance change as compared to the non-coated ones implying lower power consumption without effecting the performance. Also, increasing the sensor width decreases the resistance and so does reducing the length. The sensors were mounted

on a glove and the results indicate stable and accurate operation.

5 Conclusions and Future Work

The target of this research work was to develop high performance sensing devices using printed electronics approaches. The targeted sensor categories include environmental and bio sensing devices. Temperature and humidity sensors were focused among a vast variety of environmental sensors while immunosensors and body posture detectors were developed under biosensors category. The aim was to improve the device sensitivity, selectivity, accuracy, robustness, limit and range of detection, transient response time, stability, and output response curve shape to allow easy interfacing for real life applications. The targets were achieved through multi-disciplinary research including materials science, printing systems and processes, and device physics and sensing mechanism. The key conclusions of the research and the possible future work can be summarized as:

1. Humidity sensors were fabricated through all printed techniques using polymers, 2D materials, and hybrid nano-composites as the sensing materials with excellent performance parameters that were at least comparable to or better than the available commercial devices and those reported in literature.
2. The best performance parameters achieved for the humidity sensing device were a sensitivity of >50 kΩ/%RH or 700 Hz/%RH, response and recovery times of 0.8 s and 1.2 s respectively, range of detection from 0% RH to 90% RH, high selectivity with no response to other gases, medium temperature dependence, high accuracy of ±2% error, low hysteresis of up to 2%, high repeatability and long term stability of up to 2%, and excellent curve linearity for seamless integration and readout.
3. A linear resistive temperature sensor was 3D printed using a commercially available conductive filament based on graphene nano-rods and PLA composite. The sensor can be embedded and printed inside the 3D printed body of any host structure or robot and is capable to record temperature with accuracy from 0ºC to 60ºC. The sensor can be used in both dry and wet conditions and even under water without any degradation or error. The response and recovery times achieved for the sensor were 6 s and 10 s respectively while the sensitivity was 12 Ω/ºC.
4. Multi-reagent immunosensors were developed aimed at point-of-care diagnosis of various diseases and conditions. Prostate specific antigen (PSA), immunoglobulin G (IgG), and NF-κB were used as the analytes. A single system was designed and developed to quantitatively detect the amount of target analyte in a given sample. The diagnosis setup was handheld and was connected to mobile phone for easy and seamless

operation by one. 2D material based active area was fabricated to immobilize the receptors and IDT based transducer was used for improving the sensitivity.

5. The performance parameters achieved for the immunosensors were comparable or better than the reported ones and lied well within the required clinical detection range. The detection limits of 0.1ng/ml, 1ng/ml, and 1ng/ml were achieved for PSA, IgG, and NF-κB respectively. The detection ranges of 1ng/ml to 800ng/ml, 10ng/ml to 9µg/ml, and 10ng/ml to 1µg/ml were achieved for PSA, IgG, and NF-κB respectively. SNR values of 10, 11, and 5 were achieved for PSA, IgG, and NF-κB respectively showing high significance of the results. The POC diagnosis setup successfully detected the test samples of different concentrations of IgG with an average error of ±5.8%.
6. A highly stable and cheap mass production compatible flex sensor was fabricated through Microgravure printing for human posture and muscle movement detection. The carbon-PVDF composite based sensors protected through PVAc coating showed high robustness for more than a thousand test cycles with no degradation at all. The average change in resistance for the protected sensors was ~40% reduction for a bend of -120º and ~60% increase for a bend of 120º. The sensors were mounted on a glove to detect the hand finger motion with high accuracy. The fabricated devices were commercialization ready.
7. The future target is to develop high performance sensors through an easy and low cost method. Application specific sensors must have certain performance parameters up to the mark while some of the other in-significant parameters can be ignored. The aim is to eliminate as many limitations as possible associated with sensors. The importance of device structure & mechanism is as vital as materials development & both aspects must be considered when designing high performance devices. Multi-disciplinary research is the key to remove limitations in this research area. The current research focuses on development of high performance active layer materials, state-of-art device fabrication process and systems, and optimized device structures and sensing mechanisms to improve the overall device performance. Multi-element transducers will also be used in different sensor categories in future.

References

1 K. H. Choi, M. Sajid, S. Aziz and B.-S. Yang, *Sensors Actuators A Phys.*, 2015, **228**, 40–49.

2 M. Sajid, S. Aziz, G. B. Kim, S. W. Kim, J. Jo and K. H. Choi, *Sci. Rep.*, , DOI:10.1038/srep30065.

3 K. H. Choi, H. B. Kim, K. Ali, M. Sajid, G. Uddin Siddiqui, D. E. Chang, H. C. Kim, J. B. Ko, H. W. Dang and Y. H. Doh, *Sci. Rep.*, 2015, **5**, 15178.

4 M. Saleem, N. Ahmed, M. M. Tahir, M. S. Zahid, M. Sajid, M. M. Bashir and W. Road, 2016, **17**, 84–89.

5 E. Sauerbrunn, Y. Chen, J. Didion, M. Yu, E. Smela and H. A. Bruck, *Phys. Status Solidi*, 2015, **212**, 2239–2245.

6 P. Van Gerwen, *Sensors Actuators B Chem.*, 1998, **49**, 73–80.

7 D. Duan, *Biosens. Bioelectron.*, 2015, **74**, 134–141.

8 D. Nidzworski, *Biosens. Bioelectron.*, 2014, **59**, 239–242.

9 Andreescu, *Pure Appl. Chem*, 2004, **76**, 861–878.

10 K. Shavanova, *Sensors (Switzerland)*, 2016, **16**, 1–23.

11 S. Varghese, *Electronics*, 2015, **4**, 651–687.

12 M. Sajid, H. B. Kim, Y. J. Yang, J. Jo and K. H. Choi, *Sensors Actuators B Chem.*, 2017, **246**, 809–818.

13 H. B. Kim, M. Sajid, K. T. Kim, K. H. Na and K. H. Choi, *Sensors Actuators B*, 2017, **252**, 725–734.

14 F. Zhang, Y. Zang, D. Huang, C. Di and D. Zhu, *Nat. Commun.*, 2015, **6**, 8356.

15 M. Sajid, A. Osman, G. U. Siddiqui, H. B. Kim, S. W. Kim, J. B. Ko, Y. K. Lim and K. H. Choi, , DOI:10.1038/s41598-017-06265-1.

16 J. Yang and D. et. al. Wei, *RSC Adv.*, 2015, **5**, 25609–25615.

17 Kenry, J. C. Yeo and C. T. Lim, *Microsystems Nanoeng.*, 2016, **2**, 16043.

18 N. Neella and V. Gaddam, 2016, 17–20.

19 N. A. Travlou, M. Seredych, E. Rodríguez-Castellón and T. J. Bandosz, *J. Mater. Chem. A*, 2015, **3**, 3821–3831.

20 L. Chi-Yuan, L. Chien-Hen and L. Yi-Man, *Sensors*, 2011, **11**, 3706–3716.

21 H. Bai and G. Shi, *Sensors*, 2007, **7**, 267–307.

22 C. Yu and H. Jiang, *Thin Solid Films*, 2010, **519**, 818–822.

23 K.-P. Yoo, L.-T. Lim, N.-K. Min, M. J. Lee, C. J. Lee and C.-W. Park, *Sensors Actuators B Chem.*, 2010, **145**, 120–125.

24 S. K. Mahadeva, S. Yun and J. Kim, *Sensors Actuators A Phys.*, 2011, **165**, 194–199.

25 E. Espinosa, R. Ionescu, S. Zampolli, I. Elmi, G. C. Cardinali, E. Abad, R. Leghrib, J. L. Ramírez, X. Vilanova and E. Llobet, *Sensors Actuators B Chem.*, 2010, **144**, 462–466.

26 X. Gong, M. Tong, Y. Xia, W. Cai, J. S. Moon, Y. Cao, G. Yu, C.-L. Shieh, B. Nilsson and A. J. Heeger, *Science (80-.).*, 2009, **325**, 1665–1667.

27 et. al Kata J., Chakrit S, A. Sappat, in *ECTI-CON*, Thailand, 2011, pp. 66–69.

28 Y. Zhang, K. Yu, D. Jiang, Z. Zhu, H. Geng and L. Luo, *Appl. Surf. Sci.*, 2005, **242**, 212–217.

29 M. Anbia and S. E. M. Fard, *J. Rare Earths*, 2012, **30**, 38–42.

30 B. X. C. Dongzhi Zhang , Jun Tong, *Sensors Actuators B. Chem.*, , DOI:10.1016/j.snb.2014.02.078.

31 M. Hoummady, A. Campitelli and W. Wlodarski, *Smart Mater. Struct.*, 1997, **6**, 647–657.

32 A. Buvailo, Y. Xing, J. Hines and E. Borguet, *Sensors Actuators B Chem.*, 2011, **156**, 444–449.

33 Y. X. Weipeng Xuan1, Xingli He1, Jinkai Chen1, Wenbo Wang1, Xiaozhi Wang1* and Y. Q. F. and J. K. L. Zhen Xu2, *Nanoscale*, , DOI:10.1039/C5NR00040H.

34 Z. Ahmad, Q. Zafar, K. Sulaiman, R. Akram and K. S. Karimov, *Sensors (Switzerland)*, 2013, **13**, 3615–3624.

35 Y. D. Park, B. Kang, H. S. Lim, K. Cho, M. S. Kang and J. H. Cho, .

36 M. Saleem, N. Ahmed, M. M. Tahir, M. S. Zahid, M. Sajid, M. M. Bashir, W. Road, K. Karimov, M. Saleem, N. Ahmed, M. M. Tahir, M. S. Zahid, M. Sajid and M. M. Bashir, *PROCEEDINGS*, 2016, **17**, 84–89.

37 D. P. Pradeep, E.K.C. , Herath, H. M. P. C. K. , Perera, H. R. , Ll, C. Y. , Dissnayake, in *4th International Symposium of Frontier Technology, At Shenyang Pharmaceutical University, Shenyang, China*, 2013, pp. 1–4.

38 Y. Yao, X. Chen, H. Guo, Z. Wu and X. Li, *Sensors Actuators B Chem.*, 2012, **161**, 1053–1058.

39 S. T. Mcgovern, G. M. Spinks and G. G. Wallace, *Sensors Actuators B Chem.*, 2005, **107**, 657–665.

40 Z. M. Rittersma, 2002, **96**, 196–210.

41 Y. Zhang, R. Liu, J. Liu, Z. Li and X. Liu, *RSC Adv.*, , DOI:10.1039/C6RA03050E.

42 K. Jiang, H. Zhao, J. Dai, D. Kuang, T. Fei and T. Zhang, *ACS Appl. Mater. Interfaces*, 2016, **8**, 25529–25534.

43 G. Campo, C. Sangregorio, B. Mazzolai and V. Mattoli, *Appl. Mater. Interfaces*, , DOI:10.1021/am4013775.

44 T. Zhang, R. Wang, W. Geng, X. Li, Q. Qi, Y. He and S. Wang, 2008, **128**, 482–487.

45 S. Griesel, M. Theel, H. Niemand and E. Lanzinger, in *WMO CIMO TECO-2012, Brussels, Belgium*, Brussels, 2012, pp. 1–7.

46 G. Li, J. Ma, G. Peng, W. Chen, Z. Chu, Y. Li, T. Hu and X. Li, , DOI:10.1021/am5067496.

47 C. Y. Chao and L. J. Guo, *Appl. Phys. Lett.*, 2003, **83**, 1527–1529.

48 A. I. Barbosa, P. Gehlot, K. Sidapra, A. D. Edwards and N. M. Reis, *Biosens. Bioelectron.*, 2015, **70**, 5–14.

49 D. Quesada-González and A. Merkoçi, *Biosens. Bioelectron.*, 2015, **73**, 47–63.

50 C. C. Seepersad, *3D Print. Addit. Manuf.*, 2014, **1**, 10–13.

51 B. Khoda, 2014, **1**, 210–218.

52 Y. Xu, X. Wu, X. Guo, B. Kong, M. Zhang, X. Qian, S. Mi and W. Sun, *The Boom in 3D-Printed Sensor Technology*, 2017, vol. 17.

53 X. Wei, D. Li, W. Jiang, Z. Gu, X. Wang, Z. Zhang and Z. Sun, *Sci. Rep.*, 2015, **5**, 11181.

54 K. Gnanasekaran, T. Heijmans, S. van Bennekom, H. Woldhuis, S. Wijnia, G. de With and H. Friedrich, *Appl. Mater. Today*, 2017, **9**, 21–28.

55 J. Ou, G. Dublon, C. Cheng, F. Heibeck, K. Willis and H. Ishii, *Proc. 2016 CHI Conf. Hum. Factors Comput. Syst.*, 2016, 5753–5764.

56 M. Saari, B. Xia, B. Cox, P. S. Krueger, A. L. Cohen and E. Richer, *3D Print. Addit. Manuf.*, 2016, **3**, 137–141.

57 M. Sajid, G. U. Siddiqui, S. W. Kim, K. H. Na, Y. S. Choi and K. H. Choi, *Sensors Actuators, A Phys.*, , DOI:10.1016/j.sna.2017.08.040.

58 D. Zhang, Y. Sun, P. Li and Y. Zhang, , DOI:10.1021/acsami.6b02206.

59 J. Lee, *Sci. Rep.*, 2014, **4**, 7352.

60 W. Zhang, P. Zhang, Z. Su and G. Wei, *Nanoscale*, 2015, **7**, 18364–78.

61 H. Nam, *Sci. Rep.*, 2015, **5**, 10546.

62 O. Lopez-Sanchez, *Master Thesis*.

63 M. Naguib, V. N. Mochalin, M. W. Barsoum and Y. Gogotsi, *Adv. Mater.*, 2014, **26**, 992–1005.

64 H. Liu, C. Duan, C. Yang, W. Shen, F. Wang and Z. Zhu, *Sensors Actuators B Chem.*, 2015, **218**, 60–66.

65 F. Wang, C. Yang, C. Duan, D. Xiao, Y. Tang and J. Zhu, *J. Electrochem. Soc.*, 2014, **162**, B16–B21.

66 X. Yu, Y. Li, J. Cheng, Z. Liu, Q. Li, W. Li, X. Yang and B. Xiao, *ACS Appl. Mater. Interfaces*, 2015, **7**, 13707–13713.

67 J. L. and E. W. Qingfeng Zhaiab, Xiaowei Zhangab, *Nanoscale*, , DOI:10.1039/C6NR03608B.

68 a H. J. a * Yuan-Ying Wang, a Li-Li Ling and Catalytic, *Green Chem.*, , DOI:10.1039/C6GC00247A.

69 Z. W. Seh, K. D. Fredrickson, B. Anasori, J. Kibsgaard, A. L. Strickler, M. R. Lukatskaya, Y. Gogotsi, T. F. Jaramillo and A. Vojvodic, , DOI:10.1021/acsenergylett.6b00247.

70 J. Choi, V. Schwartz, E. Santillan-jimenez and M. Crocker, 2015, 406–423.

71 C. Xu, L. Wang, Z. Liu, L. Chen, J. Guo, N. Kang, X. Ma, H. Cheng and W. Ren, *Nat. Mater*, 2015, 1–8.

72 C. Pistonesi and A. Juan, .

73 J. Halim, S. Kota, M. R. Lukatskaya, M. Naguib, M.-Q. Zhao, E. J. Moon, J. Pitock, J. Nanda, S. J. May, Y. Gogotsi and M. W. Barsoum, *Adv. Funct. Mater.*, 2016, **26**, 3118–3127.

74 L. Huo, B. Liu, G. Zhang and J. Zhang, *ACS Appl. Mater. Interfaces*, 2016, **8**, 18107–18118.

75 C. A. Wolden, A. Pickerell, T. Gawai, S. Parks, J. Hensley and J. D. Way, *ACS Appl. Mater. Interfaces*, 2011, **3**, 517–521.

76 K. J. Sankaran, D. Q. Hoang, S. Kunuku, S. Korneychuk, S. Turner, P. Pobedinskas, S. Drijkoningen, M. K. Van Bael, J. D' Haen, J. Verbeeck, K.-C. Leou, I.-N. Lin and K. Haenen, *Sci. Rep.*, 2016, **6**, 29444.

77 X. Wang, Y. Xie and Q. Guo, *Chem. Commun.*, 2003, 2688.

78 A. Hidalgo, V. Makarov, G. Morell and B. R. Weiner, *Dataset Pap. Nanotechnol.*, 2012, **2013**, 1–5.

79 M. Sajid, A. Osman, G. U. Siddiqui, H. B. Kim, S. W. Kim, J. B. Ko, Y. K. Lim and K. H. Choi, .

80 H. B. Kim, M. Sajid, K. T. Kim, K. H. Na and K. H. Choi, *Sensors Actuators, B Chem.*, , DOI:10.1016/j.snb.2017.06.052.

81 M. Sajid, H. B. Kim, G. U. Siddiqui, K. H. Na and K. H. Choi, *Sensors Actuators A*, 2017, **262**, 68–77.

82 M. Sajid, H. B. Kim, G. U. Siddiqui, K. H. Na and K.-H. Choi, *Sensors Actuators A Phys.*, 2017, **262**, 68–77.

83 C. Wan, Y. N. Regmi and B. M. Leonard, 2014, 1–5.

84 S. Posada-pérez, F. Viñes, R. Valero, J. A. Rodriguez and F. Illas, *Surf. Sci.*, 2017, **656**, 24–32.

85 a J. A. R. and F. I. Jose ´ Roberto dos Santos Politi,ab Francesc Vin ˜es, *Phys.Chem.Chem.Phys*, 2013, **15**, 12617–12625.

86 S. Posada-P´, b F. V. nes*a erez, a Jos´ e Roberto dos Santos Politi and and F. Illasa, *RSC Adv.*, 2015, 33737–33746.

87 S. US2081, .

88 A. G. F. Padial, C. A. Cunha, O. V. Correa, N. B. de Lima and L. V. Ramanathan, *Mater. Sci. Forum*, 2010, **660**–

661, 379–384.

89 Y. Li, Y. Gao, B. Xiao, T. Min, Y. Yang, S. Ma and D. Yi, *J. Alloys Compd.*, 2011, **509**, 5242–5249.

90 F. Wang, 2015, **162**, 16–21.

91 S. Choi and J. Chae, *J. Micromechanics Microengineering*, 2010, **20**, 75015.

92 M. M. Rehman, G. U. Siddiqui, J. Z. Gul, S. Kim, J. H. Lim and K. H. Choi, *Sci. Rep.*, 2016, **6**, 36195.

93 J. Ali, G. Uddin, K. Hyun, Y. Jang and K. Lee, *J. Lumin.*, 2016, **169**, 342–347.

94 M. Sajid, A. Osman, G. U. Siddiqui, H. B. Kim, S. W. Kim, J. B. Ko, Y. K. Lim and K. H. Choi, *Sci. Rep.*, 2017, **7**, 5802.

95 E. Sheha, M. Nasr and M. K. El-Mansy, *Phys. Scr.*, 2013, **88**, 35701.

96 Z. Shalabutov, M. Friedrich, I. Thurzo, A. C. Huebler, D. R. T. Zahn and U. Hahn, *Arxiv Prepr. cond-mat/0411372*.

97 C.-W. Liew, H. M. Ng, A. Numan and S. Ramesh, *Polymers (Basel).*, 2016, **8**, 179.

98 A. Maira, J. Coronado, V. Augugliaro, K. . Yeung, J. . Conesa and J. Soria, *J. Catal.*, 2001, **202**, 413–420.

99 G. U. Siddiqui, M. M. Rehman, Y. Yang and K. H. Choi, *J. Mater. Chem. C*, 2017, **5**, 862–871.

100 M. Sajid, H. W. Dang, K.-H. Na and K. H. Choi, *Sensors Actuators, A Phys.*, , DOI:10.1016/j.sna.2015.10.037.

101 J. Lin, Z. Peng, C. Xiang, G. Ruan, Z. Yan, D. Natelson and J. M. Tour, *ACS Nano*, 2013, **7**, 6001–6006.

102 R. Pawlak, M. Lebioda, J. Rymaszewski, W. Szymanski, L. Kolodziejczyk and P. Kula, *Sensors (Switzerland)*, , DOI:10.3390/s17010051.

103 J. Yang and L. et. al. Tang, *RSC Adv.*, 2015, **5**, 25609–25615.

104 T. S. Sreeprasad, A. A. Rodriguez, J. Colston, A. Graham, E. Shishkin, V. Pallem and V. Berry, .

105 A. R. O. Raji, S. Salters, E. L. G. Samuel, Y. Zhu, V. Volman and J. M. Tour, *ACS Appl. Mater. Interfaces*, 2014, **6**, 16661–16668.

106 C. H. An Wong and M. Pumera, *J. Mater. Chem. C*, 2014, **2**, 856–863.

107 A. M. Dimiev and J. M. Tour, 2017, **10**, 1–8.

108 M. A. Cuiffo, J. Snyder, A. M. Elliott, N. Romero, S. Kannan and G. P. Halada, *Appl. Sci.*, 2017, **7**, 579.

109 C.-C. Qin, X.-P. Duan, L. Wang, L.-H. Zhang, M. Yu, R.-H. Dong, X. Yan, H.-W. He and Y.-Z. Long, *Nanoscale*, 2015, **7**, 16611–16615.

110 I. L. Liakos, A. M. Grumezescu, A. M. Holban, I. Florin, F. D'Autilia, R. Carzino, P. Bianchini and A. Athanassiou, *Pharmaceuticals*, , DOI:10.3390/ph9030042.

111 M. M. Nobrega, J. B. Olivato, C. M. O. Mueller and F. Yamashita, *Polim. E Tecnol.*, 2012, **22**, 475–480.

112 L. Wang, Y. Wang, J. I. Wong, T. Palacios, J. Kong and H. Y. Yang, *Small*, 2014, **10**, 1101–1105.

113 J. H. Chua, R. E. Chee, A. Agarwal, M. W. She and G. J. Zhang, *Anal. Chem.*, 2009, **81**, 6266–6271.

114 F. Patolsky, G. Zheng and C. M. Lieber, *Nat. Protoc.*, 2006, **1**, 1711–1724.

115 A. Kim, C. S. Ah, H. Y. Yu, J. H. Yang, I. B. Baek, C. G. Ahn, C. W. Park, M. S. Jun and S. Lee, *Appl. Phys. Lett.*, 2007, **91**, 11–14.

116 G. Zheng, F. Patolsky, Y. Cui, W. U. Wang and C. M. Lieber, *Nat. Biotechnol.*, 2005, **23**, 1294–1301.

117 M. C. Lin, C. J. Chu, L. C. Tsai, H. Y. Lin, C. S. Wu, Y. P. Wu, Y. N. Wu, D. B. Shieh, Y. W. Su and C. D. Chen, *Nano Lett.*, 2007, **7**, 3656–3661.

118 K. Kalantar-zadeh and J. Z. Ou, *ACS Sensors*, 2016, **1**, 5–16.

119 X. Yu, M. S. Pr??vot and K. Sivula, *Chem. Mater.*, 2014, **26**, 5892–5899.

120 J. Liu, Y. Li, J. Ke, Z. Wang and H. Xiao, *Catalysts*, 2017, **7**, 30.

121 X. Zeng, L. Niu, L. Song, X. Wang, X. Shi and J. Yan, *Metals (Basel).*, 2015, **5**, 1829–1844.

122 C. Shahar, D. Zbaida, L. Rapoport, H. Cohen, T. Bendikov, J. Tannous, F. Dassenoy and R. Tenne, *Langmuir*, 2010, **26**, 4409–4414.

123 D. Sarkar, W. Liu, X. Xie, A. C. Anselmo, S. Mitragotri and K. Banerjee, *ACS Nano*, 2014, **8**, 3992–4003.

124 H. D. Dhruv, Utah State University.

125 M. Sajid, S. Aziz, G. B. Kim, S. W. Kim, J. Jo and K. H. Choi, *Sci. Rep.*, 2016, **6**, 30065.

126 M. Sajid, M. Zubair, Y. H. Doh, K.-H. Na and K. H. Choi, *J. Mater. Sci. Mater. Electron.*, 2015, **26**, 7192–7199.

127 T. H. E. Y. Seiki, C. Method, I. Drive and W. Site, .

128 A. Sun, L. Huang and Y. Li, *Sensors Actuators, B Chem.*, 2009, **139**, 543–547.

129 S. Aziz, D. E. Chang, Y. H. Doh, C. U. Kang and K. H. Choi, *J. Electron. Mater.*, 2015, **44**, 3992–3999.

130 S. Aziz, K. G. Bum, Y. J. Yang, B.-S. Yang, C. U. Kang, Y. H. Doh, K. H. Choi and H. C. Kim, *Sensors Actuators A Phys.*, 2016, **246**, 1–8.

131 W. Xuan, M. He, N. Meng, X. He, W. Wang, J. Chen, T. Shi, T. Hasan, Z. Xu, Y. Xu and J. K. Luo, *Sci. Rep.*, 2014, **4**, 7206.

132 M. Yang and K. Chen, 1998, **49**, 240–247.

133 H. Bi, K. Yin, X. Xie, J. Ji, S. Wan, L. Sun and M. Terrones, 2013, 1–7.

134 D. Elektrotechnzk, 1987, **11**, 329–337.

135 M. Kuş and S. Okur, *Sensors Actuators B Chem.*, 2009, **143**, 177–181.

136 Z. Chen and C. Lu, *Sens. Lett.*, 2005, **3**, 274–295.

137 H. Bai and G. Shi, *Sensors (Basel).*, 2007, **7**, 267–307.

138 K. Jiang, T. Fei, F. Jiang, G. Wang and T. Zhang, *Sensors Actuators B Chem.*, 2014, **192**, 658–663.

139 A. C. Power, A. J. Betts and J. F. Cassidy, *Analyst*, 2010, **135**, 1645.

140 J. Li, J. Liu, C. Gao, J. Zhang and H. Sun, *Int. J. Photoenergy*, 2009, **2009**, 1–5.

141 A. Sappat, A. Wisitsoraat, C. Sriprachuabwong, K. Jaruwongrungsee, T. Lomas and A. Tuantranont, in *ECTI-CON 2011 - 8th Electrical Engineering/ Electronics, Computer, Telecommunications and Information Technology (ECTI) Association of Thailand - Conference 2011*, IEEE, 2011, pp. 34–37.

142 U. Mogera, A. a Sagade, S. J. George and G. U. Kulkarni, *Sci. Rep.*, 2015, **4**, 4103.

143 W. Geng, X. He, Y. Su, J. Dang, J. Gu, W. Tian and Q. Zhang, *Sensors Actuators, B Chem.*, 2016, **226**, 471–477.

144 K. S. Karimov, M. Saleem, N. Ahmed, M. M. Tahir, M. S. Zahid, M. Sajid and M. M. Bashir, *Proc. Rom. Acad. Ser. A - Math. Phys. Tech. Sci. Inf. Sci.*, 2016, **17**, 84–89.

145 C. M. Gerard and E. Al., *Sensors & Transducers*, 2009, **110**, 105–111.

146 G. Zhou, J. Byun, Y. Oh and B. Jung, , DOI:10.1021/acsami.6b12448.

147 M. Yang, C. Dai and W. Lin, 2011, 8143–8151.

148 S. K. Shukla, A. Bharadavaja, A. Shekhar and A. Tiwari, 2012, **3**, 421–425.

149 R. Nohria, R. K. Khillan, Y. Su, R. Dikshit, Y. Lvov and K. Varahramyan, *Sensors Actuators B Chem.*, 2006, **114**, 218–222.

150 K. Ogura, T. Tonosaki and H. Shiigi, , DOI:10.1149/1.1350690.

151 Y. Li, L. Hong, Y. Chen, H. Wang, X. Lu and M. Yang, *Sensors Actuators B Chem.*, 2007, **123**, 554–559.

152 M. Yang, Y. Li, X. Zhan and M. Ling, *J. Appl. Polym. Sci.*, 1999, **74**, 2010–2015.

153 M. T. S. Chani, K. S. Karimov, F. A. Khalid and S. A. Moiz, *Solid State Sci.*, 2013, **18**, 78–82.

154 Y. Li, K. Fan, H. Ban and M. Yang, *Sensors Actuators B Chem.*, 2016, **222**, 151–158.

155 Y. Li and M. . Yang, *Sensors Actuators B Chem.*, 2002, **87**, 184–189.

156 Z. Ahmad, M. H. Sayyad and K. S. Karimov, *J. Ovonic Res.*, 2008, **4**, 91–95.

157 H. Huang, A. Sun, C. Chu, Y. Li and G. Xu, *Integr. Ferroelectr.*, 2013, **144**, 127–134.

158 E. Ghafar-Zadeh and M. Sawan, *CMOS Capacitive Sensors for Lab-on-Chip Applications*, Springer Netherlands, Dordrecht, 2010.

159 A. Tripathy, S. Pramanik, A. Manna, S. Bhuyan, N. Azrin Shah, Z. Radzi and N. Abu Osman, *Sensors*, 2016, **16**, 1135.

160 Z. Li, L. Zhang, B. S. Amirkhiz, X. Tan, Z. Xu, H. Wang, B. C. Olsen, C. M. B. Holt and D. Mitlin, *Adv. Energy Mater.*, 2012, **2**, 431–437.

161 C. C. Chen, W. P. Shih, P. Z. Chang, H. M. Lai, S. Y. Chang, P. C. Huang and H. A. Jeng, *Appl. Phys. Lett.*, , DOI:10.1063/1.4917498.

162 D. Bagal-Kestwal, R. M. Kestwal and B.-H. Chiang, *J. Nanobiotechnology*, 2015, **13**, 13–30.

163 K.-I. Jang and H. et. al Chung, *Nat. Commun.*, 2015, **6**, 6566.

164 G. a Salvatore, N. Münzenrieder, T. Kinkeldei, L. Petti, C. Zysset, I. Strebel, L. Büthe and G. Tröster, *Nat. Commun.*, 2014, **5**, 2982.

165 V. Linder, B. D. Gates, D. Ryan, B. a Parviz and G. M. Whitesides, *Small*, 2005, **1**, 730–6.

166 Y. Zhou, L. Hu and G. Grüner, *Appl. Phys. Lett.*, 2006, **88**, 14–17.

167 J. Song, F.-Y. Kam, R.-Q. Png, W.-L. Seah, J.-M. Zhuo, G.-K. Lim, P. K. H. Ho and L.-L. Chua, *Nat. Nanotechnol.*, 2013, **8**, 356–62.

168 J. Jeong, J. Kim, K. Song, K. Autumn and J. Lee, *J. R. Soc. Interface*, 2014, **11**, 20140627.

169 Y. Zhang, J. J. Magan and W. J. Blau, *Sci. Rep.*, 2014, **4**, 4822.

170 W. Deng, X. Zhang, H. Pan, Q. Shang, J. Wang, X. Zhang, X. Zhang and J. Jie, *Sci. Rep.*, 2014, **4**, 5358.

171 C. H. Lee, D. R. Kim and X. Zheng, *Proc. Natl. Acad. Sci. U. S. A.*, 2010, **107**, 9950–5.

172 C. H. Lee, D. R. Kim and X. Zheng, *Nano Lett.*, 2011, **11**, 3435–9.

173 A. Assani, S. Moundanga, L. Beney and P. Gervais, *Ann. Bot.*, 2009, **104**, 1389–1395.

174 M. V Kulkarni, S. K. Apte, S. D. Naik, J. D. Ambekar and B. B. Kale, *Sensors Actuators B Chem.*, 2013, **178**, 140–143.

175 S. Borini, R. White, D. Wei, M. Astley, S. Haque, E. Spigone, N. Harris, J. Kivioja and T. Ryhänen, *ACS Nano*, 2013, **7**, 11166–11173.

176 X. Dong, T. Li, Y. Liu, Y. Li, C.-L. Zhao and C. C. Chan, *J. Biomed. Opt.*, 2011, **16**, 77001.

177 P. Karthick, R. Saraswathi, J. Bosco and B. Rayappan, *Sensors Actuators A. Phys.*, 2010, **164**, 8–14.

178 Y.-C. Hu, C.-L. Dai and C.-C. Hsu, *Sensors*, 2014, **14**, 4177–4188.

179 Meng-Chu Chen, Cheng-Liang Hsu and Ting-Jen Hsueh, *IEEE Electron Device Lett.*, 2014, **35**, 590–592.

180 I. Ferroelectrics and I. Tech, , DOI:10.1080/10584587.2013.787828.

181 Y. Li, K. Fan, H. Ban and M. Yang, *Sensors Actuators B. Chem.*, 2016, **222**, 151–158.

182 K. Wang, X. Qian, L. Zhang, Y. Li and H. Liu, .

183 H. Yu, H. K. Kim, T. Kim, K. M. Bae, S. M. Seo, J.-M. Kim, T. J. Kang and Y. H. Kim, *ACS Appl. Mater. Interfaces*, 2014, **6**, 8320–8326.

184 K. Jiang, H. Zhao, J. Dai, T. Fei and T. Zhang, , DOI:10.1021/acsami.6b08071.

185 R. Earths, , DOI:10.1016/S1002-0721(10)60635-7.

186 A. I. Buvailo, Y. Xing, J. Hines, N. Dollahon and E. Borguet, 2011, 528–533.

187 H. Liu, W. Sun and S. Xu, *Adv. Mater.*, 2012, **24**, 3275–3279.

188 X. Huo, Z. Wang, M. Fu, J. Xia and S. Xu, *RSC Adv.*, 2016, **6**, 40185–40191.

189 S. Sahoo, S. K. S. Parashar and S. M. Ali, 2014, **3**, 117–124.

190 R. Strümpler and R. Stru, , DOI:10.1063/1.363682.

191 K. H. Choi, M. Zubair and H. W. Dang, **2**, 3–8.

192 S. Harada, W. Honda, T. Arie, S. Akita and K. Takei, *ACS Nano*, 2014, **8**, 3921–3927.

193 F. Xue, L. Zhang, W. Tang, C. Zhang, W. Du and Z. L. Wang, *ACS Appl Mater Inter*, 2014, **6**, 5955–61.

194 M. Taghipoor, A. Bertsch and P. Renaud, *ACS Nano*, 2015, **9**, 4563–4571.

195 Y. M. Banadaki, K. M. Mohsin and A. Srivastava, *Proc. SPIE - Int. Soc. Opt. Eng.*, 2014, **9060**, 90600F.

196 X. Ren, P. K. L. Chan, J. Lu, B. Huang and D. C. W. Leung, *Adv. Mater.*, 2013, **25**, 1291–1295.

197 S. Micro, N. P. Nanogenerators and S. T. Sensors, 2012, 8456–8461.

198 C. Yan, J. Wang and P. S. Lee, *ACS Nano*, 2015, **9**, 2130–2137.

199 S.-Y. Wu, C. Yang, W. Hsu and L. Lin, *Microsystems Nanoeng.*, 2015, **1**, 15013.

200 E. García-T̂On, S. Barg, J. Franco, R. Bell, S. Eslava, E. D'Elia, R. C. Maher, F. Guitian and E. Saiz, *Adv. Mater.*, 2015, **27**, 1688–1693.

201 S. Guo, X. Yang, M.-C. Heuzey and D. Therriault, *Nanoscale*, 2015, **7**, 6451–6456.

202 M. Jamshidian, E. A. Tehrany, M. Imran, M. Jacquot and S. Desobry, *Compr. Rev. Food Sci. Food Saf.*, 2010, **9**, 552–571.

203 V. S. Giita Silverajah, N. A. Ibrahim, N. Zainuddin, W. M. Z. Wan Yunus and H. A. Hassan, *Molecules*, 2012, **17**, 11729–11747.

204 C.-Y. Lee, A. Su, Y.-C. Liu, P.-C. Chan and C.-H. Lin, *Sensors (Basel).*, 2010, **10**, 3363–72.

205 H.-S. Chuang and S. Wereley, *J. Micromechanics Microengineering*, 2009, **19**, 45010.

206 M. D. Dankoco, G. Y. Tesfay, E. Benevent and M. Bendahan, *Mater. Sci. Eng. B*, 2016, **205**, 1–5.

207 D. Kong, L. T. Le, Y. Li, J. L. Zunino and W. Lee, *Langmuir*, 2012, 1–6.

208 Y. M. Banadaki, K. M. Mohsin and A. Srivastava, *Proc. SPIE - Int. Soc. Opt. Eng.*, 2014, **9060**, 90600F.

209 T. Vuorinen, J. Niittynen, T. Kankkunen, T. M. Kraft and M. Mäntysalo, *Sci. Rep.*, 2016, **6**, 35289.

210 T. Kose, K. Azgin and T. Akin, *J. Micromechanics Microengineering*, 2016, **26**, 45012.

211 S. Ali, A. Hassan, J. Bae, C. H. Lee and J. Kim, *Langmuir*, 2016, **32**, 11432–11439.

212 Z. Pan, Y. Zhang, Z. Cheng, J. Tong, Q. Chen, J. Zhang, J. Zhang, X. Li and Y. Li, *Sensors*, 2017, **17**, 473.

213 G. Y. Carlos Moina, *Adv. Immunoass. Technol.*, 111.

214 P. B. Luppa, *Clin. Chim. Acta*, 2001, **314**, 1–26.

215 C. Zhu, *Anal. Chem.*, , DOI:10.1021/ac5039863 (2014).

216 Daniels, *Electroanalysis*, 2007, **19**, 1239–1257.

217 S. Kumar, *Biosens. Bioelectron.*, 2015, **73**, 114–122.

218 Y. Liu, Y. Xie and C. Feng, in *5th International Conference on Bioinformatics and Biomedical Engineering, iCBBE 2011*, pp. 4–7.

219 M. K. Sharma, *J. Clin. Microbiol.*, 1–8.

220 C. S. Lee, D. Kwon, J. E. Yoo, B. G. Lee, J. Choi and B. H. Chung, *Sensors*, 2010, **10**, 5160–5170.

221 M. S. Mannoor, *Nat. Commun.*, 2012, **3**, 763–768.

222 T. Cramer, *J. Mater. Chem. B*, 2013, **1**, 3728–3741.

223 D. Sarkar, *ACS Nano*, 2014, **8**, 3992–4003.

224 Q. H. Wang, *Nat. Nanotechnol.*, 2012, **7**, 699–712.

225 H. Nam, *J. Vac. Sci. Technol. B, Nanotechnol. Microelectron. Mater. Process. Meas. Phenom.*, 2015, **33**, 06FG01.

226 H. Li, Z. Yin, Q. He, H. Li, X. Huang, G. Lu, D. W. H. Fam, A. I. Y. Tok, Q. Zhang and H. Zhang, *Small*, 2012, **8**, 63–67.

227 F. K. Perkins, A. L. Friedman, E. Cobas, P. M. Campbell, G. G. Jernigan and B. T. Jonker, .

228 A. N. Sekretaryova, *Biotechnol. Adv.*, 2015, **34**, 177–197.

229 B. Kavosi, *Biosens. Bioelectron.*, 2015, **74**, 915–923.

230 D. Wu, Y. Liu, Y. Wang, L. Hu, H. Ma, G. Wang and Q. Wei, *Sci. Rep.*, 2016, **6**, 20511.

231 Y. Wang, *Thesis SIMON FRASER Univ.*

232 S. Loeb and W. J. Catalona, *Ther. Adv. Urol.*, 2014, **6**, 74–7.

233 S. Azzouzi, H. K. Patra, M. Ben, M. Nooredeen, C. Dridi, A. Errachid and A. P. F. Turner, *Sensors Actuators B. Chem.*, 2016, **228**, 335–346.

234 A. Gonzalez-Quintela, *Clin. Exp. Immunol.*, 2008, **151**, 42–50.

235 J. Wang, *ECS Trans.*, 2007, **2**, 1–7.

236 R. Das, *RSC Adv.*, 2015, **5**, 48147–48153.

237 A. Aziz and H. Yang, 2007, **28**, 1171–1174.

238 Y. Wu, *Biosens. Bioelectron.*, 2009, **24**, 1389–1393.

239 and A. Y. W. Hengyi Y. Xu, Zoraida P. Aguilar, *ECS Trans.*, 2010, **25**, 1–8.

240 T. Minamiki, T. Minami, R. Kurita, O. Niwa, S. I. Wakida, K. Fukuda, D. Kumaki and S. Tokito, *Materials (Basel).*, 2014, **6**, 6843–6852.

241 F. Baldini, L. Citti, C. Domenici, A. Giannetti, L. Tedeschi, M. B. Wabuyele, O. R. National and O. Ridge, *DNA Seq.*, 2008, **5855**, 439–442.

242 A. Oeckinghaus and S. Ghosh, *Cold Spring Harb. Perspect. Biol.*, 2009, 1, 1–14.

243 Q. Shen, C. Chitchumroonchokchai, J. L. Thomas, L. V. Gushchina, D. Disilvestro, M. L. Failla and O. Ziouzenkova, *Mol. Nutr. Food Res.*, 2014, **58**, 239–247.

244 C. D. Chin, *Low-Cost Microdevices for Point-of-Care Testing*, .

245 P. Kumar, J. Verma and S. Prasad, *Int. J. Adv. Sci. Technol.*, 2012, **43**, 15–26.

246 N. H. Adnan, K. Wan, S. Ab, S. Khadijah, H. Desa, M. Azri and A. Aziz, in *The 2nd International Malaysia-Ireland Joint Symposium on Engineering*, 2012, vol. 2012, p. 579.

247 S. K. Dixit and N. S. Shingi, *Int. J. Sci. Res. Publ.*, 2012, **2**, 2–4.

248 N. H. Adnan, K. Wan, a. B. Shahriman, M. H. Ali, M. Nasir Ayob and A. a. Aziz, *Int. J. Mech. Mechatronics Eng.*, 2012, **12**, 41–51.

249 N. Tongrod, T. Kerdcharoen, N. Watthanawisuth and A. Tuantranont, in *International Symposium on Wearable Computers (ISWC)*, Ieee, 2010, p. 1.

250 A. Raut, V. Singh, V. Rajput and R. Mahale, *Int. J. Eng. Sci.*, 2012, **1**, 19–25.

251 D. V. K. B. Prakash B Gaikwad, *Int. J. Adv. Res. Comput. Sci. Softw. Eng.*, 2012, **4**, 1–4.

252 G. Saggio, *Sensors Actuators, A Phys.*, 2014, **205**, 119–125.

253 S. Bakhshi and M. H. Mahoor, in *Proceedings - International Conference on Body Sensor Networks, BSN*, 2011, p. 35.

254 G. Saggio, L. Bianchi, S. Castelli, M. Santucci, M. Fraziano and A. Desideri, *Sensors*, 2014, **14**, 11672–11681.

255 P. et. al. Walters, in *IS&T Digital Fabrication*, 2011, pp. 185–188.

256 G. Saggio, *Sensors Actuators, A Phys.*, 2012, **185**, 53–58.

257 A. C. Yuen, A. A. Bakir, N. Nur, Z. Mohd, C. L. Lam, S. Saleh and D. H. B. Wicaksono, 2014, **14**, 2872–2880.